Fermilab Library
0 1160 0003730 3

E 272

FERMILAB

AUG 7 1984

LIBRARY

A Measurement of the Mass, Full Width, and Radiative Width of the B^+ (1237) Meson

BRUCE DAVID COLLICK

April 1984

Thesis

Supported in part by:
The Department of Energy

ROUTE TO

NAME	LOCATION

RETURN TO FERMI LIBRARY

School of Physics and Astronomy
Tate Laboratory of Physics
116 Church Street S.E.
Minneapolis, Minnesota 55455

LIBOFFCE
FERMILAB
THESIS

SITY OF MINNESOTA

A MEASUREMENT OF THE MASS, FULL WIDTH, AND RADIATIVE WIDTH OF THE $B^+(1237)$ MESON

A THESIS

SUBMITTED TO THE FACULTY OF THE

GRADUATE SCHOOL OF THE

UNIVERSITY OF MINNESOTA

BY

BRUCE DAVID COLLICK

IN PARTIAL FULFILLMENT OF THE REQUIREMENTS

FOR THE DEGREE OF

DOCTOR OF PHILOSOPHY

APRIL 1984

LIBRARY

TABLE OF CONTENTS

		Page
ACKNOWLEDGEMENTS		v
ABSTRACT		vi
CHAPTER		
I.	INTRODUCTION	1
	A. Coherent Nuclear processes	5
	B. Coulomb Production	10
	C. Hadronic Production	12
II.	EXPERMINTAL APPARATUS	15
	A. General Considerations	15
	B. Beam	17
	C. Targets	21
	D. Charged Particle Detection	21
	E. Liquid Argon Calorimeter	26
	F. Trigger	30
	G. On Line Data Acquisition	41
III.	CALIBRATION AND ALIGNMENT PROCEDURE	45
	A. Drift Chamber System Calibration	45
	B. Liquid Argon Calorimeter Calibration	48

		Page
IV.	DATA ANALYSIS	61
	A. Overview	61
	B. Charged Track Reconstruction	62
	C. Photon Reconstruction	66
V.	MONTE CARLO	69
	A. General Structure	70
	B. Beam Particle	71
	C. Event Generation	72
	D. Geometry	73
	E. Track Counters	73
	F. MBV Simulation	76
	G. Chambers	77
	H. Liquid Argon Calorimeter	80
	I. Monte Carlo and Data Comparison	81
VI.	NORMALIZATION	98
	A. Beam Related Corrections	99
	B. Target Dependent Corrections	103
	C. Spectrometer Corrections	105
	D. Kaon Decays	108

		Page
VII.	B DATA	113
	A. Mass Fits	126
	B. Cross Section	135
	C. Fits to t Distributions	139
	D. Conclusions	148
	Appendix A	151
	Appendix B	157

Acknowledgments

This experiment was completed with the help of many people from several institutions. The principal collaporators from Fermi National Accelerator Laboratory were Joe Biel, Tom Droege, Alan Jonckheere, Peter Koehler, and Charles Nelson. Also contributing to this effort, from the University of Rochester, were David Berg, Clark Chandlee, Selcuk Cihangir, Tom Ferbel, Joey Huston, Terrence Jensen, Fred Lobkowicz, Takayoshi Ohshima, Paul Slattery and Pat Thompson. From the University of Minnesota the collaborators were Steven Heppelmann, Terry Joyce, Yousef Makdisi, Marvin Marshak, Earl Peterson, and Keith Ruddick. I wish to thank all of these individuals for help and encouragement throughout the writing of this thesis.

Abstract

An experiment was performed at Fermi National Accelorater Laboratory to investigate the coherent production of mesons on nuclear targets (lead and copper). The experiment used and 200 GeV/c incident meson beam and a high resolution forward spectrometer consisting of proportional and drift chambers plus a liquid argon photon calorimeter. This thesis reports the results of the process $\pi^+ + A \rightarrow \pi^+ \omega + A$. The $\pi^+\omega$ spectrum was found to be dominated by the $B^+(1237)$ meson. A fit was performed on the line shape of the $\pi^+\omega$ mass spectrum and values of 1.271 ± 0.011 GeV and 0.232 ± 0.029 GeV were found for the mass and total width. The helicity zero decay probability of the ω, $|F_0|^2$, was measured to be $|F_0|^2 = 0.15 \pm 0.035$. The t distributions were analyzed allowing the electromagnetic and hadronic production processes to interfer. From these distributions a radiative width of 230 ± 61 was extracted.

I. Introduction

Electromagnetic interactions have been used to study the structure of atomic and subatomic systems. In particular, radiative transitions have a long history of application in atomic and nuclear physics. It was natural that the early stages of the quark model involved attempts to predict radiative decays of hadrons. The first radiative decays predicted were $V \to P\gamma$ (vector meson $\to$ pseudoscalar meson and photon) [1]. These first attempts were refined as experimental data became available. The decays were predicted from the point of view of unitary symmetry, simple quark models, and vector meson dominance. Using these ideas it is possible to relate many decays involving radiative transitions among vector and pseudoscalar mesons, and at the present time the agreement between prediction and experimental measurement is good [2].

[1] C. Becchi and G. Morpurgo, Phys. Rev. 140, B687, (1965); L. D. Soloviev, Phys. Lett. 16, 345, (1965).

More recently attempts have been made to predict the radiative decay widths and relationships between the radiative and full decay widths for the $q\bar{q}$, L=1 mesons [3]. These predictions rely on the single-quark description of pion or photon emission and the vector meson dominance hypothesis [4]. The partial widths for single-pion and single-photon emission can be given by [3]

$$\Gamma(a^* \to a\pi) = \frac{p_\pi^3}{8\pi} \frac{1}{2J_{a^*}+1} \sum_\lambda |A_\lambda(\pi)|^2 \tag{1}$$

and

$$\Gamma(a^* \to \gamma a) = \frac{p_\pi^3}{8\pi} \frac{1}{2J_{a^*}+1} \sum_{\substack{\lambda \\ (\lambda=\pm 1)}} |A_\lambda(\gamma)|^2 \quad . \tag{2}$$

Here, p_π and p_γ are momentum factors specific to the particular process. J is the spin of the resonance a*. $A_\lambda(\pi)$ and $A_\lambda(\gamma)$ are the helicity amplitudes for the decay process (defined in reference 3). These two equations can be coupled by vector meson dominance.

Vector meson dominance relates the amplitude $a^* \to \gamma a$ to the decays of the resonance a* to vector mesons, $a^* \to Va$. This relation is given by

[2] P. J. O'Donnell, Rev. Mod. Phys. 53, 673, (1981); T. Ohshima, Phys. Rev. D22, 707 (1980).

[3] J. Babcock and J. L. Rosner, Phys. Rev. D14, 1286, (1976); J. L. Rosner, Phys. Rev. D23, 1127 (1981).

[4] H. J. Melosh, Phys. Rev. D9, 1095, (1974).

$$A_\lambda(a^* \to \gamma a) = \frac{e}{g_\rho} A_\lambda(a^* \to \rho a) + \frac{e}{g_\omega} A_\lambda(a^* \to \omega a) + \frac{e}{g_\phi} A_\lambda(a^* \to \phi a). \qquad (3)$$

In this equation each g represents the coupling constant for a particular vector meson. Simple models involving SU(3) relate g_ρ, g_ω, and g_ϕ in the ratios [5]

$$g_\rho : g_\omega : g_\phi = 9 : 1 : 2. \qquad (4)$$

This relation is used to simplify equation (3) to

$$A_\lambda(a^* \to \gamma a) = \frac{e}{g_\rho}[A_\lambda(a^* \to \rho a) + \frac{1}{3} A_\lambda(a^* \to \omega a) + \frac{\sqrt{2}}{3} A_\lambda(a^* \to \phi a)]. \qquad (5)$$

This thesis reports experimental values for the mass, full width, and radiative width of the B^+ meson. The measurement was carried out through a study of the coherent reaction

$$\begin{array}{l} \pi^+ + A \to A + B^+ \\ \qquad\qquad\quad \hookrightarrow \pi^+\omega \\ \qquad\qquad\qquad\quad \hookrightarrow \pi^+\pi^-\pi^0 \end{array} \quad . \qquad (6)$$

Here N represents targets of different atomic mass and number. The B^+

[5] For a discussion of SU(3) and the vector meson dominance hypothesis see "Photon-Hadron Interactions" by R.P. Feynman, W.A. Benjamin Inc., p. 89.

meson has a spin and parity of 1^+ and quarks in a $^1P_0$ state. The radiative decay involves one quark spin flip ($^1P_0 \rightarrow {}^1S_0 + \gamma$). Using the equations for single-pion and single-photon emission and the vector meson dominance hypothesis the relation between $B^+ \rightarrow \gamma\pi^+$ and $B^+ \rightarrow \omega_\perp \pi^+$ can be written as

$$\Gamma(B^+ \rightarrow \gamma\pi^+) = \frac{1}{9} \left(\frac{p_\gamma}{p_\pi}\right)^3 \frac{\alpha}{(g_\rho^2/4\pi)} \Gamma(B^+ \rightarrow \omega_\perp \pi^+) \ . \qquad (7)$$

ω denotes the transversely polarized component of the vector meson in the decay. As mentioned above, p_π and p_γ are kinematic factors which are determined by the particular decay. $g_\rho/4\pi$ is taken to be 2.7 [3]. $B^+ \rightarrow \omega_\perp \pi^+$ is determined from the ratio $\Gamma(B^+ \rightarrow \omega_\perp \pi^+)/\Gamma(B^+ \rightarrow \omega\pi^+) = 0.89$ [6]. Using and width of 137 MeV and a mass of 1232 MeV equation (7) predicts a radiative decay width of $\Gamma(B^+ \rightarrow \gamma\pi^+) = 195$ keV [6].

Radiative transitions can be measured by three different approaches. Direct measurements can be made, $a^* \rightarrow \gamma a$, but rarely is the branching ratio sufficiently large to allow for this. In addition serious background problems would occur if the decay $a^* \rightarrow \pi^0 a$ occurred. Only the widths of the ω and ϕ have been measured in this manner.

Photoproduction (figure 1a) produces the resonance directly by exchanging a, as a virtual particle, with the target. However, various hadronic exchanges can contribute to this production process. Calculations to extract the radiative width tend to depend on

[6] Particle Data Group, Physics Letters, Vol. 111B, April 1982.

ambiguous models of hadronic production.

Figure 1b reverses the roles of the beam and the target. An incident pseudoscalar meson interacts with the Coulomb field of the target nucleus (Primakoff process) to create the desired particle. Primakoff suggested that the π^0 lifetime could be measured in this fashion [7]. Coherent production can also proceed through hadronic exchange so a clean extraction of the radiative width involves separating the Coulomb and hadronic contributions. The rest of this chapter derives the characteristics and relative rates for these two processes.

A. Coherent Nuclear Processes

The kinematics of a coherent nuclear process are illustrated in figure 2. In this figure a represents the incident particle, a* the produced resonance and N a nuclear target of atomic number A and charge Z. The interaction process is called coherent if the nucleus remains in its ground state or a well defined, low-lying excited state. Typical momentum transfers for coherent interactions can be estimated by using the uncertainty principle. The radius for a nucleus is $R \approx 1.12 * A^{1/3}$ fm and the expected momentum transfer is

[7] H. Primakoff, Phys. Rev. 81, 899 (1951).

a) Photoproduction

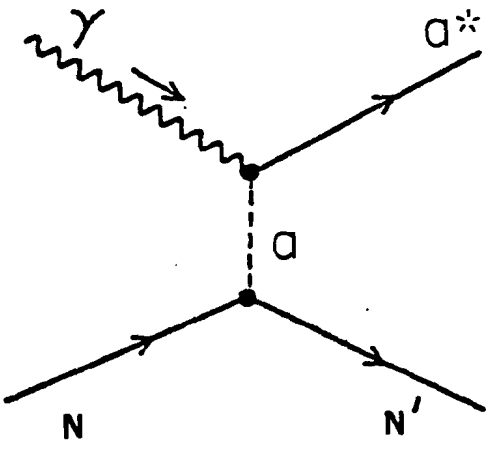

b) Primakoff effect

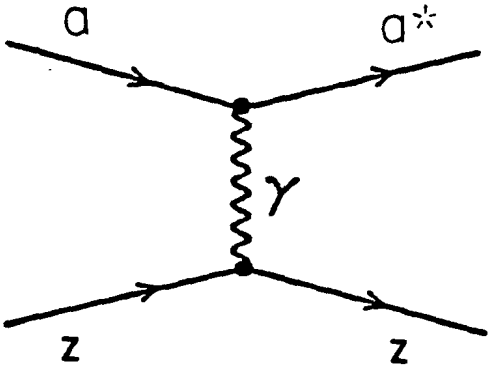

Figure 1

$$P_a = (\vec{P}_a, E_a) \qquad P_N = (\vec{0}, M_N)$$

$$P_{a^*} = (\vec{P}_{a^*}, E_{a^*}) \qquad P_N' = (\vec{q}, E_N)$$

$$q = (\vec{q}, E_N - M_N)$$

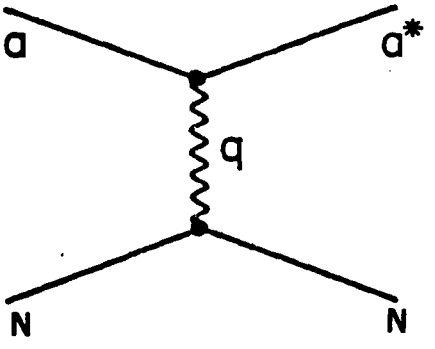

Figure 2

$q \leq hc/R$. This is ~35 MeV/c for a lead target. Consequently the recoil energy of the nucleus is negligible and $E_a = E_{a*}$ in figure 2. This leads to

$$p_a - p_{a*} = [m_a^2 - m_{a*}^2] \;/\; 2p_a = q_{min} \tag{8}$$

where p_a and p_{a*} are the magnitudes for the three-momenta of the states a and a*. This is the minimum momentum transfer required to produce the state a*. Because of the p_a in the denominator, a small q_{min} can be reached for a sufficiently large p_a.

The low momentum transfer imposed by nuclear coherence insures that the scattering angle will always be small. The three-momentum transfer can be written as $\vec{q}_{tot} = \vec{q}_l + \vec{q}_t$. Here, $\vec{q}_l$ corresponds to the longitudinal momentum transfer while $\vec{q}_t$ corresponds to the transverse momentum transfer. In this form q_{min} corresponds to setting $q_t = 0.0$. The longitudinal momentum transfer is essentially a constant for a given reaction. Under these circumstances the usual four-momentum transfer can be written as the difference between the three-momenta $\vec{p}_a$ and $\vec{p}_{a*}$,

$$t = (\vec{p}_a - \vec{p}_{a*})^2, \tag{9}$$

and

$$t_{min} = (m_a^2 - m_{a*}^2) \;/\; 2p_a. \tag{10}$$

For coherent reactions it is possible to use the properties of different nuclei to enhance or suppress various reaction mechanisms [8]. For an incident pseudoscalar meson ($J^P = 0^-$) where only momentum is transferred between the projectile and the target, certain

[8] L. Stodolsky, Phys. Rev. 144, 1145 (1966).

selection rules can be derived. For production in the forward direction, only changes in parity between a and a* of the form $(-1)^l$ are allowed. The spin-parity states that can be produced are $J^P=0^-,1^+,2^-,\ldots$. This process is called diffractive dissociation and can be viewed as taking place via vacuum or pomeron exchange. Away from the forward direction, parity changes of the form $(-1)^{l+1}$ are allowed producing spin-parity states of the form $J=1^-,2^+,3^-\ldots$. The amplitude for these states is proportional to t.

Isospin and G-parity must be conserved at the a - a* vertex, again limiting the avaliable number of coherent final states. For Coulomb production, an electromagnetic interaction, G-parity is not conserved, and the photon has both I=0 and I=1 components. For diffractive production the exchange numbers are $I^G=0^+$. For hadronic exchange processes both isospin exchanges are possible. It should be noted that the nuclear cross section increases like $A^{2/3}$ for isoscalar exchange and $(A-2Z)^{2/3}$ for isovector exchange. It is thus expected that ω ($J^P=1^-$, $I^G=0^-$) exchange will dominate A2 ($J^P=2^+$, $I^G=1^-$) exchange in hadronic production of the B^+.

The quantum numbers for the $B^+(1235)$ are $J^P=1^+$, $I^G=1^+$ [6]. For an incident pion the B^+ meson can be produced by both Coulomb and strong processes. Diffractive production is not allowed because G-parity is not conserved at the π^+-B^+ vertex. Strong production processes with both I=0 and I=1 are allowed but, as mentioned above, the I=1 are suppressed.

The decay characteristics of the B^+ meson can be used to determine its spin and parity. The B^+ meson proceeds to its final state of four pions through two successive decays $B^+ \to \omega\pi^+$, $\omega \to \pi^+\pi^-\pi^0$. An analysis of the angular distribution resulting from the interconnection of these decays can determine the spin and parity of the B^+ (see Appendix A).

For this experiment, the two main contributors to B^+ production were Coulomb production and ω-exchange. The next two sections discuss the amplitude for these two production processes in detail.

B. Coulomb Production

The cross section for the Coulomb production of a state a* with mass m can be written (in the high energy limit) as [9]

$$\frac{d\sigma}{dt\, dm^2} = \frac{Z^2\alpha}{\pi} \frac{\sigma_\gamma(m)^2}{(m^2-m_a^2)} \frac{t-t_{min}}{t^2} \left|F_{em}(t)\right|^2 \quad . \tag{11}$$

Z is the nuclear charge, α is the fine structure constant, m_a is the mass of the incident particle, and $F_{em}(t)$ is the electromagnetic form factor. $\sigma_\gamma(m^2)$ is the total cross section for the reaction $a+\gamma \to a^*$.

[9] A. Halprin, C. M. Anderson, and H. Primakoff, Phys. Rev. 152, 1295 (1966); M. Gourdin, Nuclear Physics 32B, 415 (1971); G. Berland et al., Ann. of Phys. , 75, 461 (1973).

$\sigma_\gamma(m^2)$ can be written as

$$\sigma_\gamma(m)^2 = \frac{2\pi}{p_\gamma^2} \frac{2J_{a^*}+1}{2J_{a^*}+1} \frac{\Gamma(a^* \to a\gamma)\ \Gamma(a^* \to X)}{(m-m_o)^2 + (\Gamma/2)^2} \tag{12}$$

Here m_0 is the mass of the resonance a* and p_γ is the momentum of the photon in the center of mass system. $\Gamma(a^* \to a+\gamma)$ and $(a^* \to X)$ represent partial widths while the Γ in the denominator refers to the total width of a*. In $\Gamma(a^* \to X)$, X is the final state of a* which is measured experimentally. Using this equation and the narrow resonance approximation ($\Gamma \ll m_0$) equation (11) can be reduced to [9]

$$\frac{d}{dt} = 8\pi\ \alpha\ Z^2 \left(\frac{2J_{a^*}+1}{2J_{a^*}+1}\right) \Gamma_o(a^* \to a\gamma) \left(\frac{m_o}{(m_o^2-m_a^2)}\right)^3$$

$$* \ \frac{t-t_{min}}{t^2} \left|F_{em}(t)\right|^2 \quad . \tag{13}$$

Here Γ_0 is the radiative width evaluated at the resonance mass m_0.

In this form certain features of Coulomb production are evident. First the cross section has a narrow peak. The electromagnetic form factor, $F_{em}(t)$, has a weak t dependence for high energies and so the shape of the distribution is dominated by $(t-t_{min})/t^2$. This vanishes at $t=t_{min}$, reaches a maximum at $t=2t_{min}$, and falls roughly as 1/t.

The width at half maximum is given approximately by p_a^{-2}. The narrow peak has a height that increases like p_a^2:

$$\left(\frac{d\sigma}{dt}\right)_{max} = \frac{-1}{2t_{min}} \sim p_a^2 \quad .$$

Consequently, as the incident particle energy increases the experimental resolution must improve in order to detect the Primakoff peak.

Due to the dependence of t_{min} on p_a, the integrated cross section for Coulomb production increases asymtotically as $\log(|p_a|)$. The Z^2 dependence is useful experimentally as a means of checking systematic errors.

D. Hadronic Production

Coherent strong production is expected to be dominated by ω-exchange. The cross section for this process can be parameterized as [10]:

$$\frac{d\sigma}{dt} = A^2 C_s |t-t_{min}| \, |F_h(t)|^2 \quad . \tag{15}$$

[10] H. Harari, Phys. Rev. Lett. 26, 1400 (1971); L. Stodolsky, Phys. Rev. 144, 1145 (1966).

C_s is the amplitude of production on a single nucleon. $F_h(t)$ is the matter-distribution from factor. A is the atomic weight of the target.

The behavior of C_s can be determined from Regge theory. C_s, for ω- exchange, should fall as $1/p_a$. Thus, the integrated cross section falls as $1/p_a$ and at sufficiently high incident particle energies Coulomb production will dominate strong production.

In the forward direction the hadronic form factor behaves like exp(-bt), with $b \sim R^2/4$, R being the nuclear radius. With this form factor the cross section in equation (14) vanishes in the forward direction ($t=t_{min}$), rises to a peak at $t \sim 4/R^2$, and then falls due to the exponential dependence of the form factor. This shape is roughly independent of incident energy while Coulomb production peaks at $t=2t_{min}$, with $t_{min} \sim 1/p_a^2$. This leads to greater separation of the Coulomb and strong contributions at higher energies.

The A dependence is modified by screening of nucleons by absorption. With this effect included the effective A dependence of the integrated cross section can be shown to be $A^{2/3}$ [10]. Since Coulomb production increases as Z^2, the ratio between the Coulomb and strong contributions will increase with heavier nuclei.

The Coulomb and strong amplitudes can interfere. The total cross section must then be written in the form

$$\frac{d\sigma}{dt} = |T_c + e^{i\phi} T_s|^2 \quad . \tag{15}$$

T_c is the amplitude for Coulomb product, T_s is the amplitude for strong production and ϕ is the relative phase between them. Chapter VIII. describes in detail the fitting procedure used to extract the radiative width from this equation.

II. Experimental Apparatus

A. General Considerations

This chapter discusses the experimental apparatus which was used for E-272. The principal purpose of this experiment was measuring the radiative widths of the ρ and K^* mesons. These particles primarily decay into a pseudoscalar meson and a π^0. The subsequent decay of the π^0 into two photons made necessary the detection of both photons and charged particles. The experimental resolution was also important. Unambiguous extraction of the radiative width required adequate separation of the two coherent contributions, Coulomb and strong (see Chapter I.).

To meet these requirements, a spectrometer involving drift chambers was used to measure charged particle trajectories and momenta, while a liquid argon calorimeter was developed for measuring

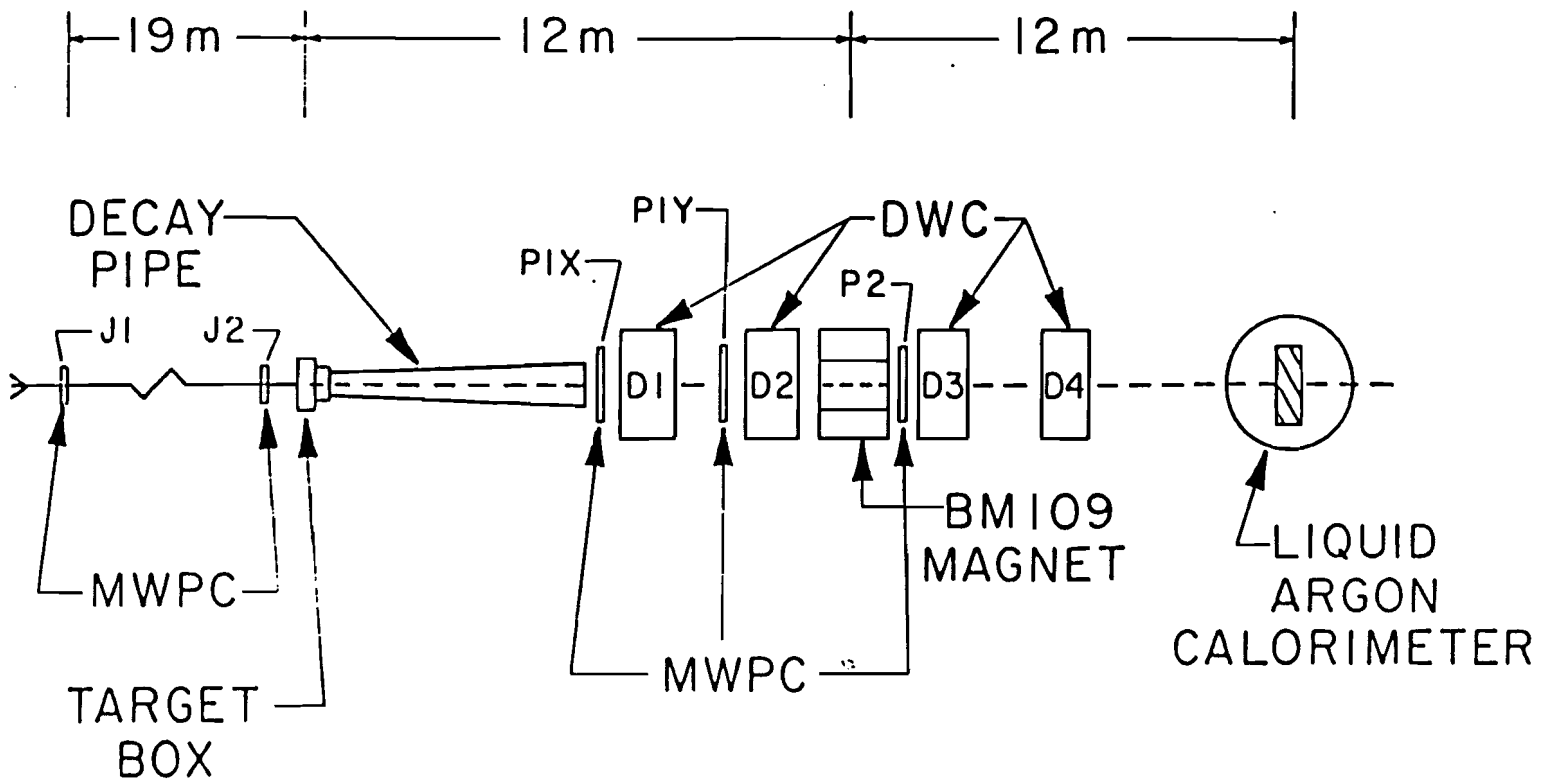
19 m
12 m
12 m
DECAY PIPE
J1
J2
MWPC
TARGET BOX
PIX
PIY
DWC
P2
D1
D2
D3
D4
MWPC
BM109 MAGNET
LIQUID ARGON CALORIMETER

Figure 3

the energies and positions of photons. The small integrated cross sections for Coulomb produced events demanded the development of a "smart trigger" which could pick out the events of interest.

A plan view of the experiment is shown in figure 3. The target box, the decay pipe, and the region between beam proportional chambers were evacuated. This reduced multiple scattering and photon conversion upstream of the magnet, and allowed the charged particles to reach the first spectrometer proportional chamber undeflected. The regions between the drift chamber stations were filled with polyethylene bags containing helium gas to reduce scattering as the particles moved through the spectrometer.

B. Beam

The experiment was performed in the east branch of the M1 beamline at the Fermilab Meson Laboratory. A 400 GeV/c primary proton beam was focused onto a beryllium production target which supplied the six beamlines of the Meson Laboratory. The important features of the M1 beamline, along with computer generated ray traces from selected beam particles are outlined in figure 4. The M1 beamline was a three stage beam [11]. The first stage provided dispersion for momentum selection by the use of a collimator which defined the range of momenta that would be transmitted to the experiment. The second stage

[11] S. Ecklund, Fermilab Report TM-743.2833, May 1977.

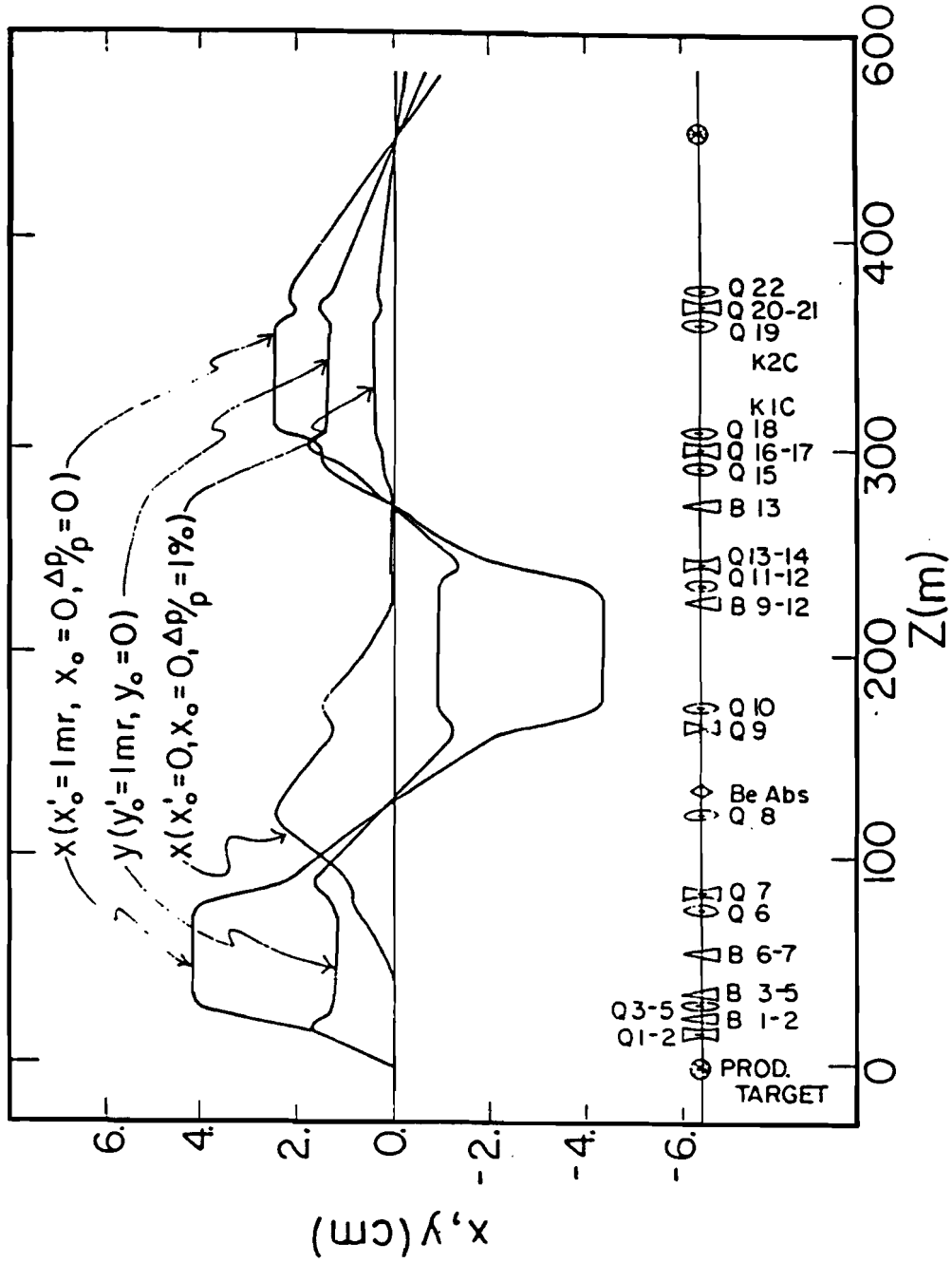
x(x'o=1mr, xo=0, Δp/p=0)
y(y'o=1mr, yo=0)
x(x'o=0, xo=0, Δp/p=1%)
Q 22
Q 20-21
Q 19
K2C
K1C
Q 18
Q 16-17
Q 15
B 13
Q13-14
Q 11-12
B 9-12
Q 10
Q 9
Be Abs
Q 8
Q 7
Q 6
B 6-7
B 3-5
Q3-5
B 1-2
Q1-2
PROD.
TARGET
Z(m)
x,y (cm)

Figure 4

recombined and refocused the different momenta. The third stage provided a 50 m parallel section where three Cerenkov counters were placed to tag each particle in the beam. Direct control of the various beamline elements was available through a beamline computer.

The three Cerenkov counters were called K1, K2, and K3. K1 and K2 were differential Cerenkov counters which identified kaons and pions respectively. Each counter focused light onto a ring of six phototubes. Signals from adjacent phototubes were added together to obtain three outputs which tagged particles by requiring either a 2-fold or a 3-fold coincidence. K3 was a threshold Cerenkov counter with two phototubes, which identified protons. One of the phototubes collected light radiated at an angle less than 5 mrad, while the other phototube collected light at angles greater than 5 mrad. Only the signal from the inner phototube was used by this experiment. All three Cerenkov counters were filled with helium.

The M1 beam transported particles produced at angles from 1.9 mrad to 3.6 mrad relative to the primary beam. The beamline was tuned to provide positively charged 200 GeV/c particles and had a momentum spread of 2%. At this energy and production angle the beam consisted up of 2.5% kaons, 14% pions, and 83.5% protons.

Beam protons were of little interest in E-272. Since trigger rate and dead time considerations limited the maximum acceptable beam flux to $\sim 10^6$ particles per spill, considerably less than the beamline limit, a decision was made to change the content of the beam. A

beryllium "filter" was used to enhance the pion and kaon flux relative to the proton flux by making use of the different kaon, pion, and proton interaction cross sections [12]. The filter was made of four metal blocks which could be inserted into the path of the beam in any combination. These blocks ranged in length from 15 cm to 125 cm for a combined length of 221 cm. They were located approximately 270 m downstream of the production target. Data was typically taken with 178 cm of Be inserted. The beam was attenuated by an order of magnitude as it passed through the beryllium filter, while the content of the beam was changed to 13% kaon, 43% pion, and 44% proton.

Beam particle trajectories were determined by two sets of proportional planes, J1 and J2. Each set had two staggered horizontal and two staggered vertical planes with 1.0 mm wire spacing yielding an angular resolution of 0.015 mrad.

[12] A. Jonckeere et. al., Nucl. Inst. and Meth. 180, 25, 1981.

C. Targets

Two different nuclear targets were used in this experiment. The properties of these targets are listed in Table I. The targets were 3.75 cm by 3.43 cm. They were glued to the end of a thin, lucite holder which was inserted inside of the target-veto assembly (see figure 5).

D. Charged Particle Detection

The E-272 charged particle spectrometer consisted of 24 drift chamber planes and six proportional chamber planes. The separation between drift chamber sense wires was 2.0 cm yielding maximum drift distance of 1.0 cm (drift times of up to 200 nsec). The expected resolution of each plane was 0.025 cm [13].

The drift planes were split into four groups or stations of six planes each in separate gas enclosures. The planes in each station were separated into three pairs. Each doublet was in either a "X", "Y", "U", or "V" orientation. The labels assigned to the planes indicated the coordinate that each plane measured. For instance, an X

[13] T. C. Jensen, PhD Thesis, University of Rochester report UR-747 (1980).

Table 1

Properties of Targets

Target	Atomic Number	Atomic Weight	Thickness (cm)	Thickness (gm/cm)	Number of radiation lengths	Number of collision lengths
Cu	29	63.54	0.638±.003	5.66±.006	0.441±.0005	0.068±.00007
Pb	82	207.19	0.124±.003	1.378±.002	0.216±.0003	0.012±.00002

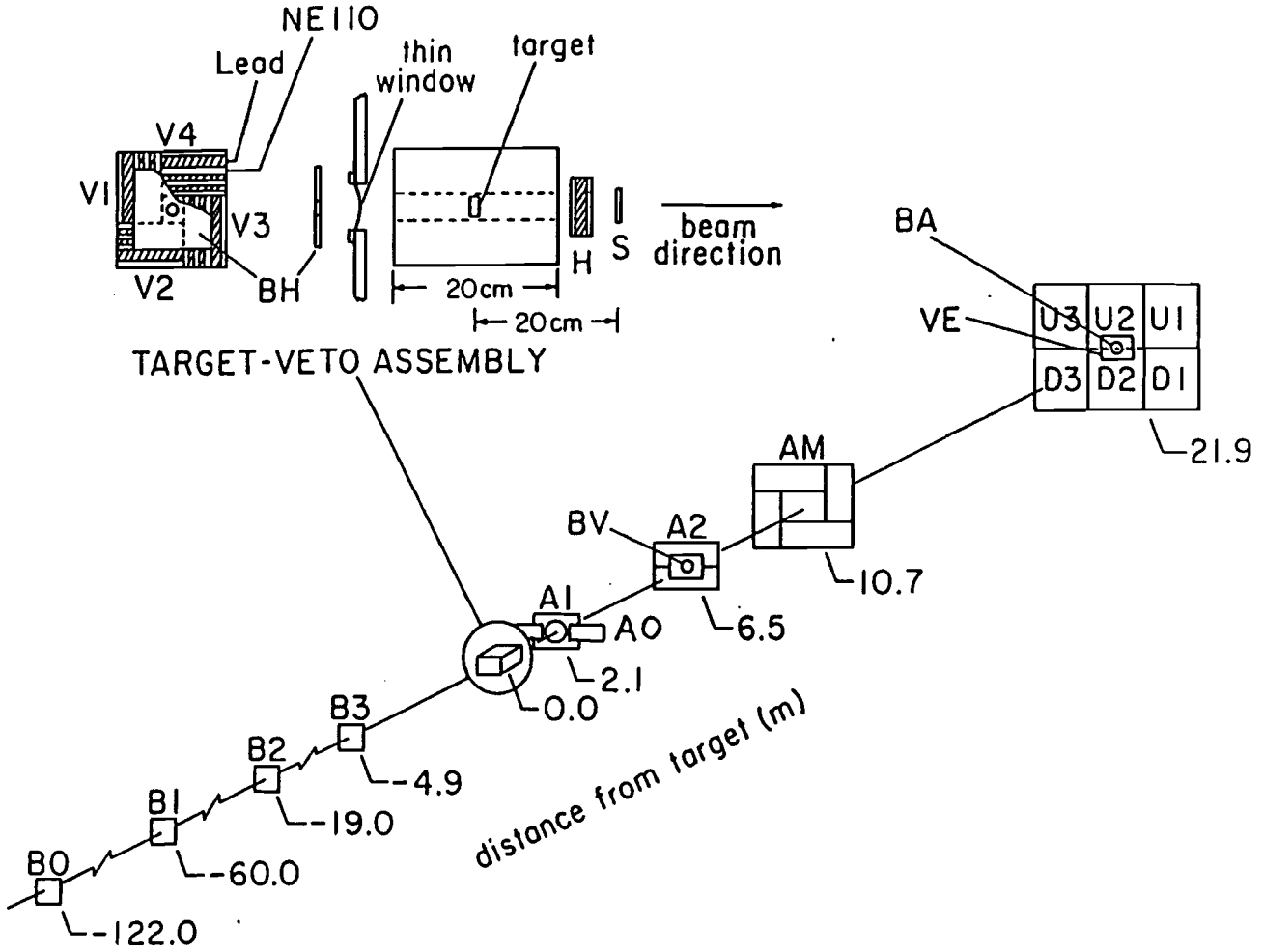
NE110
Lead
thin window
target
V4
V1
V3
V2
BH
H
S
beam direction
20cm
20cm
TARGET-VETO ASSEMBLY
BA
VE
U3
U2
U1
D3
D2
D1
21.9
AM
10.7
BV
A2
6.5
A1
A0
2.1
0.0
B3
-4.9
B2
-19.0
B1
-60.0
B0
-122.0
distance from target (m)

Figure 5

plane had its wire strung perpendicular to the X axis. The coordinate system of the spectrometer was chosen with the positive Z axis pointing along the spectrometer center. The X and Y axes were chosen with the X axis in the horizontal direction and the positive Y axis pointing vertically upward. The X and Y planes gave measurements in the horizontal and vertical while the U and V planes were rotated in opposite directions in relation to the horizontal plane. These definitions applied to all the beam, proportional, and drift chambers.

A drift time does not distinguish on which side of a wire the particle has passed. This results in two possible track positions for each drift wire signal. As a partial solution to this "left-right" ambiguity the two planes of a doublet were offset by half a wire spacing.

The drift chamber stations were called D1, D2, D3, and D4. Stations D1 and D2 were upstream of the bending magnet. Station D1 was located 7.1 m downstream of the target and contained X, Y, and U planes. The U planes were rotated 30^0 in a clockwise direction relative to the positive X axis. Station D2 had X, Y, and V planes located at 9.9 m from the target with the V plane rotated -30^0 in a counter-clockwise direction relative to the positive X axis. The active area of these 12 planes was 20.3 cm by 61.0 cm. This size was chosen so that the U and V planes would cover the aperture of the analyzing magnet.

Downstream of the magnet were stations D3 and D4. These groups had planes in the X, U, and V orientations. Here the U planes were rotated to 18.5^0 and the V planes to -18.5^0 in relation to the horizontal. The stations were placed 13.5 m and 17.3 m from the target and had active areas of 45.7 cm by 111.8 cm and 61.0 cm by 152.4 cm respectively. This size was chosen to cover the active area of the liquid argon calorimeter.

The time signals were digitized by Lecroy Research System (LRS) model 2770A Drift Chamber Digitizers. Each digitizer contained 96 8-bit time-to-digital converters (TDC). Typically each count of a digitizer channel corresponded to 2 nsec, implying a spatial resolution of about 0.1 mm. These TDC's required start, stop, and clear signals. If a second start pulse occurred before a stop pulse had arrived, the clock would be reset. Chapter III. discusses the calibration of these digitizers.

The six proportional planes were separated into three chambers. Each station was composed of two staggered planes with wire spacings of 2.5 mm. P1X was located at 6.9 m, P1Y at 9.7 m and P2 at 13.3 m. These were X, Y, and X planes respectively. The proportional chamber system formed the heart of the trigger system described in Section F. These chambers were also important for off-line track finding because they do not have the left-right ambiguity of the drift chambers (see Chapter IV.).

A BM109 magnet was used to determine the momenta of the particles. The magnet had a aperture of 61 cm by 20 cm and an effective field length of 187 cm. The magnet was operated at a current of 2900 amps which corresponded to an integrated transverse momentum kick of 1.05 GeV/c in the horizontal plane.

E. Liquid Argon Calorimeter

This experiment anticipated photons with an energy range of 5 - 100 GeV/c. These photons primarily came from the decays of π^0's which in turn were part of the decay product of a coherently produced resonance. As noted earlier, t resolution was the key to evaluating the production mechanism. It was calculated that an energy resolution of $20\%/\sqrt{E}$ and a position resolution of 1.5 mm were necessary to achieve the physics goals. To avoid phototube instability and to achieve uniform response over a large active area a liquid argon calorimeter (LAC) was built [14]. The LAC was 25 radiation lengths deep to contain the expected photon showers.

The detector consisted of 61 layers of of 0.2 cm lead sheets alternating with 0.16 cm copper coated G-10 boards. Figure 6 shows

[14] C. Nelson et al., Nucl. Instrum. Methods Vol. 216, 381 (1983).

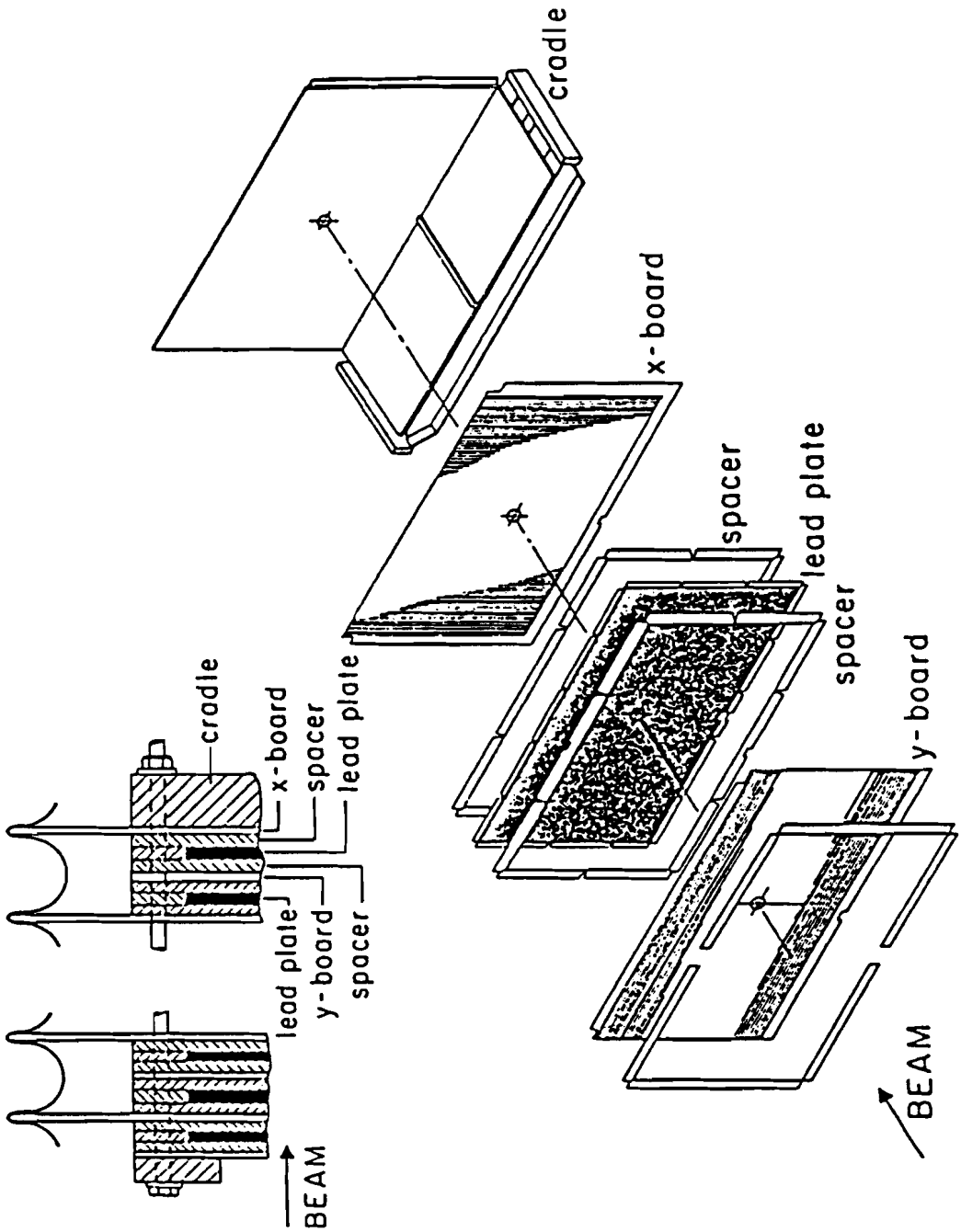
cradle
x-board
spacer
lead plate
spacer
y-board
BEAM
cradle
x-board
spacer
lead plate
lead plate
y-board
spacer
BEAM

Figure 6

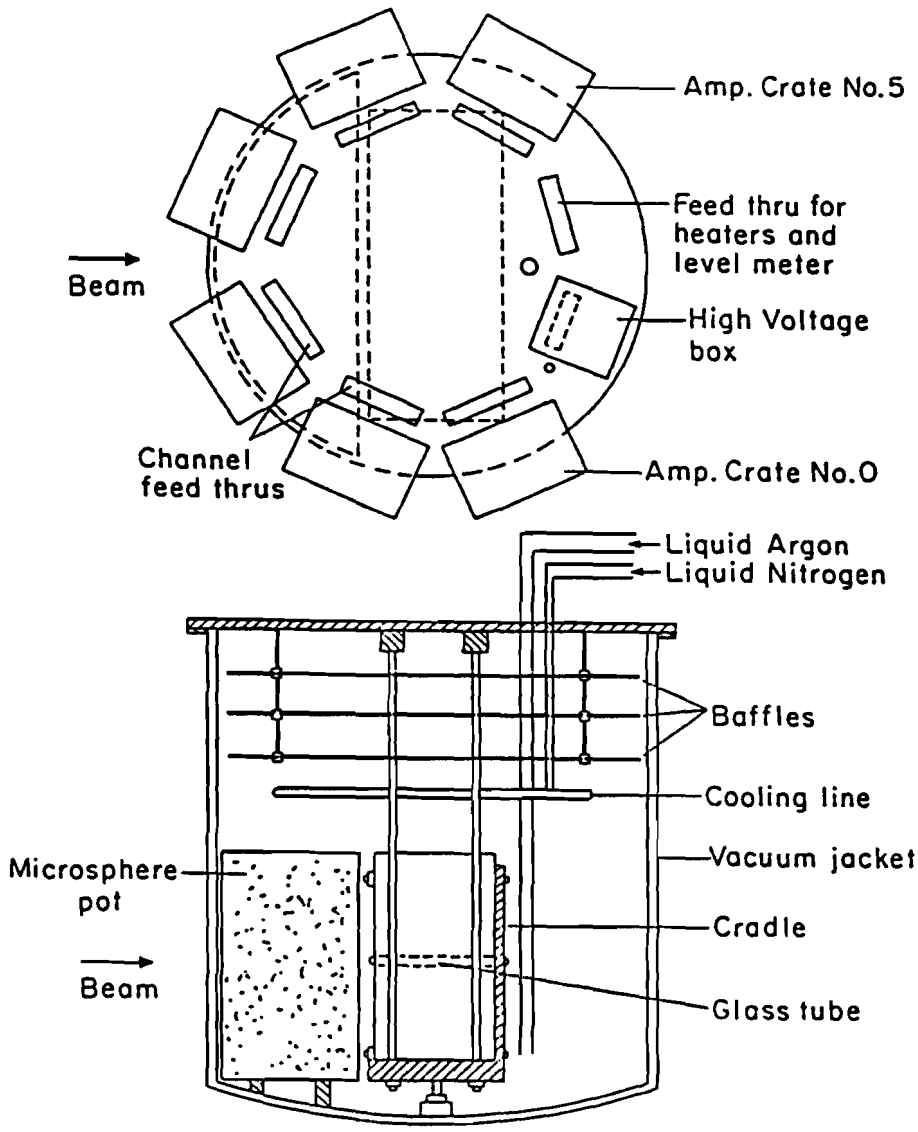
Amp. Crate No.5
Feed thru for heaters and level meter
High Voltage box
Beam
Channel feed thrus
Amp. Crate No.0
Liquid Argon
Liquid Nitrogen
Baffles
Cooling line
Vacuum jacket
Microsphere pot
Cradle
Beam
Glass tube

Figure 7

two cells of the detector. The dimension of each sheet was 140 cm horizontally and 81 cm vertically. This size was chosen to match the magnet aperture. Each sheet and G-10 board had a 1.9 cm diameter hole at its center to allow the beam to pass through a minimal amount of material. In the assembled detector, this region was filled with an evacuated quartz tube. During assembly, alignment and thickness along the detector edge were monitored as each cell was added. This procedure insured the homogeneity of the 0.16 cm argon gap.

Each copper coated G-10 board was segmented into 1.27 cm wide strips which extended the length of the board in the horizontal and vertical directions on alternate boards. The horizontal strips, which were used to measure the Y position, were divided into left and right halves. The strips extending in the vertical direction measured the X position. The detector was divided into front and back halves, each being 12.5 radiation lengths. The detector was thus connected in six sections, X front, X back, Y front right, Y front left, Y back right and Y back left. Within each section all corresponding strips from back to front were connected together for readout. The detector had a total of 480 channels, 224 for X and 256 for Y.

The liquid argon detector was suspended from the steel cover plate of a thin walled steel cryostat and submerged in 3000 liters of liquid argon. A specially shaped stainless steel box was placed in the dewar in front of the detector to displace the liquid argon. This box was filled with hollow glass microspheres to prevent implosion

when the dewar was evacuated. There was a 2.5 cm gap between the box and the front of the detector. A total of 0.9 radiation lengths of material were upstream of the first G-10 board. Figure 7 shows the top and side views of the detector assembly.

Charge sensitive amplifiers were designed for reading out signals from each strip [15]. For each event, these amplifiers sampled the level just before the arrival of a pulse and just after it reached its maximum. The difference between these two levels was then digitized. Fast outputs for triggering were provided by another difference amplifier and these signals could be weighted, summed, and discriminated to form an overall calorimeter trigger decision.

F. Trigger

The E-272 trigger system was designed to accommodate eight logically independent triggering schemes. Four of these were used throughout the running period as data triggers. The remaining four were set up as beam and calibration triggers to be used for monitoring the performance of the experiment.

[15] T. F. Droege, F. Lobkowicz and Y. Fukushima, Fermilab Report TM-746 2500.000, (October 1977).

The definition of a beam particle was common to all data triggers. The scintillation counters used are shown in figure 5. Also shown are the other counters to be discussed later in this section. Beam counters B0 and B1 were placed before and after the Cerenkov counters, K1 and K2 respectively. B2 was located just downstream of K3, and B3 was placed between J2 and the target box. A particle track defined by these four counters also had to pass through a 1.6 cm diameter hole in a veto counter BH, located 38 cm upstream of the target. A beam particle was defined by the coincidence $B0*B1*B2*B3*\overline{BH}$ and was called "B". To complete the definition of a beam particle, this signal was required to coincide with signals from the Cerenkov counters; B*K1 for kaons, $B*K2*\overline{K1}$ for pions, and B*K3 for protons. The $K2*\overline{K1}$ coincidence for pions was necessary to eliminate kaon contamination. With this beam particle definition, less than 0.5% pions were actually kaons, as determined by pressure curves.

Coherent interactions were enhanced by the five veto counters, V1, V2, V3, V4, and H (see figure 5). The V counters surrounded the target and were in position to veto any fragments of the nucleus which scattered at large angles and escaped the target. The H counter had a 3.2 cm hole to allow the beam to pass through; it was located 20 cm downstream of the target. All of these counters were lead scintillator sandwiches of about six radiation lengths. Their outer surfaces were lined with 0.25 mm copper to absorb low energy δ-rays, which could be produced as the charged particles passed through the

target. These δ-rays could otherwise veto good events.

The counters A0, A1, A2, and AM circumscribed the upstream geometrical acceptance of the spectrometer. A0, A1, and A2 consisted of lead scintillator sandwiches of about six radiation lengths and were used to veto neutral hadrons and photons. AM was a fan-in of several counters which covered the magnet's upstream face and the inner pole faces. These counters vetoed those charged particles which hit the magnet face as well as low momentum charged particles which were bent into the inner faces of the magnet.

The last veto counter was a 2.9 cm diameter circle called BA. It was placed in front of the the LAC to shadow the hole where the noninteracting beam passed. All of these signals were combined to form the common logic signal

$$\text{Veto Logic} = B2*B3*\overline{BH}*\overline{BA}*\overline{(V1+V2+V3+V4)}*\overline{(A0+A1+A2+AM)}.$$

This signal defined an interaction in which the produced particles passed through the magnet and the nucleus remained in the target.

A 3.8 cm square threshold counter, called the S counter, was placed 20 cm downstream of the target. The pulse height from this counter gave information on the number of charged particles leaving the target. Different discriminator levels were set to select different S counter pulse heights and were called S0, S1, S2, and S3. S0 was set to select a minimum of one charged particle passing through the S counter. S1 was set as an upper limit on the one charged particle S counter signal. S2 was set slightly lower than S1 and was

used as the lower threshold for two charged particles. S3 was set to select a minimum of three charged particles.

In addition, a crude trigger processor was developed at Fermilab [16] to count the number of charged tracks downstream of the target using the spectrometer's proportional chambers. The signature for a track consisted of signals on a continuous group of adjacent proportional chamber wires separated from another group by at least one blank wire. In the case of the P1X and P1Y chambers, the wire signals from the two offset planes were interleaved to produce one "continuous plane". Each plane of P2 was wired separately. The four processors provided logic levels proportionate to the number of groups or tracks and could count up to a maximum of five groups. These signals were passively latched as well as implemented in a trigger decision.

One of the triggers used in E-272 required only one track out of the beam region. This topology could easily be mimicked by a beam particle which interacted with the material in the spectrometer downstream of the decay tank. To suppress this background, a hard wired circuit called the Matrix Beam Veto (MBV) was developed. Signals from the X planes of J1 and J2 and the 3 cm central region of P1X were put in coincidence to determine whether the hits formed a straight line. The MBV would give a signal for any track which deviated by less than 0.3 mrad from the beam direction as defined by

[16] C. R. Kerns, Fermilab Report TM-819 2510.000, (October 1978).

J1 and J2. This arrangement could also veto good events which scattered in the vertical plane. To prevent this, a 2.5 cm diameter counter, BV, was placed just downstream of P1X, and its signal was put in coincidence with the MBV signal. The combined signal MBV2 = MBV*BV was used as a veto signal.

The final state particles of the ρ and K^* were primarily one charged particle and two photons from a π^0 decay. In addition the decay of a beam kaon to this final state was a major tool in evaluating the performance of the spectrometer (see Chapter V.). The two photons from these reactions deposited energy in the LAC. To aid in a trigger decision, the fast outputs of the LAC amplifiers were ganged together and a minimum threshold was set on this energy signal. This signal was call a LAC pre-trigger. Merely interrogating this signal was insufficient because hadrons would frequently interact and deposit energy in the detector. To help remove this type of background, six scintillator panels, three up and three down, were placed in front of the LAC covering its active area (see figure 5). The LAC trigger logic was instrumented to recognize energy deposited above or below the center line. Using this information, a trigger was set up to crudely check the overlap of a charged particle and LAC energy (see figure 8).

The trigger elements described above could be combined in any fashion to form a data trigger. Due to timing considerations each trigger was formed in stages. The initial stage used the beam and

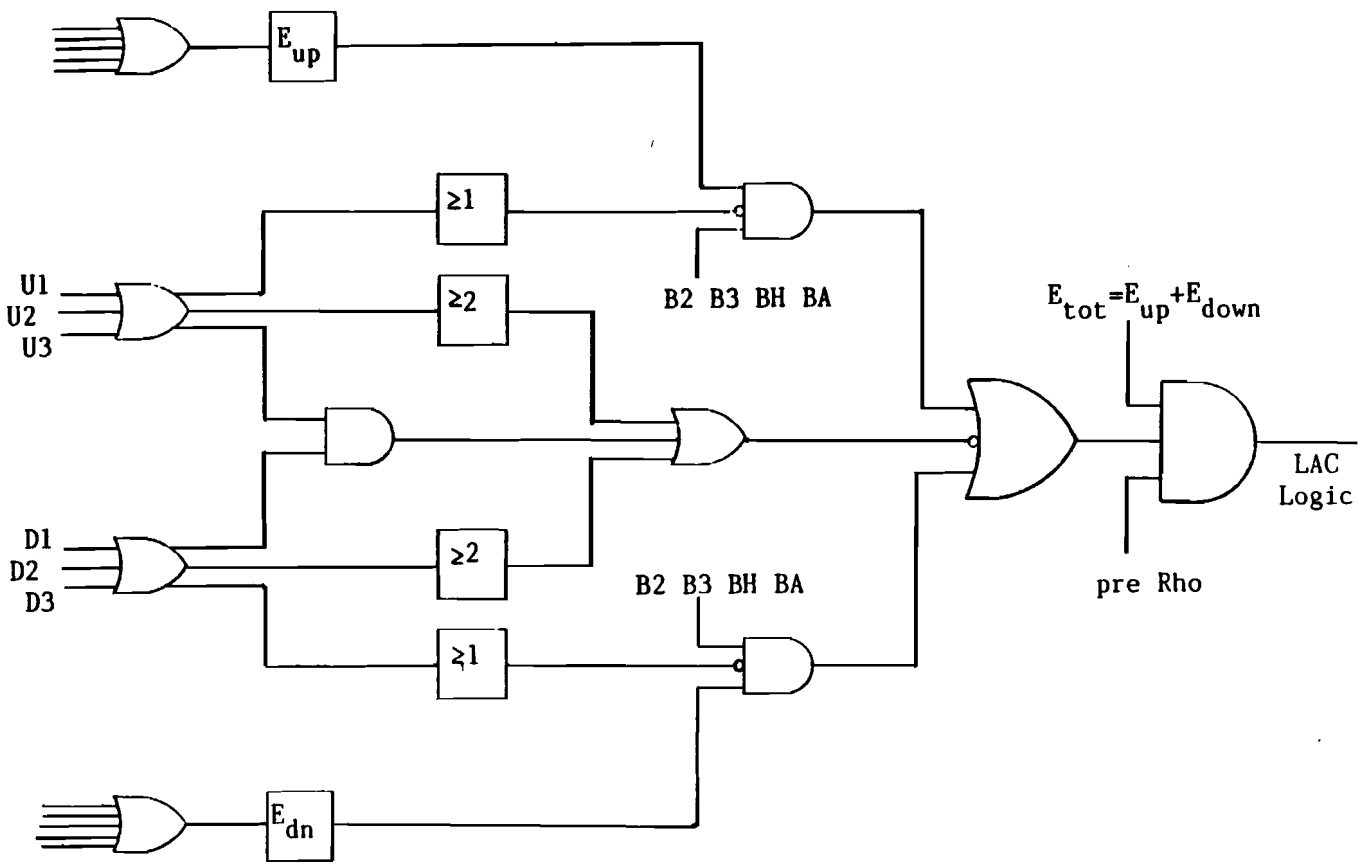
E up
≥1
≥2
U1
U2
U3
B2 B3 BH BA
E tot=E up+E down
LAC
Logic
D1
D2
D3
≥2
B2 B3 BH BA
pre Rho
≥1
E dn

Figure 8

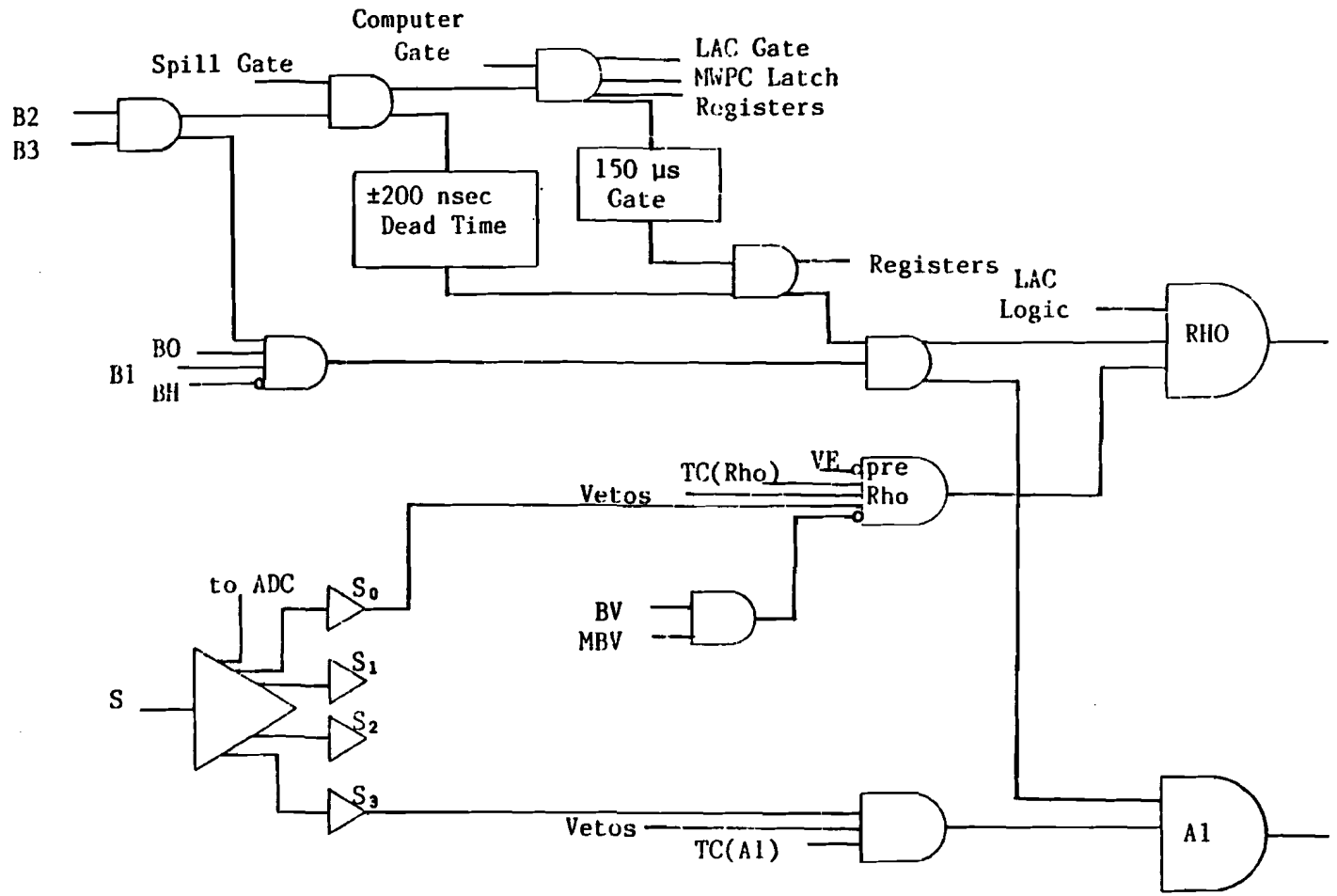
Computer
Gate
Spill Gate
LAC Gate
MWPC Latch
Registers
B2
B3
±200 nsec
Dead Time
150 μs
Gate
Registers
LAC
Logic
RHO
BO
B1
BH
TC(Rho)
VE
pre
Rho
Vetos
to ADC
S0
BV
MBV
S1
S
S2
S3
Vetos
TC(A1)
A1

Figure 9

veto counters. Signals from these counters were used to set the reference timing of the experiment (see Section G.). Next a reaction had to satisfy track counter, MBV, and the LAC pre-trigger requirements. The last stage required a reaction to satisfy the full LAC trigger.

The data triggers were call Rho, A1, V, and Pi-E. This thesis is primarily concerned with data from the Rho and A1 triggers. Figure 9 is a logic diagram of these triggers.

The Rho trigger was designed to select one charged track and electromagnetic shower energy in the LAC. This trigger employed the veto logic, S counter, track counters, and MBV elements. Each of the four track counters was required to count one or two tracks for this trigger, TC(Rho). The track counting logic (see figure 10) was defined loosely to allow for electronic noise and dead chamber wires. The LAC logic described above was also part of this trigger. In addition, a 17.8 cm by 1.9 cm rectangular counter, the VE, was added at the LAC to veto elastic scattering events. The Rho trigger was defined as:

$$\text{Rho} = B*(\text{Veto Logic})*SO*TC(\text{Rho})*MBV2*\overline{VE}*(\text{LAC Logic}).$$

The A1 trigger was set up to pick out three charged track events. It was the simplest of the data triggers and used only the veto logic, track counters and S counter. For this trigger, P1X and P1Y were required to detect two or three tracks while the P2 system was required to report three or four tracks, TC(A1). The track counting

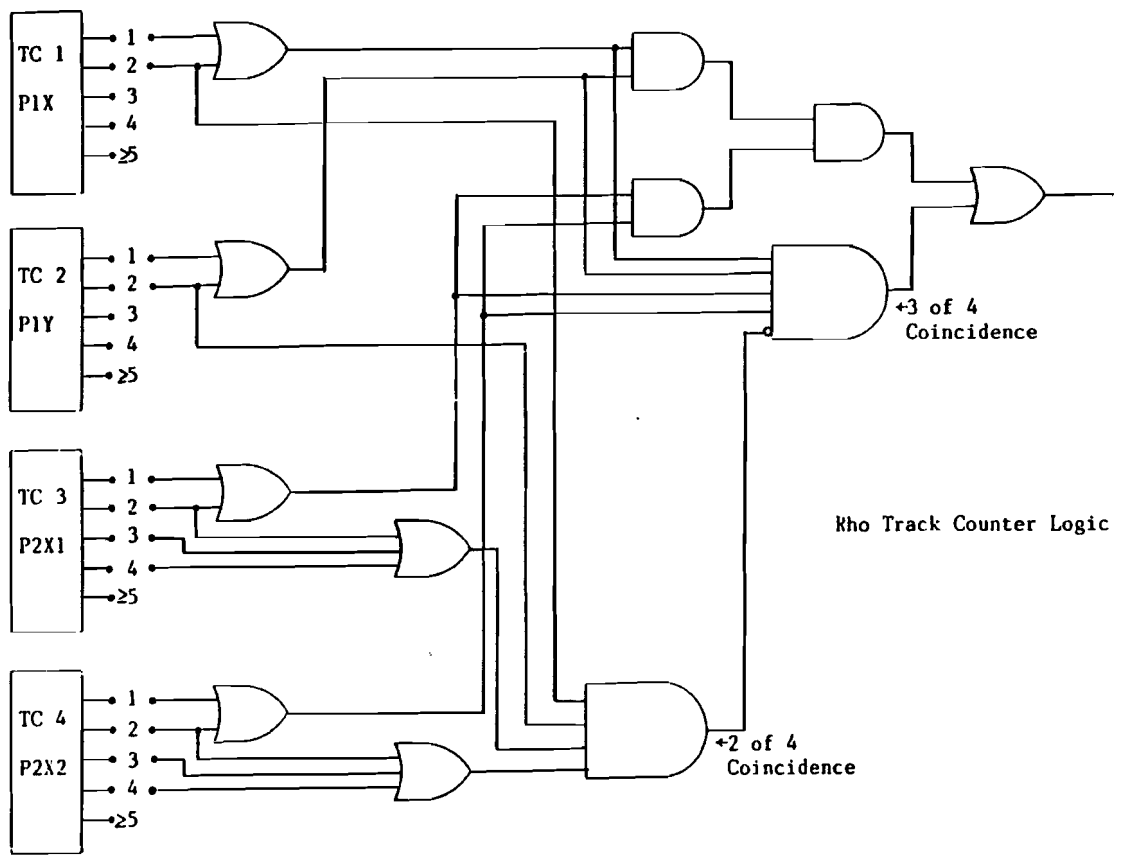

Rho Track Counter Logic

Figure 10

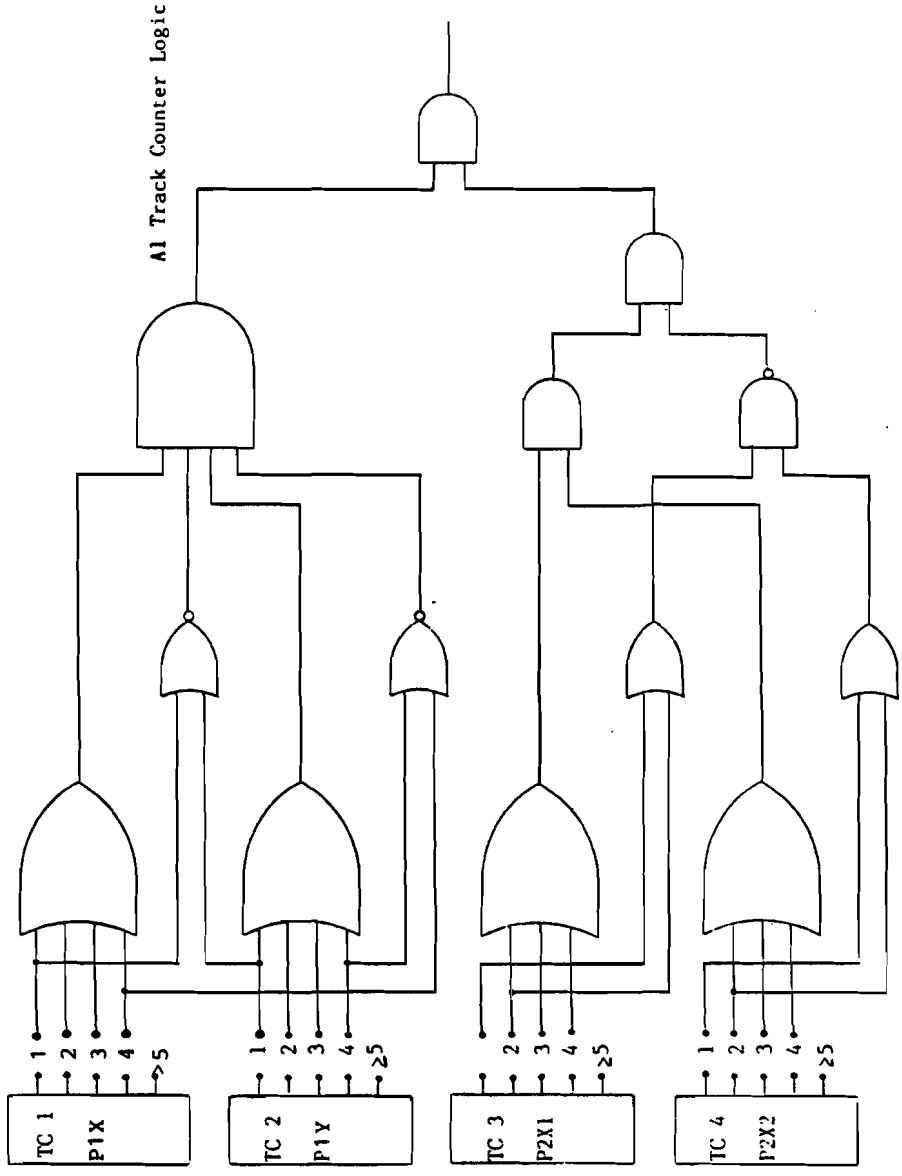
A1 Track Counter Logic
TC 1
P1X
TC 2
P1Y
TC 3
P2X1
TC 4
P2X2
1
2
3
4
≥5

Figure 11

logic is shown in figure 11. The B meson was one of the reaction which satisfied this trigger. The A1 trigger was defined as:

A1 = B*(Veto Logic)*S3*TC(A1)

The V trigger selected reactions in which the intermediate particle products were a charged particle and a neutral which decayed into two charged particles before exiting the decay tank. The trigger was set up using the S counter to select one charged particle leaving the target while the track counters were set for three tracks by using the TC(A1) logic. The MBV was used to veto $K^+ \rightarrow \pi^+\pi^+\pi^-$ events which had not decayed before leaving the decay tank. In summary, the trigger was defined as:

$V = B*(\text{Veto Logic})*(S0*\overline{S1})*TC(A1)*MBV2.$

The Pi-E trigger was set to select pion-electron scattering events. The S counter was set to select a minimum of two charged particles leaving the target, while the track counting logic was loosely set for two tracks. The LAC minimum energy threshold was also implemented. In summary, the Pi-E trigger was defined as:

Pi-E = B*(Veto Logic)*S2*TC(Pi-E)*(LAC Minimum).

A major component of the Rho, A1, and V triggers were kaon decays. These decays were used for studying the resolution and acceptance of the spectrometer as well as the efficiency of the reconstruction program. The $K^+ \rightarrow \pi^+\pi^0$ mode was ideal for comparing with events in the Rho trigger. In addition a number of Ke3 ($K^+ \rightarrow e^+\nu\pi^0$) were taken as a component of the Rho trigger and were used

in the LAC calibration and alignment (see Chapter III). $K^+ \to \pi^+\pi^+\pi^-$ decays were present in both the A1 and V triggers. The V trigger kaons had to decay downstream of the S counter while the A1 kaons had to decay upstream of the S counter.

Three of the monitor triggers were beam triggers. Two of these took a random sample of beam particles which satisfied the beam definition B. One sampled those particles which hit the BA counter while the other sampled those which missed. The third beam trigger was the first beam particle of every spill. The fourth monitor trigger was a "between spill" trigger. This trigger was responsible for initiating and recording the information from the calibration process (see Chapter III).

G. On-line Data Acquisition

The on-line computer was a PDP-15. It communicated with the experiment through a CAMAC read out system and was responsible for writing data onto magnetic tape and for some rudimentary analysis. A block diagram of the read-out system is shown in figure 12.

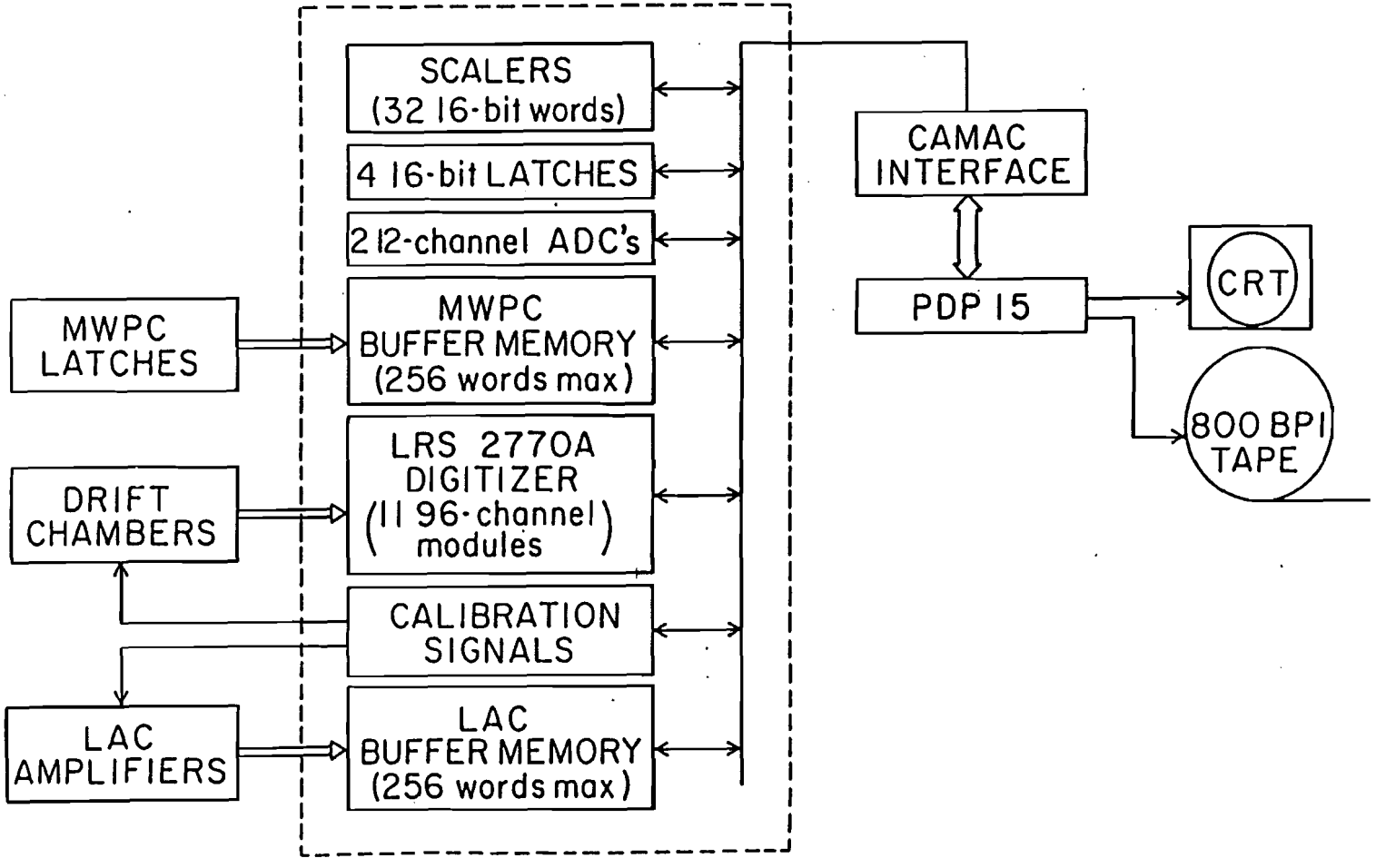
SCALERS
(32 16-bit words)
4 16-bit LATCHES
2 12-channel ADC's
MWPC
BUFFER MEMORY
(256 words max)
LRS 2770A
DIGITIZER
(11 96-channel
modules)
CALIBRATION
SIGNALS
LAC
BUFFER MEMORY
(256 words max)
MWPC
LATCHES
DRIFT
CHAMBERS
LAC
AMPLIFIERS
CAMAC
INTERFACE
PDP 15
CRT
800 BPI
TAPE

Figure 12

Each new beam particle was referenced by a B2*B3 beam signal. The leading edge of the B3 signal established the reference time for all coincidences and the TDC system. When a reaction satisfied the initial stage of a trigger (mentioned above) the experiment was gated off. At this point the proportional chambers and four 8 channel 16 bit registers were latched. The signal for latching was $B2*B3*\overline{BA}$. These registers contained the states of the veto counters, the Cerenkov counters, and the trigger elements. A set of ADC's were read out and contained such things as S counter pulse heights and gamma detector total energy.

No B2*B3 signal was counted if it was preceded or followed by another such signal within 200 ns. This cut was necessary to insure that the information being recorded by the drift chamber TDC system was associated with the correct event. The TDC system required three signals. The start was provided by a pulse from a drift chamber amplifier. The TDC channel which received this signal accumulated counts until a stop was received. The stop was a delayed B3 signal and was sent to all the TDC channels. The PDP-15 read and cleared the TDC system as part of an event read-out.

Two independent sets of scalers were used in the experiment. One set recorded the rates between events, while the other set accumulated the rates for an entire spill. The "event" scalers were written to tape with each trigger while the "spill" scalers were written to tape with the first "between spill" calibration trigger. These scalers

provided a means of cross checking the gated beam count, which was used in calculating cross sections.

The LAC amplifiers were located in six CAMAC crates on top of the cryostat (see figure 6). A scanner was located in each of the six crates. Each scanner was in turn connected to the master controller. When an event satisfied a trigger, the master controller checked the individual amplifiers through the crate scanner and digitized each of the channels that was above a preset threshold of ~600 MeV. These values along with the address of the channel were transmitted to a CAMAC buffer memory which the on-line computer would read and clear.

III. Calibration and Alignment Procedure

A. Drift Chamber System Calibration

The calibration and the alignment of the drift chamber system required determination of parameters describing the electronics, the gas drift velocities, and the sense wire positions. The final goal of this process was to convert the drift time count of a particular channel into coordinates in space.

The between-spill calibration trigger was set up to obtain an absolute time calibration for the LeCroy time digitizers. The trigger consisted of a start and a stop pulse separated by a computer-controlled time delay. The time delay between these pulses was cycled through four different values. The accurately known intervals of these standard delays were compared with the time count of each digitizer. This information established a relationship between elapsed time and the number of counts recorded by a digitizer.

A slope or gain and a time offset were determined for each channel.

Each wire position had to be known in relation to a standard coordinate system. During construction and installation of the chambers standard survey techniques were used to obtain uniform wire spacing and orientation of the wire planes perpendicular to the beam direction. While the Z positions of the drift chambers could be measured directly none of the wires of a plane coincided with an axis of the standard coordinate system. This necessitated the determination of a position offset. With the position offset, the drift velocity for the electrons in the gas, and the gains and time offsets for the TDC's, counts were converted into coordinates.

Initial estimates for the drift velocities and position offsets were determined by using "straight-through" beam particles. These data were obtained at low intensity with the analyzing magnet off and the target out. The position offsets and drift velocities were determined by fitting each particle to a straight track hypothesis as defined by the beam chambers J1 and J2. Position offsets were determined for each drift plane. Only two drift velocities were determined: one for the chambers upstream of the magnet and one for the chambers downstream of the magnet.

These parameters were fine tuned using Rho trigger events which had only one hit in each of the 24 drift planes. Only the drift chamber information was used in the fitting procedure. The analyzing magnet was on, and the upstream and downstream chambers were treated

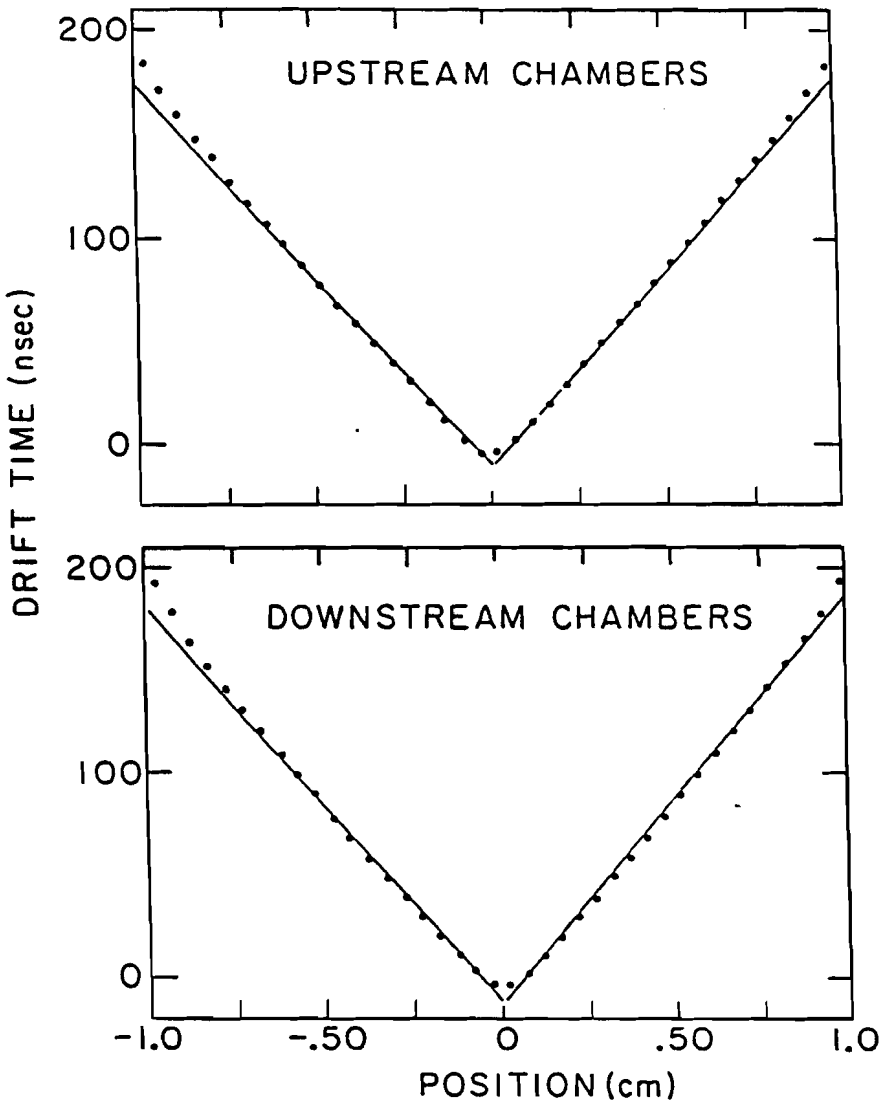
UPSTREAM CHAMBERS
DOWNSTREAM CHAMBERS
DRIFT TIME (nsec)
200
100
0
200
100
0
-1.0
-.50
0
.50
1.0
POSITION (cm)

Figure 13

separately. These events illuminated a larger region than the limited central portion of the chambers which the straight through triggers sampled.

Figure 13 shows the relation between drift time and drift distance for typical chambers. The lines in the figure were drawn using the velocities determined by the alignment process: 5.13×10^{-3} cm/nsec upstream and 4.90×10^{-3} cm/nsec downstream. Using reconstructed $K^+ \rightarrow \pi^+ \pi^0$ decays the resolution for a drift plane was determined to be $\sigma = 0.23$ mm.

B. Liquid Argon Calorimeter Calibration

The LAC calibration was split into two parts: the between spill events which were used to monitor the stability of the electronics and a 50 GeV/c electron run which was used to determine the gain of each amplifier channel. There were two types of between spill triggers monitoring the LAC. One continually monitored an effective zero level or pedestal for each LAC amplifier. The measurements of the pedestals were obtained by setting the read-out threshold to zero. The pedestal measurements from each tape were averaged on a channel by channel basis and were stored in the calibration file. Typically, the pedestal levels varied by less than 10% per run. The pedestal level

had to be subtracted from an amplifier's ADC count before an energy could be assigned.

The second type of between spill trigger monitored the gains of the individual amplifiers. These were studied by applying pulses of known amplitude to the inputs of the amplifiers. The gain of an individual channel fluctuated by less than 2% over the period of the two month run. Consequently, variations in electronic gains were not included in the calibration process.

To convert ADC counts to energy, a special low intensity 50 GeV/c negative beam calibration run was taken. At this momentum about 10% of the beam consisted of electrons. The LAC could be moved in small steps in the X direction, and a vertically-deflecting dipole magnet, located just upstream of the target box, made it possible to scan in the Y direction. The small steps of the scans provided each strip with a range of energies.

At this energy a typical electromagnetic shower covered 3 - 5 strips. The accumulated energy read out by the LAC was compared with the momentum of each electron as determined by the charged-particle spectrometer. The gain of each strip was adjusted to give the best agreement between these measurements.

This procedure worked well in the front half of the detector, but typically only 13% of the calibration electron's energy was deposited in the back portion. It was impractical to determine gains on a

channel by channel basis. A constant gain was assigned to the back portion's amplifiers. This gain was determined along with the calibration of the front amplifier gains. Once these constants were determined it was possible to monitor the performance of the LAC by observing reconstructed π^+-e^-, $K^+ \rightarrow \pi^+\pi^0$, and Ke3 events.

Figures 14 a and b show the energy and position resolution for the 50 GeV/c electron calibration. The narrow Gaussian curves in these two figures illustrate the expected resolutions of the spectrometer. The energy resolution for the 50 GeV/c electron data was $\sigma(E)/E = 10.3\%/\sqrt{E}$ where the energy, E, is given in units of GeV. The spatial resolution was 0.58±0.07 mm when the resolution of the spectrometer had been unfolded.

The response of the LAC to electromagnetic showers of differing energies was studied by using the positron from Ke3 decays. Figure 15 shows a comparison of the reconstructed LAC energy and the momentum measured by the spectrometer. The linearity of the response was better than 5.0% in the momentum range from 20 GeV/c to 80 GeV/c.

Figure 16 shows the energy resolution for Ke3 decays. The plotted points were obtained from a comparison of the LAC and the spectrometer energies. The dashed line through the data is given by $\sigma^2(\mathrm{GeV}) = (0.14*\sqrt{E(\mathrm{GeV})})^2+(0.55)^2$. The result for the electron calibration is shown for comparison. There is a notable difference in resolution. This difference was attributed to several effects. The Ke3 events had two photons from the π^0 decay. These photons sometimes

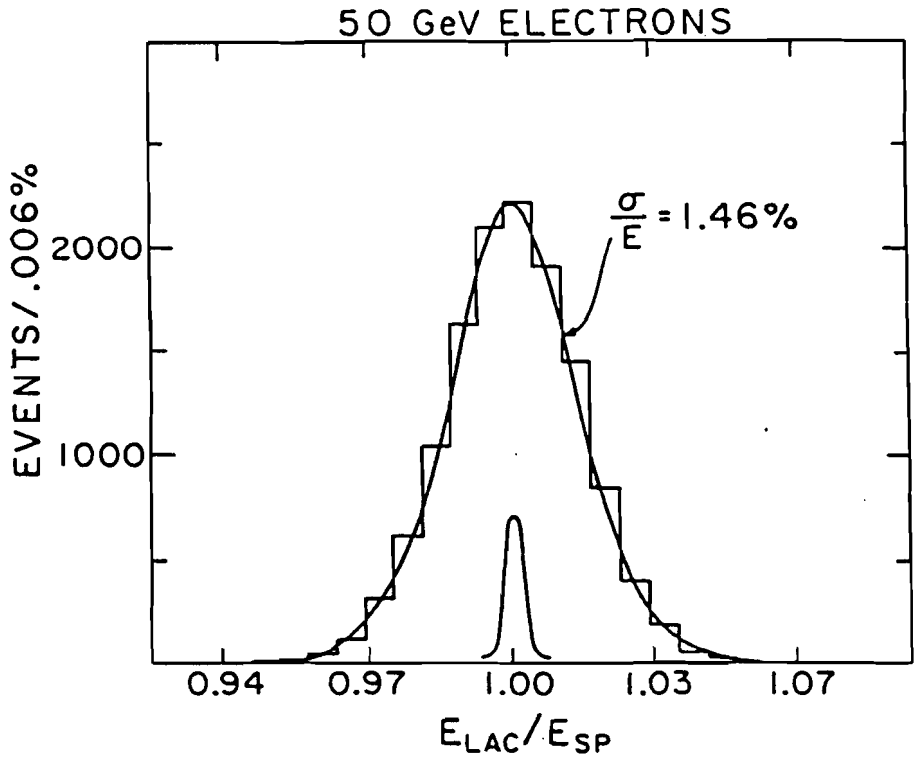

Figure 14 a

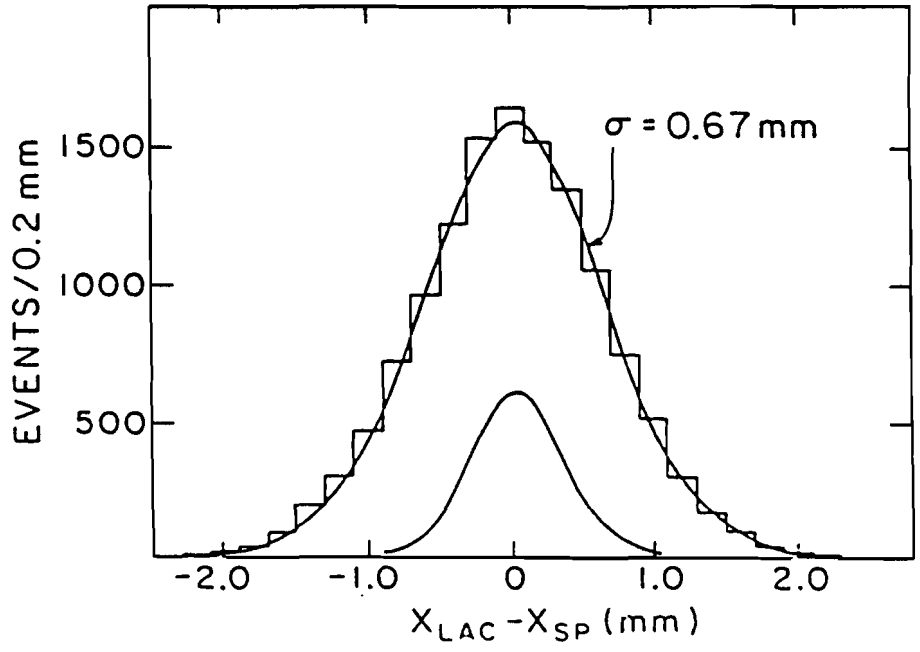

Figure 14 b

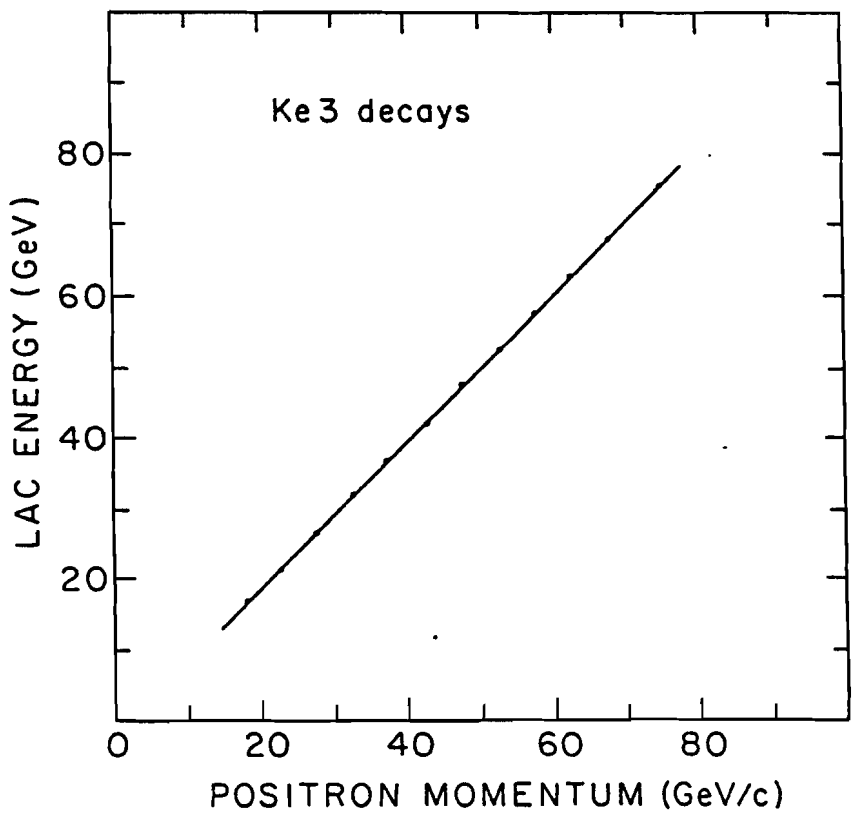
Ke3 decays
LAC ENERGY (GeV)
80
60
40
20
0
20
40
60
80
POSITRON MOMENTUM (GeV/c)

Figure 15

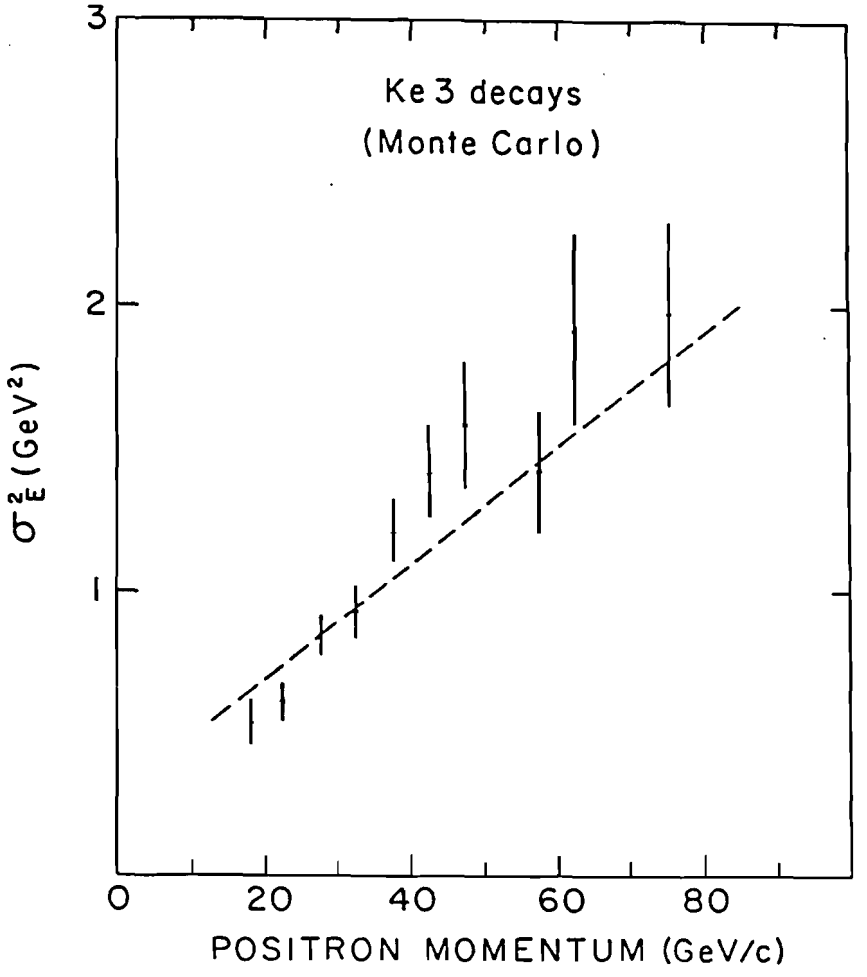
Ke 3 decays
(Monte Carlo)
σ_E^2 (GeV^2)
3
2
1
0
20
40
60
80
POSITRON MOMENTUM (GeV/c)

Figure 16

struck the LAC near the position of the positron and resulted in overlapping showers. Reconstruction of overlapping showers was more difficult and lead to inaccuracies in reconstruction of the positron energy. The Ke3 data were accumulated over several months while the electron calibration data were gathered in a day. The calibration data did not suffer from inaccuracies in monitoring the behavior of the individual amplifiers. Also, high intensities occasionally produced amplifier pedestal shifts which were uncorrelated with the Ke3 events.

Figure 17 shows the electromagnetic shower shape obtained from the electron calibration data. By using Ke3 events it was determined that this shower shape was independent of energy to within 3% - 5%. The shower shape was used by the photon reconstruction program to separate overlapping showers. The hadronic shower shape, determined from interacting π^+-e^-'s and from $K^+ \rightarrow \pi^+\pi^+\pi^-$ decays, is shown for comparison.

Another test of the performance of the gamma detector was observing the position and width of the π^0 mass peak from $K^+ \rightarrow \pi^+\pi^0$ decays. There were approximately 1000 of these decays per tape. A tape contained about 25,000 triggers and took about one hour to accumulate. Observation of the π^0 peak from these events revealed a steady increase in the π^0 mass as a function of time (see figure 18). This same effect was found when the energy of π^+-e^- and Ke3 electromagnetic showers were compared to the electron's momentum as

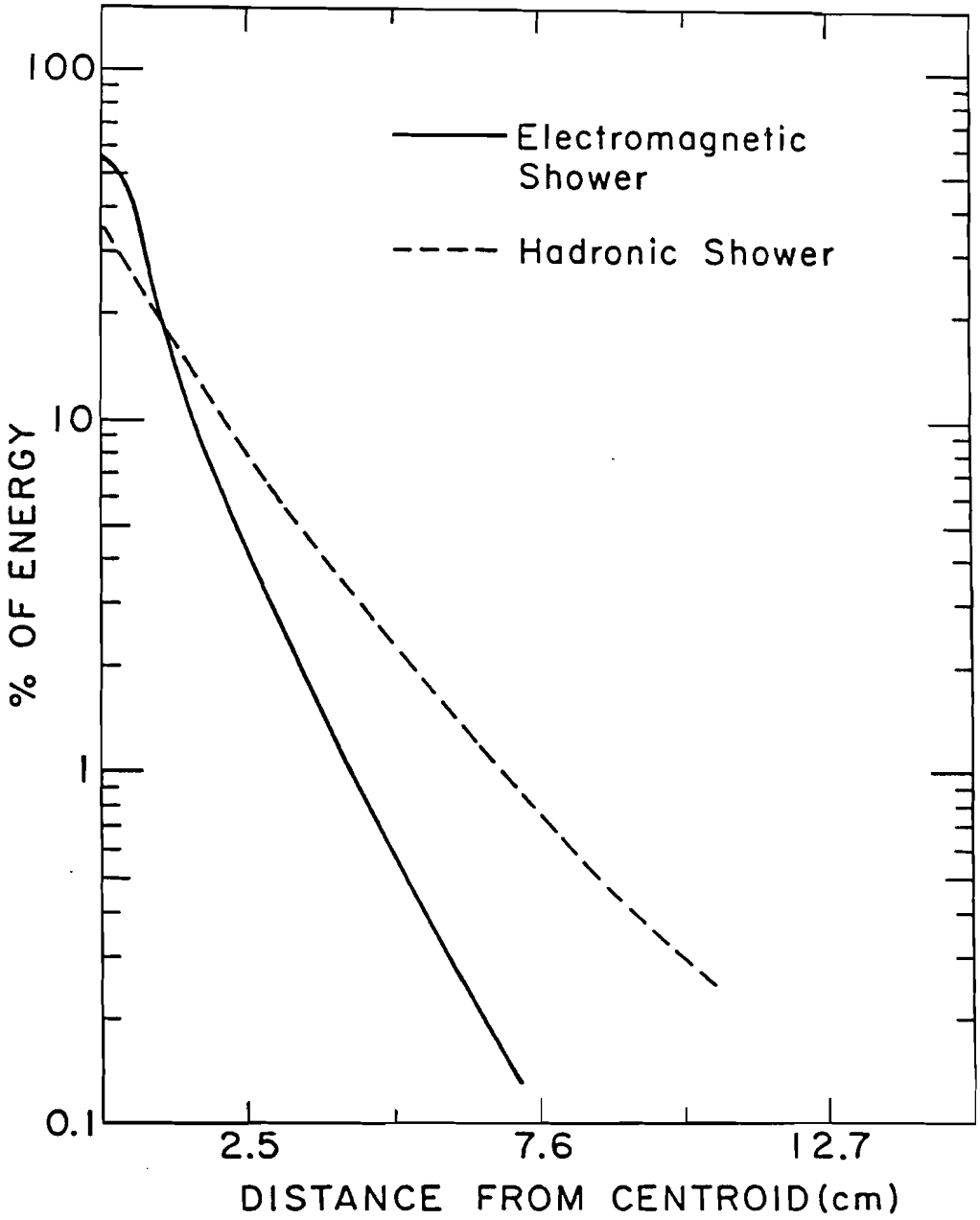
100
10
1
0.1
% OF ENERGY
Electromagnetic Shower
Hadronic Shower
2.5
7.6
12.7
DISTANCE FROM CENTROID (cm)

Figure 17

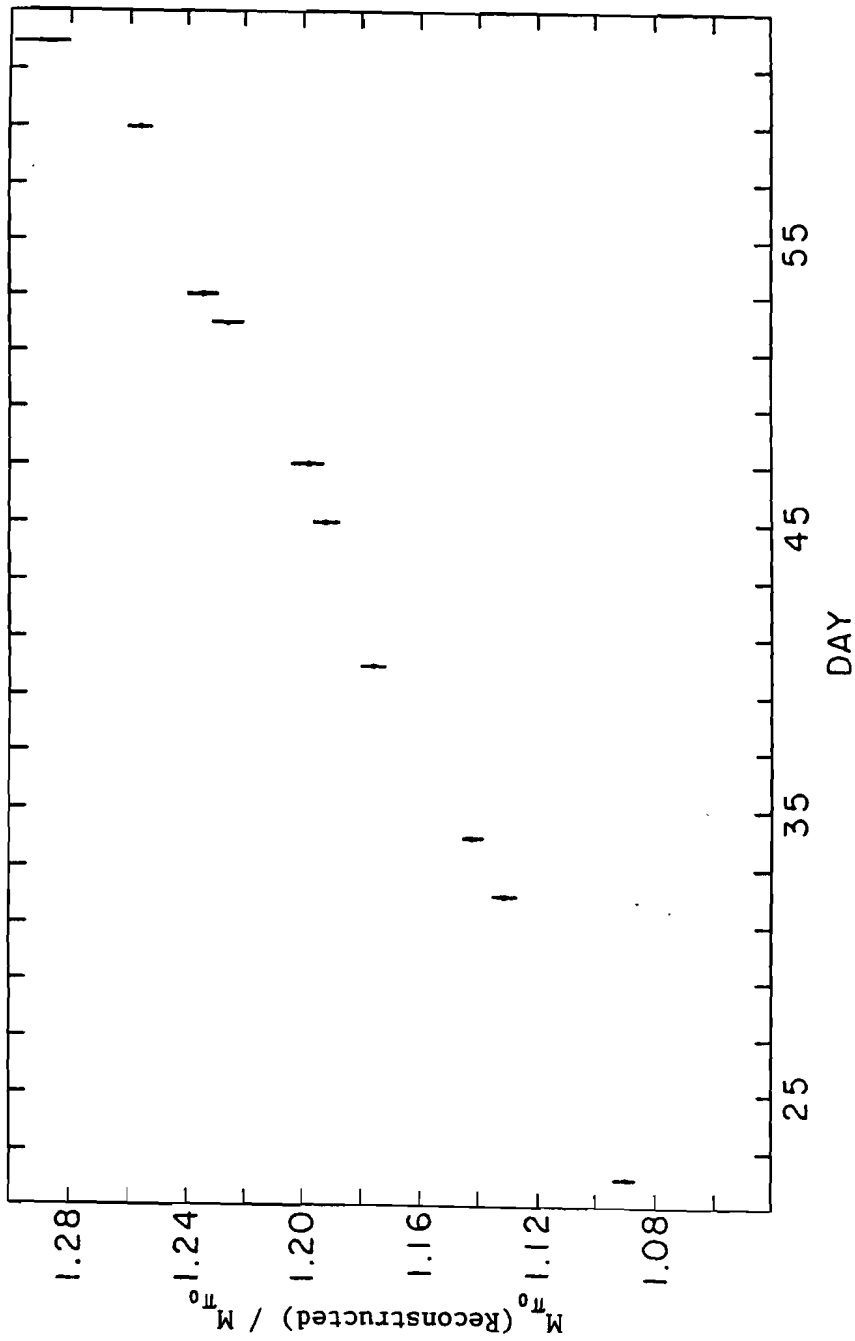
1.28
1.24
1.20
1.16
1.12
1.08
M_{π^0}(Reconstructed) / M_{π^0}
25
35
45
55
DAY

Figure 18

determined by the spectrometer. This increase in the reconstructed LAC shower energies and the known stability of the gains implied an increase in the LAC pulse height as a function of time. The increase may have been due to the slow freezing out of some electronegative impurity in the liquid. The time dependence was applied to the calibration constants determined by the 50 GeV/c eletron calibration, and it was included in the final calibration file.

The response of the LAC to hadrons was investigated by using the π^-'s from the $K^+ \rightarrow \pi^+\pi^+\pi^-$ decay. The different charges of the decay products isolated the π^+ from the two other particles. From this data it was determined that ~36% of the hadrons that hit the LAC interacted in the LAC. The energy distribution of the hadrons which did interact is shown in figure 19 a. Figure 19 b shows the distribution of the ratio of the energy deposited in the back of the LAC versus the total LAC energy. Curves for both the 50 GeV/c electron calibration data and the π^- hadronic studies are shown in this figure. The information from these curves and the shower shape were used to simulate the response of the detector to hadrons in the Monte Carlo model of the experiment.

Alignment of the LAC was determined by the positrons from Ke3 decays and π^+-e^- data. The position at the LAC of the charged lepton was extrapolated from the spectrometer drift chamber information. This position was then compared to the position reconstructed from the pulse distribution in the LAC. Figure 20 shows the difference between

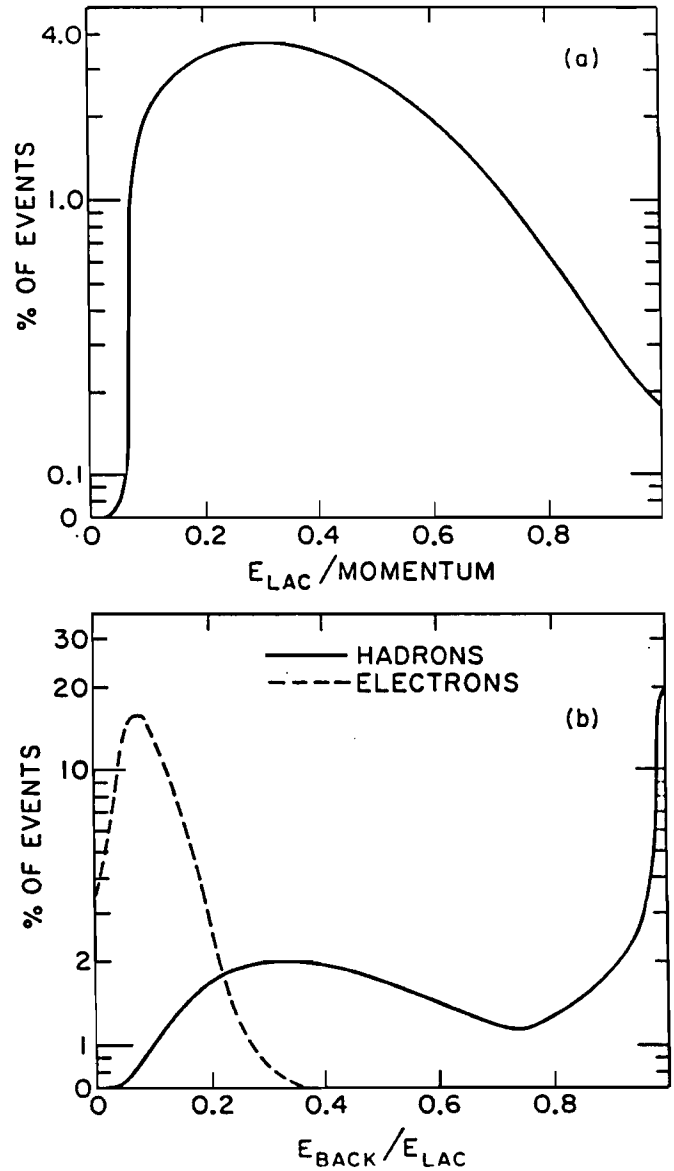
4.0
1.0
0.1
0
% OF EVENTS
(a)
0
0.2
0.4
0.6
0.8
E_LAC /MOMENTUM
30
20
10
2
1
0
% OF EVENTS
HADRONS
ELECTRONS
(b)
0
0.2
0.4
0.6
0.8
E_BACK /E_LAC

Figure 19

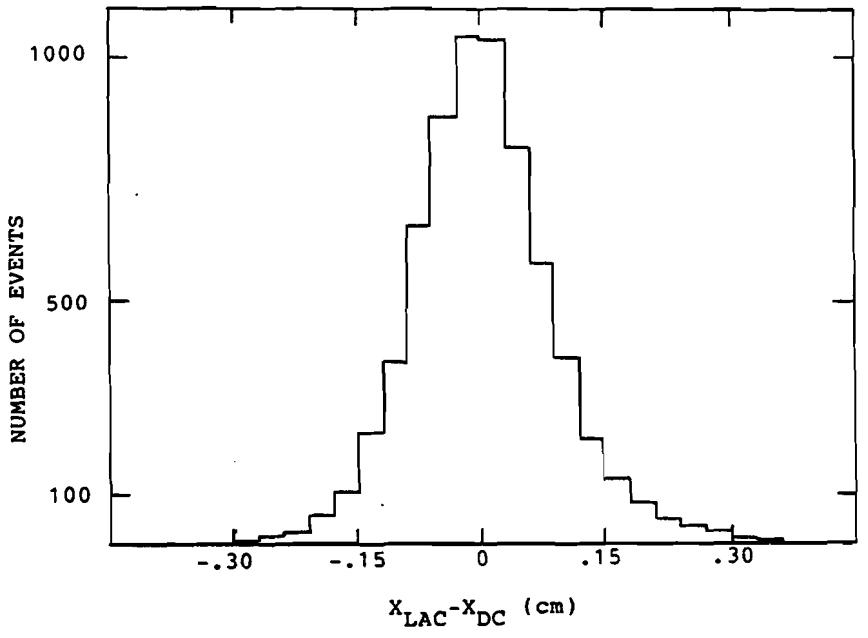

Figure 20

these two positions. By adjusting the expected Z position of the LAC, the centroid of this distribution could be changed. This test was sensitive enough to align the position of the LAC to 1.0 mm in X and Y.

IV. Data Analysis

A. Overview

The E-272 data run collected 7.5×10^6 triggers which were written onto 300 tapes at 800 bpi. The first step in reducing the data to a manageable form was separating the calibration and event data. The calibration data from each tape was then processed by the method described in the previous chapter. The calculated calibration constants were stored on a disk file and the appropriate set was applied during the reconstruction of each tape.

The reconstruction was done on a CDC CYBER-175 system at Fermilab and produced one 6250 bpi tape, called a "summary tape", for every input or "raw" data tape. The events from each tape were reconstructed, and the following were written onto the summary tape: the trajectories and momenta of the charged particles, positions and

energies of the photons, and the original input data.

Subsequently, the events on the summary tapes were sorted according to trigger and target type and were written onto "super summary tapes". These tapes contained all the information present on the summary tapes. These tapes were processed again, and only the information necessary to calculate physical quantities was kept. In this form, all the triggers for a particular target were written on one or two tapes which were called "physics tapes".

The reconstruction process divided naturally into two independent parts, charged particle track reconstruction and photon reconstruction. The same programs were used for all triggers.

B. Charged Track Reconstruction

The performance of the drift chamber system directed the philosophy of the E-272 charged track reconstruction program. All of the E-272 events studied were produced at low -t. In addition, final state particles often remained close together upstream. The result of this was the loss of upstream hits due to low beam region efficiency and the single hit capability of the TDC's. As the charged particles passed through the magnet their trajectories were changed. Downstream of the magnet particles rarely occupied the same drift chamber cell

and were bent out of the beam region. The inherent efficiency of a drift chamber plane outside of the beam region was >97%. Consequently, a nearly complete set of hits was available downstream of the magnet. This led to a reconstruction scheme which first found a complete set of potential tracks downstream of the magnet. After the set was identified an attempt was made to find upstream tracks using the downstream tracks as part of the known information.

Downstream reconstruction involved finding hits in at least two of the three available downstream projections, X, U, V, which would lie on a line. Simple hit counting determined which of the projections was the least efficient. Bunches were made in the two more efficient projections by looking for hits in a staggered doublet which were within 2 cm of each other. A hit in one plane should have had a corresponding hit in its staggered partner. The separation in Z between the planes of a staggered pair was 7.6 cm. The resulting angular resolution was sufficient for a pair of hits from a bunch to predict the position of a corresponding bunch in the same projection at the other drift chamber station. Thus, a list of lines and corresponding hits were accumulated.

These lines were then compared and matched by checking the remaining downstream projection and the upstream Y chamber information. This process yielded a list of downstream tracks. A check was made to insure that hits in the P2 proportional chamber were present for each track. All the hits were combined and a fit yielded

a downstream track's coordinates, slopes, and chi-squared. Based on the chi-squared and the number of hits involved, each track received a quality value. Next, the hit lists of the downstream tracks were compared. If a hit was shared by more than one track, the quality values for these tracks were compared and the track with the lowest quality value was removed from the list.

The magnetic field of the BM109 deflected charged particles horizontally. Because the field was very uniform, the trajectory of a charged particle could be approximated by two straight lines that intersected at the center of the magnet. This midpoint provided one starting point for the analysis of upstream tracks.

Each downstream track was traced to the center of the magnet. From there, each downstream track was assigned a upstream track for each hit in the P1X proportional chamber. The total number of hypothetical tracks was the number of downstream tracks multiplied by the number of P1X hits.

Hit lists were now made for these new tracks. All hits within 0.76 cm of a track were assigned to that track. To fit and assign a chi-square to these tracks was impractical because of the many hits which were shared by these hypothetical tracks in the upstream region. For this reason, a weighted fit was performed. The weight function chosen was a Gaussian which depended on the distance between the hypothetical track and the hit positions. The initial σ was 0.76 cm. With this value a weighted fit was performed thus determining new

intercepts and slopes for each track. σ was now reduced by 1/4. The weighting and fitting was done using the new track parameters. This cycle was repeated till σ reached a predetermined cut off.

Next, the requirement that no two tracks share the same hits was applied. Track hit lists were compared two at a time. When a hit was shared by both of the lists the track with the lower weight had the hit removed. This was done for half the shared hits and a new fitting iteration was performed. A hypothetical track was eliminated when its hit list was reduced to a specified number of hits. This cycle was repeated until the remaining tracks no longer shared any hits. At this point all hits with weights less than 1/e were removed from a track's list. A final fit was performed with all the remaining hits' weights set to 1.

In a separate routine, the reconstruction program fit straight lines to the hits in the beam chambers, J1 and J2. If more than one beam track hypothesis was avaliable the track deviating the least from the Z axis of the spectrometer was chosen and the event was flagged as having multiple beam tracks.

Using $K^+ \rightarrow \pi^+ \pi^0$ decays it was found that the K^+ beam track could be linked with an outgoing track about 95% of the time. About 1% of the loss was due to chamber inefficiency, while the remainder resulted from the strictness of the program's track finding criteria.

C. Photon Reconstruction

The positions and energies of photons were calculated by the gamma reconstruction program. The raw data contained the address and counts of any LAC amplifier which had been above the preset threshold level of §300 MeV. The reconstruction program converted these digital signals into energies by subtracting the pedestal levels and multiplying these results by the conversion factors. Both the pedestal levels and conversion factors were part of the calibration file discussed earlier. A minimum energy of 450 MeV was required for any channel to be considered further.

There were two stages to photon reconstruction. During the first stage the X and Y views were treated independently. A search was made in each view for channels above threshold in the front half of the detector. Within each group of strips above threshold peaks were found. A peak was one channel which registered a higher energy than the adjacent channels. Each peak within a group was separated from the others by use of the shower shape. These separated peaks were called "gammas" and were assigned energies and positions based on the energies of the three central strips of the peak. Gammas which had energies less than 2.4 GeV were eliminated in the next stage of the program.

The next stage of the program correlated the gammas found in the two views of the detector. The LAC was finely segmented in the Z direction with X and Y read-out planes interleaved. A photon striking the detector would have deposited equal amounts of energy in each view. The program searched for gammas which had energy differences in a particular range. When an X and Y gamma were found to meet this criteria they were removed from further consideration, and the search was repeated looking for correlations with a larger energy difference.

This correlation procedure worked best when the gammas were well separated in both views but often events would have showers which overlapped in one view or the other. After all single gammas had been matched, the program attempted to match the energies of two gammas in one view with one in the other. If there was a match, the program would split the single gamma into two gammas which would correlate with the two distinct gammas in the other view.

After all the possible correlations were made, the energies in both views and the corresponding energies deposited in the back half of the detector were added to form the photon energies. The positions of the photons were the same as the positions of the overlapping gammas.

Before the results were written to tape, the photon positions were compared with the extrapolated charged track positions at the LAC. If a photon and a charged track were within 2.5 cm of each other the photon was flagged as a "photon-charged overlap" and as such was a

candidate for an electron or an interacting hadron.

V. Monte Carlo

E-272 was designed to accept a variety of reactions. It was necessary to calculate geometrical and trigger related acceptance factors for each of the processes. This was accomplished by the development of a sophisticated Monte Carlo model of the experiment. This program modeled the performance of each element of the spectrometer and the LAC. In addition, trigger dependent effects had to be included. The performance of many of the trigger elements was often dependent on the final state involved. The variety of monitoring triggers and the presence of well established K decays as components of the Rho, A1, and V triggers made this development a natural step.

To aid in properly modeling trigger elements special "test" tapes were taken throughout the run. For each of these tapes a given element of the trigger was not implemented. This was an effective way

of evaluating the efficiencies of the trigger elements. To verify that these test tapes were taken during typical running conditions the full trigger was implemented by off-line software. The events which passed this reimplemented trigger were then analyzed in identical fashion as the normal data. Comparison of K decay kinematic distributions showed good agreement between the test tape data and the normal data.

A. General Structure

Every attempt was made to guarantee that the Monte Carlo modeled all elements of the experiment. First, a particular reaction was chosen for study. The program generated the kinematic variables for this reaction using the known masses and expected decay-angular distributions of all intermediate and final state particles. Trajectories for the final state particles were projected through a software model of the apparatus. Charged particle trajectories were converted to sets of hits in the proportional and drift chambers. Energy was assigned to the appropriate strips of the LAC. The generated events were then checked against the logic requirements of the appropriate trigger. When an event satisfied a trigger the "raw data" was written to a file.

This process was repeated until a specified number of events had been generated. This file was reconstructed and analyzed by the same procedure used on the experimental data. This allowed for simple and direct comparison between Monte Carlo and experimental event distributions. Sections B. through G. describe in more detail how various elements of the apparatus were modeled. Section H. compares the Monte Carlo and experimental event distributions.

B. Beam Particle

The M1 beamline's final focus (see figure 4) was located 2 m downstream of the target. This focus was located by tracking noninteracting beam particles and finding the minimum spatial extent of the beam spot. In addition to the beam's dimensions in the X and Y directions, the angular dispersions were also noted. The cutoffs of these distributions formed the boundary of a phase space ellipse which was defined in both the horizontal and vertical directions. This ellipse was uniformly filled and the position of a point defined a beam particle's trajectory. The beam particle's mass and charge had to be specified. The particle's momentum was chosen from a Gaussian distribution with a width and mean of the actual beam momentum.

The performance of the beam proportional chambers was studied using the random beam triggers. Each plane was >99% efficient and this performance was modeled by the program. The number of noise hits added to the system was given by a Poisson distribution with a mean of 8. Each noise hit was randomly assigned to a wire of the beam proportional chambers.

C. Event Generation

The Monte Carlo program was structured so as to model any reaction of interest to this experiment. The program required the user to input the masses, charges, and lifetimes of all initial, intermediate, and final state particles. At this time angular distributions, t-distributions, and three particle Dalitz plots could also be specified. This information was used to generate 4-vectors in the center of mass frame. The final state particles were then boosted into the laboratory frame using the information from the generated beam particle.

Multiple scattering of the charged particles passing through the target was simulated by assuming a Gaussian approximation and was based on the radiation length of the target material. The trajectories of the final state charged particles were appropriately changed. The outputs from this stage were the energies, momenta, and

both upstream and downstream trajectories of all final state particles.

D. Geometry

The Z positions of BA, BV, VE, and AM veto counters were measured directly. The X and Y positions were determined by sharp cutoffs seen in the spatial distributions of reconstructed charged tracks at the Z positions of these counters. The Monte Carlo program projected the final state particles through the apparatus and the status of vetos were set accordingly. For neutral particles the geometric acceptance was determined by the magnet aperture and the edges of the LAC. The hole in the center of the LAC was also simulated.

E. Track Counters

In E-272 the track counters (see Chapter II.) were used to trigger on specific hit patterns in the proportional chamber system. To study their performance and to model them correctly in the Monte Carlo program two test tapes were taken: one with the two upstream track counters removed from the trigger and the other with the two downstream track counters removed. All track counter levels were

TABLE 2
Track Counter Error Tables

H \ S	0	1	2	3	4	5
			TC1			
0	?	.06	.0	.0	.0	?
1	?	.91	.06	.0	.0	?
2	?	.03	.90	.10	.0	?
3	?	.0	.04	.87	.17	?
4	?	.0	.0	.03	.80	?
>5	?	.0	.0	.0	.03	?
			TC2			
0	?	.02	.0	.0	.0	?
1	?	.97	.04	.0	.0	?
2	?	.01	.94	.09	.0	?
3	?	.0	.02	.89	.25	?
4	?	.0	.0	.02	.71	?
>5	?	.0	.0	.0	.04	?
			TC3			
0	?	.03	.0	.0	.0	?
1	?	.97	.09	.0	.0	?
2	?	.00	.91	.11	.0	?
3	?	.0	.00	.89	.20	?
4	?	.0	.0	.00	.80	?
>5	?	.0	.0	.0	.00	?
			TC4			
0	?	.02	.0	.0	.0	?
1	?	.98	.04	.0	.0	?
2	?	.00	.96	.03	.0	?
3	?	.0	.00	.97	.04	?
4	?	.0	.0	.00	.94	?
>5	?	.0	.0	.0	.02	?

still recorded and written to the data tapes as part of the latch information.

Off-line a systematic comparison was made between the recorded hardware track counter level and a software count performed by testing the proportional chamber wire hit list. The difference between these two counts indicated the level of the track counter error. From this information a probability matrix was established. Table 2 shows this matrix for each of the four track counters. The columns are the number of software track bunches counted off-line. The rows show the hardware levels for the same events. The diagonal elements of the matrix give the probability for software and hardware agreement.

After hits were assigned to the tracks of a Monte Carlo event the program counted the number of bunches and generated track counter outputs based on this probability table. These outputs were then checked against the track counter trigger logic to see if the event should be vetoed.

F. MBV Simulation

The MBV, like the track counters, could only be modeled effectively by studying data where the MBV was out of the trigger. The MBV was not part of the logic for the beam triggers or the A1 trigger. In addition, a test tape was taken for each of the three remaining data triggers with the MBV removed. The efficiency for vetoing noninteracting beam particles was about 90%. This efficiency was the product of three effects: proportional plane efficiency, logical inconsistancies of the MBV hardware, and beam trajectories outside the acceptance of the hardware logic. The largest part of the 10% inefficiency was due to the last factor and was accounted for in the Monte Carlo program by the distribution of the beam tracks chosen (see Section B.).

The first step in modeling the MBV was establishing a table which used beam proportional chamber hits to predict the wire hit in P1X. This table was taken directly from the hardware wiring of the experiment. The logical inconsistancies were studied using the beam triggers. Off-line the MBV veto signal was predicted by looking at the hits in the beam chambers and P1X. The table was then used to predict the status of the MBV veto. This software "signal" was compared to the latched hardware signal which had been written to tape. This study showed that the hardware signal agreed with the software analog 99% of the time. So the MBV was modeled in a straight

forward fashion by using this table to correlate hits and applying a 1% random failure.

G. Chambers

Correctly modeling the proportional chambers was a critical element in modeling the performance of the MBV and track counters. The chamber edges and wire positions were determined from the same alignment file which was used by the reconstruction program. The Monte Carlo program assigned a hit to the wire of each plane closest to the charged particle track. Two adjacent wires would fire if a trajectory passed through a 0.1 mm region centered between two consecutive wires in a plane. The proportional chambers were assigned overall efficiencies with no special effects in the beam region.

As with the beam proportional chambers the number of noise hits assigned to an event was given by a Poisson distribution with a mean of 8. The noise was randomly assigned to the wires of the spectrometer's proportional chambers. This noise level was adequate to describe the level of extra hits when the chambers were well behaved but it did not allow for any unusual behavior by the proportional chambers. Unusual behavior could not be studied when the full trigger was implemented because it typically boosted one of the track counters to ≥5 bunches. Noise of this type resulted in the loss

of good events. The problem was studied using the two track counter test tapes mentioned above. These tapes showed this noise effect to be insignificant for one charged particle final states. It was, however, a major correction for three charged particle events. This correction is discussed in more detail in the next chapter.

The drift chambers posed a different problem. Their efficiencies were radically affected in the beam region dipping as low as 20%. A study was done using the various K decays to study the drift chamber performance outside of the beam region while beam triggers were used to study their beam region efficiency. This study resulted in the development of a model [17]. This model expressed the efficiency of a particular region of a plane as an exponential function of the local instantaneous beam intensity. The input parameters for this model were the nominal beam intensity, the intensity at which a drift plane's efficiency fell by 1/e, and the efficiency of the plane far from the beam region. The last two parameters were determined on a plane by plane basis.

The model was used by transporting the initial beam phase space to the appropriate Z position of a particular drift plane. From this information the program determined the local intensity of a given spot on a plane and thereby the efficiency at that spot. This efficiency was used to determine the probability of keeping any hit in that

[17] "A Measurement of the Pion Electromagnetic Charge Radius by Pion Electron Scattering." Thesis by Steven Heppelmann, University of Minnesota 1981.

region.

Once a hit was accepted the Monte Carlo program assigned a "mirror" hit on the other side of the drift chamber wire to mimic the two-fold ambiguity of a drift time. The positions of these hits were then smeared by using a Gaussian with a width of σ=0.33 mm. This resolution was determined by measuring the deviation of the individual chamber hits from the reconstructed tracks of $K^+ \to \pi^+ \pi^0$ and $K^+ \to \pi^+ \pi^+ \pi^-$ decays.

If there were more than one hit in a drift chamber cell the Monte Carlo program was set up to duplicate the single hit capability of the TDC units. This included the modeling of the 100 ns dead time of the drift chamber amplifiers.

Next noise hits were added. The drift system was quieter for one track events like $K^+ \to \pi^+ \pi^0$ than three track events. Consequently, the noise for the drift chambers was modeled differently for these two cases. For one track events a Poisson distribution with a mean of 8 was used to add random hits. For three track events the distribution of extra random hits was fit by an exponential C*exp(A*N). A and C are the parameters being fit and N is the number of extra hits for a particular event. The fit yielded A=-0.18 and C=0.96. The exponential was then inverted and the number of noise hits was assigned used the expression Y=(-5.6*ln(X)). X was assigned a random value from 0 - 1. The corresponding Y value was truncated and the resulting integer was the number of noise hits which were assigned to

random wires in the drift system. These distributions were chosen by studying the distribution of drift hits for successfully reconstructed $K^+ \to \pi^+ \pi^0$ and $K^+ \to \pi^+ \pi^+ \pi^-$ events.

H. Liquid Argon Calorimeter

First, the Monte Carlo program established the positions of the LAC detection strips by using the reconstruction alignment file. The trajectories of all final state particles were traced to face of the LAC. Here the shower shapes for electrons and pions (see figure 19 b) were used to convert the energies of the particles which interacted into energy on a strip. Care was taken to model the different front/back ratios of the electromagnetic and hadronic showers and to duplicate the probability of a hadronic interaction. Once the energy was assigned to the strip it was given an rms jitter of $\sigma = 0.14/\sqrt{E}$. Energy leakage near the hole was also simulated.

There were two types of noise contributions. One type of noise was studied using between spill calibration events. Occasionally random strips were above threshold when the LAC was read out. The second type of noise was associated with the beam and affected the amplifiers nearest the LAC hole. This was modeled by studying noninteracting beam particles from the beam triggers.

I. Monte Carlo and Data Comparison

The chief tool for studying the performance of the spectrometer were the various K^+ decays. There were approximately 1000 $K^+ \to \pi^+\pi^0$ events, 50 $K^+ \to \pi^+\pi^+\pi^-$, and 10 Ke3 decays per tape. A tape contained about 25,000 triggers. $K^+ \to \pi^+\pi^0$ and Ke3 decays were used to study the LAC while the charged particles from all the decays provided information for modeling the spectrometer. Table 3 lists the cuts used to define the sample of $K^+ \to \pi^+\pi^0$ and $K^+ \to \pi^+\pi^+\pi^-$ decays used in this section. The structure of the Monte Carlo program allowed the generated events to be analyzed by the same kinematic programs used on the real data. In the following figures the solid lines represent the normalized Monte Carlo predictions. Agreement between measured and predicted quantities was essential to demonstrate our understanding of the experimental apparatus.

Figure 21 shows the vertex distributions for $K^+ \to \pi^+\pi^0$ decays. These decays were a subset of the data taken by the Rho trigger. The vertex of the decay was defined by the intersection between the incident beam particle and the outgoing charged particle trajectories. The dip seen in the data near the target region was due to the presence of the various veto counters. These counters were not included in the Monte Carlo model since the target region could be avoided in the $K^+ \to \pi^+\pi^0$ normalization procedure (see Chapter VI.). The fall off at the downstream end of the distribution is caused by the

Table 3

Cuts Used to Define $K^+ \to \pi^+ \pi^0$ Decays

a) Rho Trigger
b) Kaon Cerenkov
c) 1 Beam Track
d) 1 Track in Final State
e) 2 Photons in Final State
f) Decay Vertex 100 - 400 cm (Normalization Region)
g) Reconstructed Final State Energy 192 - 212 GeV
h) Reconstructed t t<0.005 (GeV/c)
i) Reconstructed π^0 Mass 0.110 - 0.160 GeV
j) Reconstructed K^+ Mass 0.450 - 0.550 GeV

Cuts Used to Define $K^+ \to \pi^+ \pi^+ \pi^-$ Decays

a) A1 Trigger
b) Kaon Cerenkov
c) 1 Beam Track
d) 3 Tracks in Final State
e) Decay Vertex -250 - 250 cm (Normalization Region)
f) Reconstructed Charged Track Energy 192 - 212 GeV
g) Reconstructed Charged Track t t<0.01 (GeV/c)
h) Reconstructed K^+ Mass 0.450 - 0.550 GeV

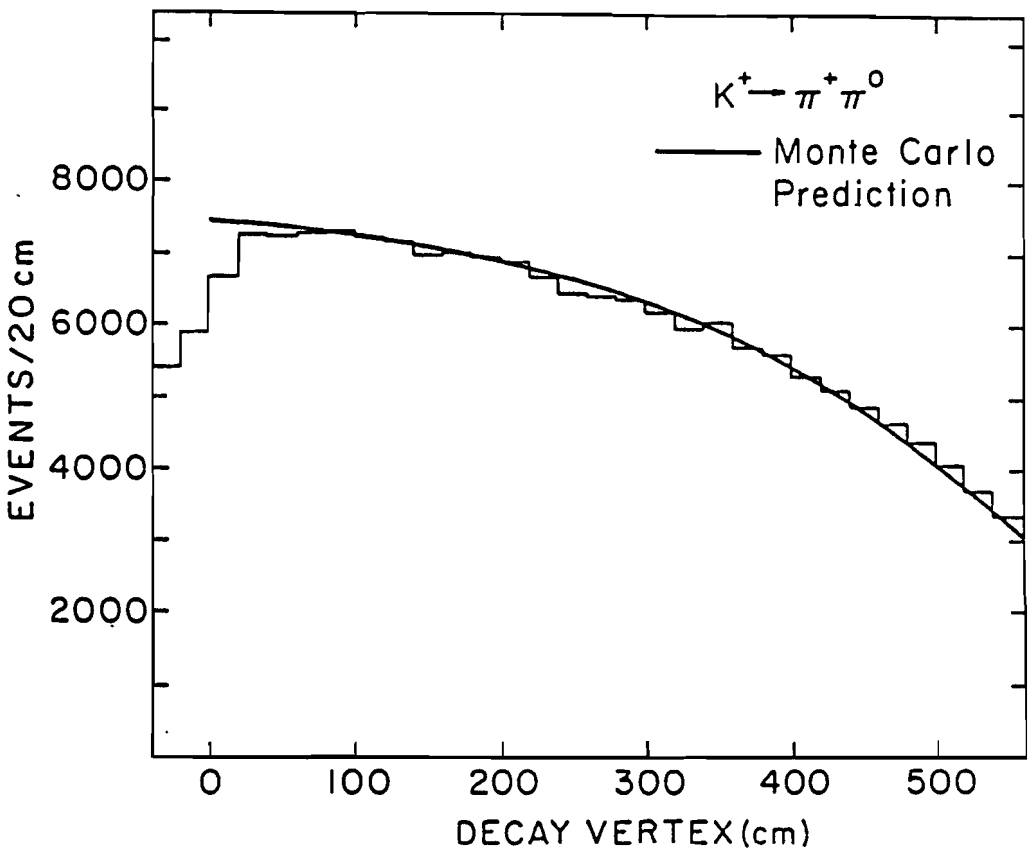
$K^+ \to \pi^+ \pi^0$
Monte Carlo Prediction
8000
6000
4000
2000
EVENTS/20cm
0
100
200
300
400
500
DECAY VERTEX (cm)

Figure 21

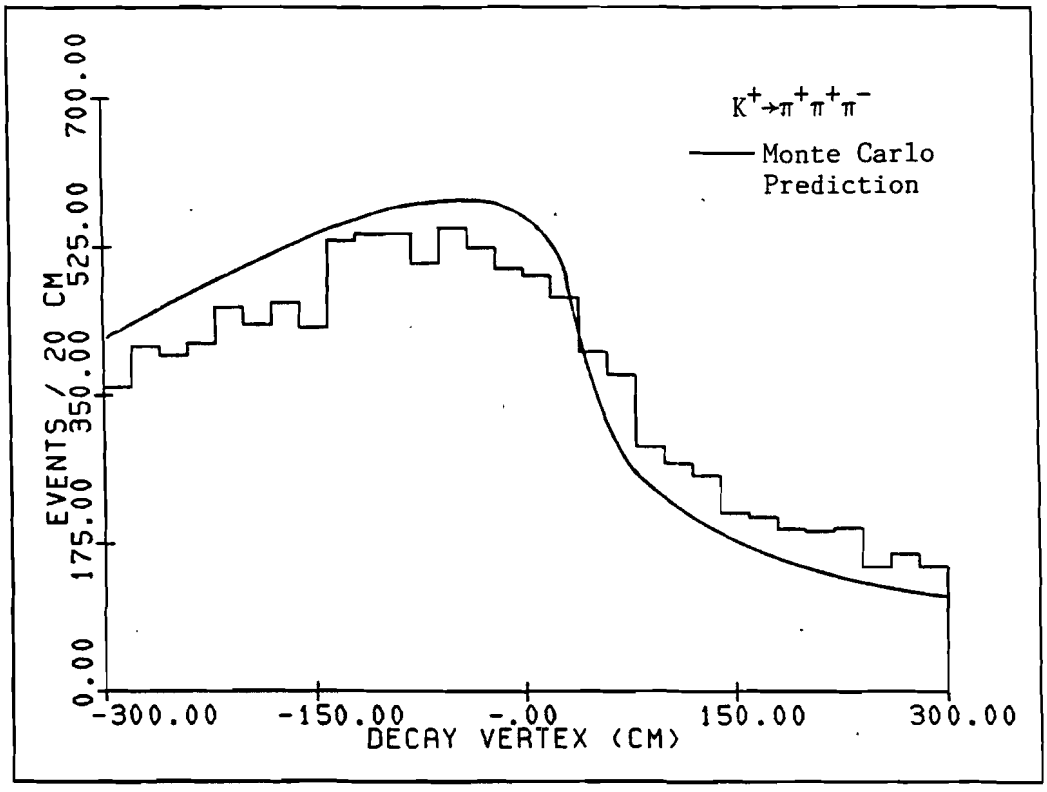
$K^+ \to \pi^+\pi^+\pi^-$
Monte Carlo Prediction
EVENTS / 20 CM
0.00
175.00
350.00
525.00
700.00
-300.00
-150.00
-.00
150.00
300.00
DECAY VERTEX (CM)

Figure 22

MBV2 veto.

Figure 22 shows the vertex distribution for the $K^+ \rightarrow \pi^+\pi^+\pi^-$ decays in the A1 trigger. Because of the A1 S counter trigger requirement of three charged particles the majority of the $K^+ \rightarrow \pi^+\pi^+\pi^-$ decays occurred in the target region. The sharp drop at 7 cm in this figure is caused by this requirement. Only kaons which decayed upstream of this point should have satisfied this condition. The events downstream of the S counter position came from two sources. First, some of the decays which actually occured upstream of the S counter were incorrectly reconstructed and resulted in a vertex assignment downstream of the S counter. The second contribution was from kaons which had not decayed before reaching the S counter. Some of these particles would give a large pulse height which satisfied the S counter requirement (high energy tail of the Landau energy loss distribution). This contribution was modeled by studying the S counter pulse distribution of random beam particles. From this distribution it was determined that 7% of the kaons had a pulse height greater than the three track cutoff.

Figure 22 also shows severe losses upstream of the target. These losses are due to the BH and H counters which defined the beam in the region immediately around the target. When a beam kaon decayed the resulting pion trajectories deviated from that of the beam particle. As this decay occured further upstream it became increasingly likely that one of the decay pions would have moved out of the beam and

struck one of the veto counters. To reproduce the $K^+ \to \pi^+\pi^+\pi^-$ vertex distribution upstream of the target, the positions of these counters had to be accurately known relative to the beam. This was complicated by two separate shifts of the positions of these counters during the run. In addition, the H counter was dislodged during the early runs and vetoed up to 30% of the incident beam. This was not corrected until approximately half of the data had been taken. The positions of the counters and the relative beam count had to be determined for each of these running periods.

The positions of the counters were determined by studying both random BA and $\overline{BA}$ triggers. Events which had a positive H counter latch signal were chosen for study. The beam particle trajectories of these events were projected to the appropriate Z position of these counters. The X and Y position of each event was noted and the resulting shadows located the positions of these counters in space. These counters were inserted as an extra cut on the generated Monte Carlo kaon decays.

In spite of this care, the Monte Carlo curve only crudely agrees with the data. This discrepancy is the result of generating Monte Carlo events with a better spatial resolution than the data. The Monte Carlo drift chamber resolution could have been tuned to match these vertex distributions, but drift chamber resolution also affected the t and momentum resolutions. Matching any of these distributions could adversely bias another. Because of this, the resolution of

σ=0.33 mm, determined by direct comparison of track and hit position, was used.

Figures 23 and 24 show the total summed energy of the final state particles for $K^+ \to \pi^+ \pi^0$ and $K^+ \to \pi^+ \pi^+ \pi^-$ decays. The momentum spread of the beam was designed to be <1% hence, the widths of the distributions were determined by the resolution of the spectrometer.

The 2-photon mass distribution for $K^+ \to \pi^+ \pi^0$ decays is shown in figure 25. As stated in Chapter III. each photon had an energy of at least 5 GeV. The Monte Carlo prediction is somewhat narrower than the data. For the Monte Carlo σ=4.7 MeV and for the data σ=5.5 MeV. The cause of this discrepency is not clear. It may have been due to difficulties in relating the electromagnetic shower shape, determined at 50 GeV (see Chapter IV.), to a wide range of energies. Since the Monte Carlo model used the same shower shape for generation as was used in the reconstruction program, the resolution would necessarily be expected to be better. Figure 26 shows the distribution of the π^0 energy asymmetry variable $A = |E1-E2| / |E1+E2|$. E1 and E2 are the energies of the two π^0 photons. Since the π^0 is a spin 0 object the asymmetry variable should be flat. The fall off at high asymmetries is primarily due to one of the photons dropping below the 5 GeV reconstruction energy cutoff.

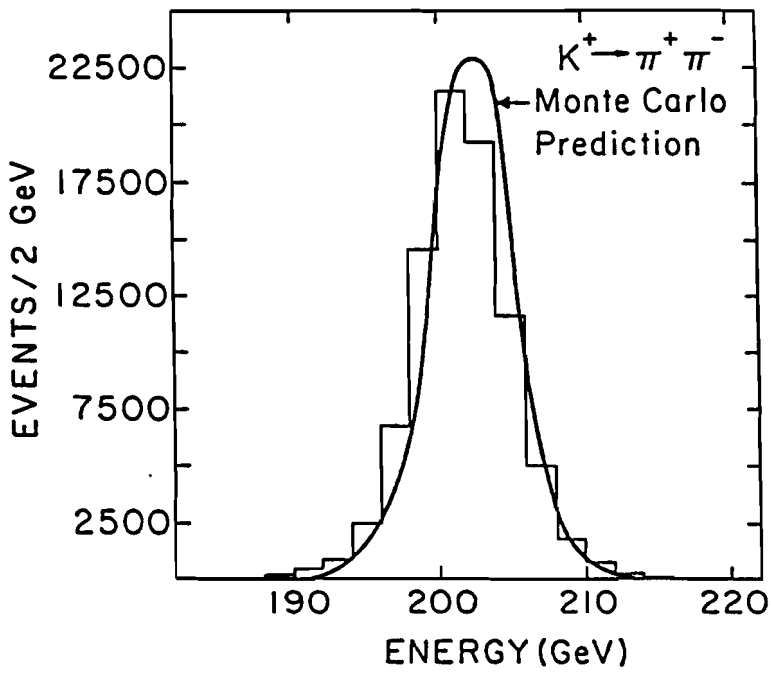

Figure 23

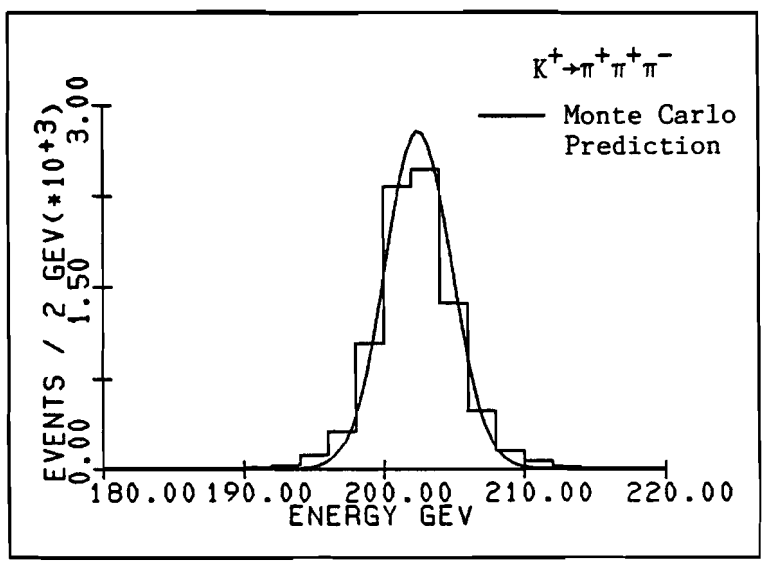

Figure 24

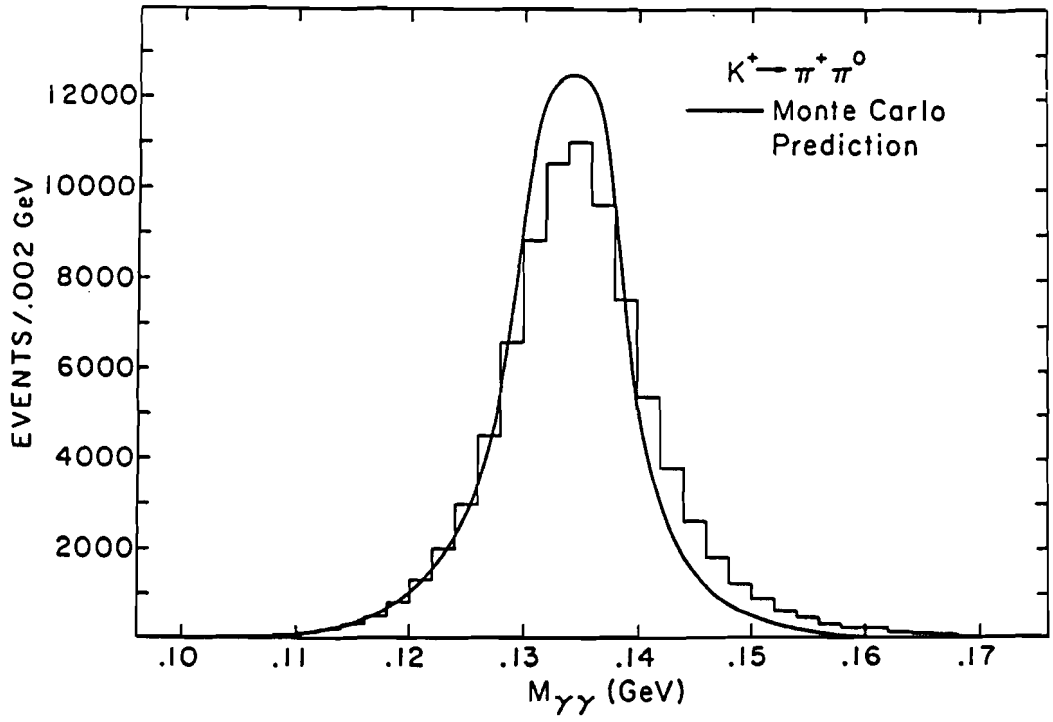

Figure 25

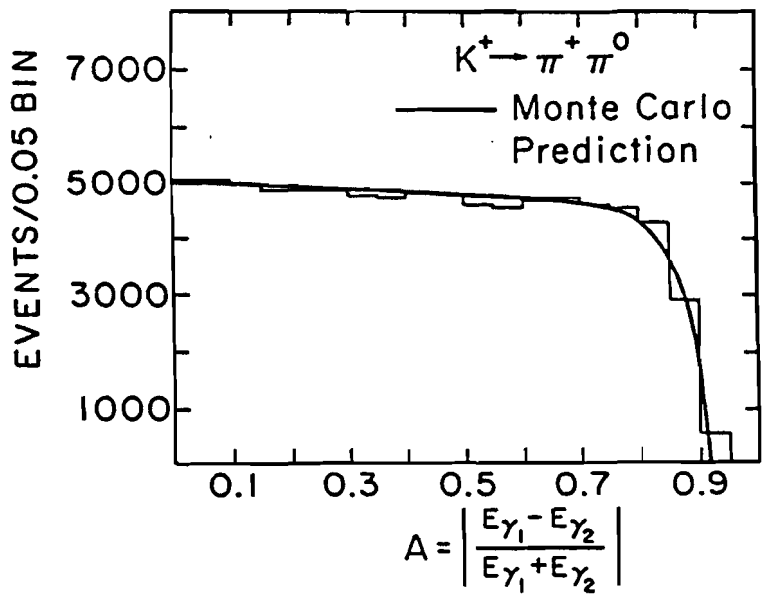

Figure 26

Figures 27 and 28 show the mass distributions for $K^+ \to \pi^+\pi^0$ and $K^+ \to \pi^+\pi^+\pi^-$ decays. The mass standard deviations are 8.5 MeV and 8.0 MeV respectively.

Figures 29 and 30 show the t-distributions for $K^+ \to \pi^+\pi^0$ and $K^+ \to \pi^+\pi^+\pi^-$ events. Since the K decays occured at t=0.0 any slope in the reconstructed t distribution would be due to the finite resolution of the spectrometer. If a Gaussian resolution is assumed the t-distribution for these decays has the form

$$N(t) = N_0 \exp(-t/2\sigma^2)$$

where σ is the resolution of the transverse momentum of the spectrometer (See Appendix B for more details.). Table 4 lists the results of these fits for both the data and Monte Carlo distributions. The solid line Monte Carlo slopes in figures 29 and 30 were drawn using the values listed in this table. Agreement between Monte Carlo and data is good, but again the resolution obtained in the Monte Carlo is somewhat better. The differences in slope between the targets are due to multiple scattering and target thickness.

In both figures there is an excess of data events relative to the Monte Carlo prediction at larger values of t. At these higher values the Gaussian approximation does not work as well. In addition, there is some background from other decay modes. For $K^+ \to \pi^+\pi^0$ events this is caused by Ke3 decays which were not eliminated by the total energy cut. For $K^+ \to \pi^+\pi^+\pi^-$ decays the excess is due to $K^+ \to \pi^+\pi^0$ decays where the π^0 undergoes a Dalitz decay ($\pi^0 \to e^+e^-\gamma$). Again if the photon were

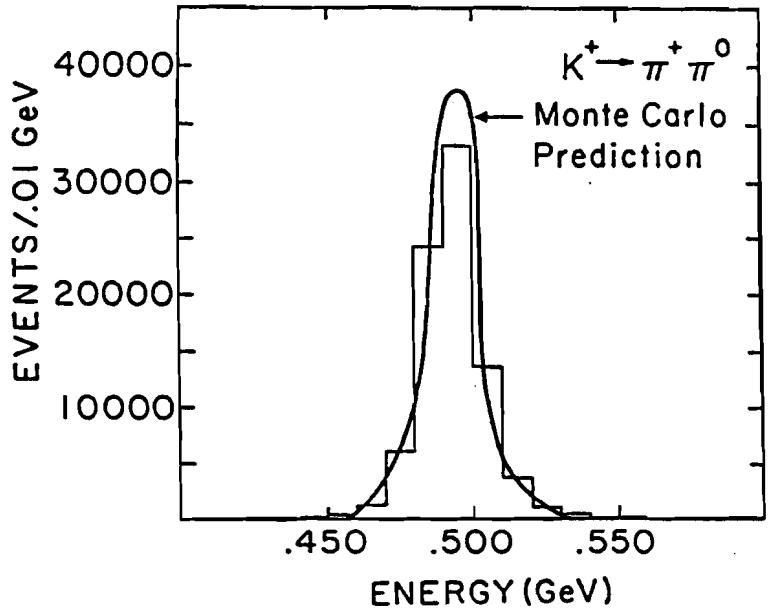

Figure 27

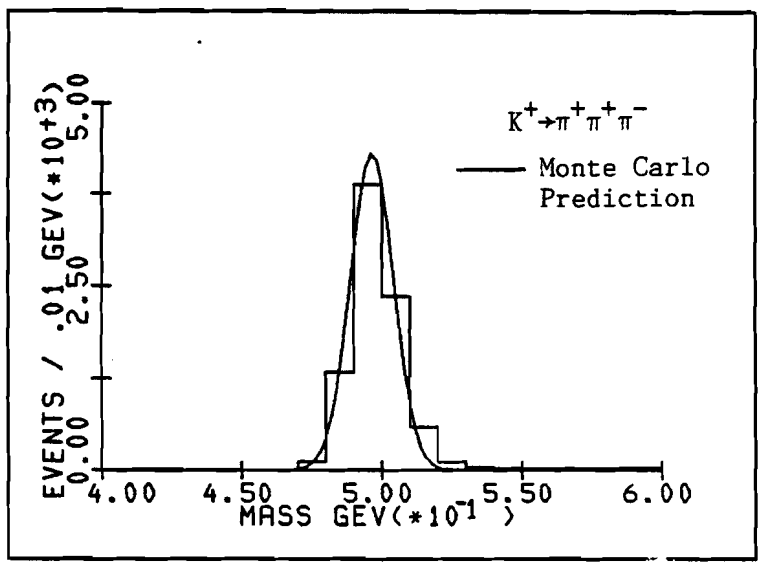

Figure 28

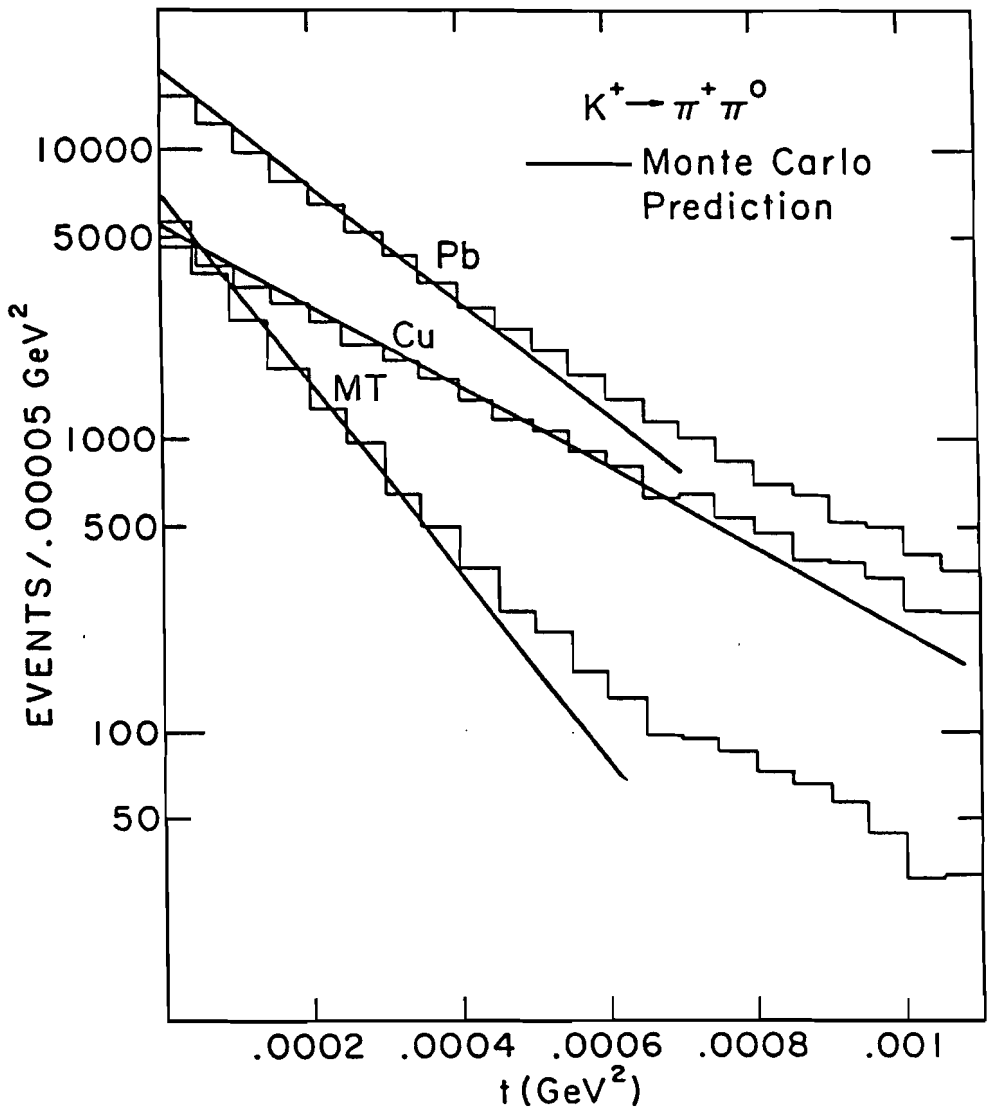
$K^+ \rightarrow \pi^+ \pi^0$
Monte Carlo Prediction
Pb
Cu
MT
10000
5000
1000
500
100
50
EVENTS/.00005 GeV^2
.0002
.0004
.0006
.0008
.001
t (GeV^2)

Figure 29

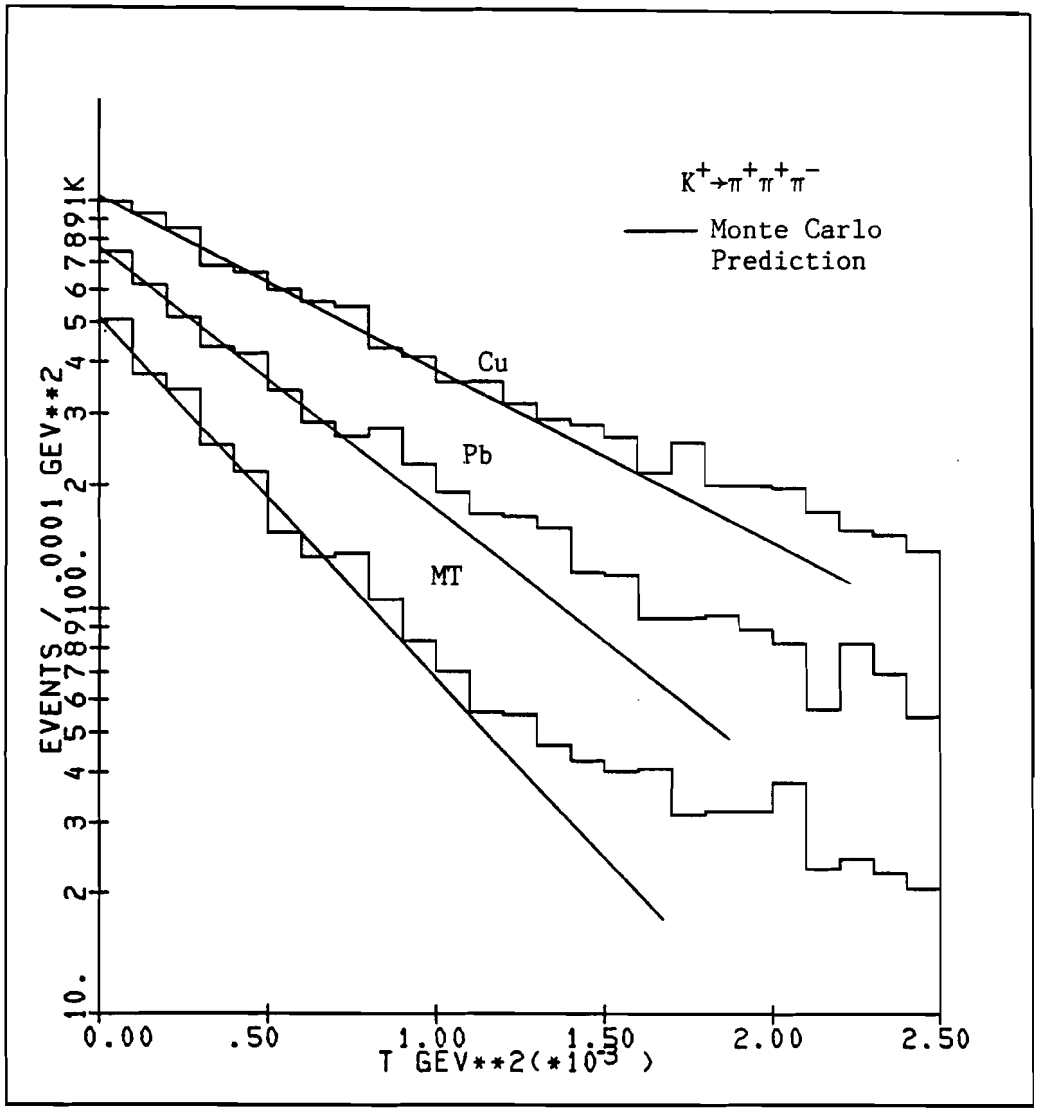
$K^+ \to \pi^+\pi^+\pi^-$
Monte Carlo Prediction
Cu
Pb
MT
EVENTS / .0001 GEV**2
10.
100.
1K
0.00
.50
1.00
1.50
2.00
2.50
T GEV**2(*10^{-3})

Figure 30

Table 4

Resolution in p_t for $K^+ \to \pi^+ \pi^0$ decays

Target	σ_{MC}(MeV)	σ_{Data}(Mev)
MT	7.8	8.6
Cu	12.	13.
Pb	9.8	11.

Resolution in p_t for $K^+ \to \pi^+ \pi^+ \pi^-$ Decays

Target	σ_{MC}(MeV)	σ_{Data}(MeV)
MT	12.	14.
Cu	22.	24.
Pb	18.	19.

of sufficiently low energy these events would pass all of the $K^+ \to \pi^+\pi^+\pi^-$ cuts.

Figure 31 shows the angular distribution of the $K^+ \to \pi^+\pi^0$ decays in the helicity frame. The expected distribution is isotropic since the kaon is a spin zero particle. A number of trigger elements conspired to veto events with the charged pion in the forward direction. The charged tracks with small θ were vetoed by the MBV2, BA, and VE counters. In addition, the low energy photons from the π^0 decay tended to be eliminated by the AM counters and the minimum energy requirement of the LAC. Thus the acceptance was a strong function of θ and it is well accounted for by the Monte Carlo program.

Figure 32 shows the $K^+ \to \pi^+\pi^+\pi^-$ Dalitz plots for Monte Carlo and real data. Because of energy and momentum conservation, the energies and directions of the three pions in the decay plane are determined by two independent variables. These variables are T1 and X where $X=(T2-T3)/\sqrt{3}$. T1 is the kinetic energy of the π^- divided by its maximum possible value. T2 and T3 are the corresponding quantities for the two π^+'s with T2>T3. The kaon is a spin 0 object and, consequently, the Dalitz plot is expected to have uniform density. Both the plots in figure 32 satisfy this criterion. The slight departures from a circle are a relativistic effect.

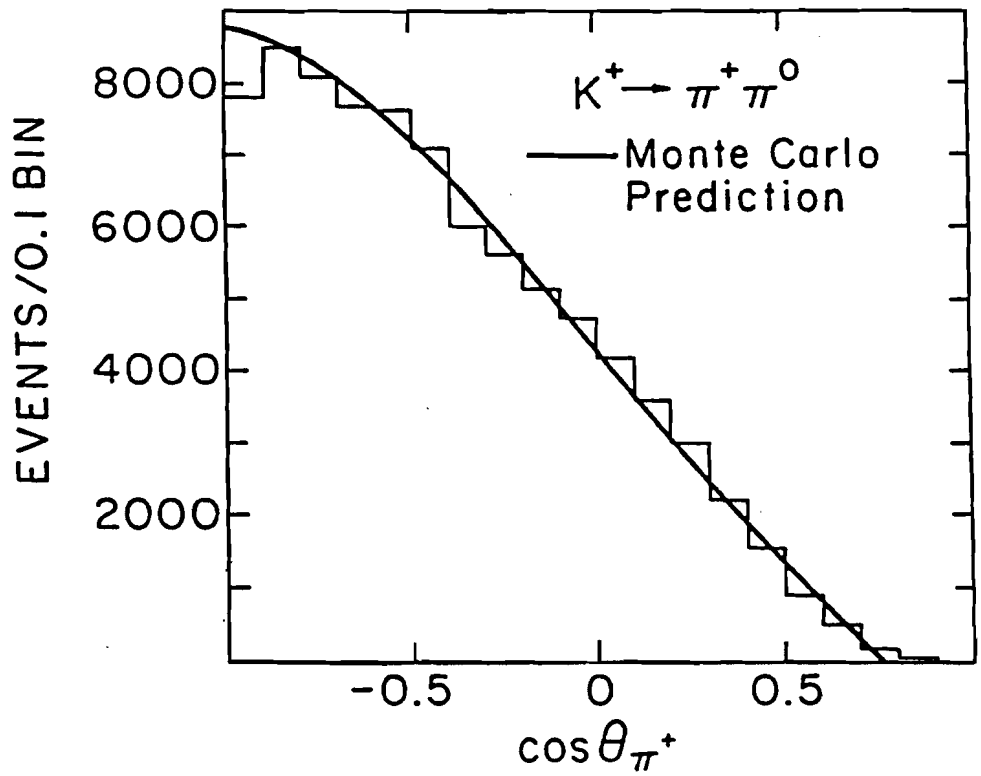
EVENTS/0.1 BIN
8000
6000
4000
2000
$K^+ \to \pi^+\pi^0$
Monte Carlo Prediction
-0.5
0
0.5
$\cos\theta_{\pi^+}$

Figure 31

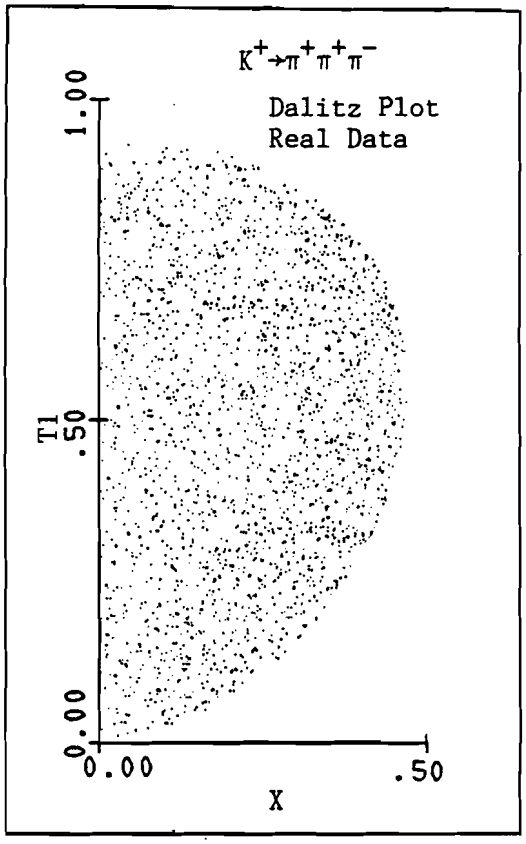
$K^+ \to \pi^+\pi^+\pi^-$
Dalitz Plot
Real Data
1.00
T1
.50
0.00
0.00
.50
X

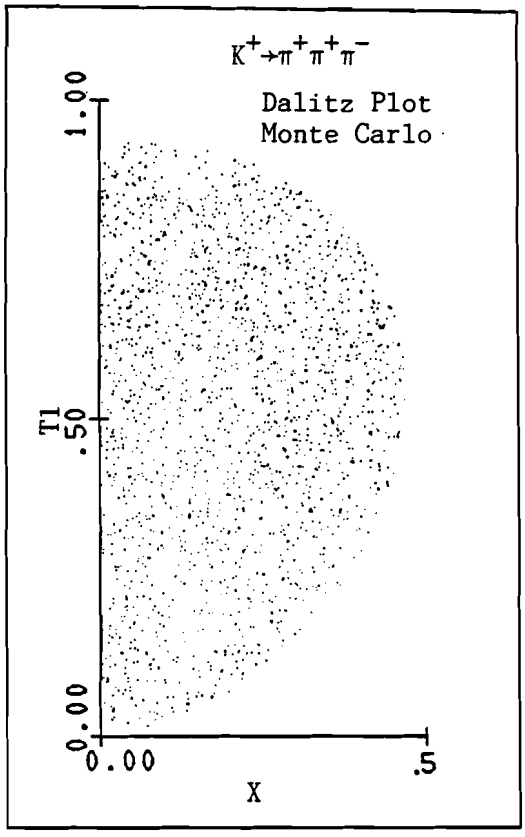
$K^+ \to \pi^+\pi^+\pi^-$
Dalitz Plot
Monte Carlo
1.00
T1
.50
0.00
0.00
.5
X

Figure 32

VI. Normalization

A determination of a radiative width involves the measurement of the Coulomb cross section. This can be seen from equation (13). This chapter discusses the procedure used for normalizing the cross sections measured by this experiment.

The normalization procedure involved careful determination of the incident beam count and of the performance of the spectrometer for a particular final state. The last chapter demonstrated the Monte Carlo model's ability to reproduce kinematic distributions and to provide a measure of the geometrical acceptance and the trigger efficiency of the apparatus. Other corrections had to be applied to take into account factors not included in the Monte Carlo. These effects included veto and Cerenkov counter efficiency, initial and final state absorption, and counter alignment. In principle all these effects could have been incorporated into the model but all of these effects could be measured directly or calculated.

As a final check of the normalization procedure measurements were made of both the $K^+ \to \pi^+\pi^0$ and $K^+ \to \pi^+\pi^+\pi^-$ decay rates. The corrections used were divided into three groups: beam related, target dependent, and spectrometer related.

A. Beam Related Corrections

The definition of a beam particle was discussed in Chapter II. Any beam particle which satisfied the basic beam requirement $BO*B1*B2*B3*\overline{BH}$ supposedly traversed the remainder of the spectrometer without firing any other veto counter. However, an occasional noninteracting beam particle would have an associated veto. These vetos had any one of several sources: delta rays, random noise in any of the veto counters, or a beam halo particle hitting a counter. By studying the BA and $\overline{BA}$ random beam triggers the accidental correlations between an incident beam particle and a spurious veto were directly measured.

The random BA beam trigger, B*BA, sampled ~90% of the noninteracting beam. The remaining 10% of the scaled beam count was sampled by the random $\overline{BA}$ trigger, $B*\overline{BA}$. This latter component of the beam contained the halo of the noninteracting beam, ~5%, beam interactions, ~2.5%, and junk, ~2.5%. This last fraction was dominated

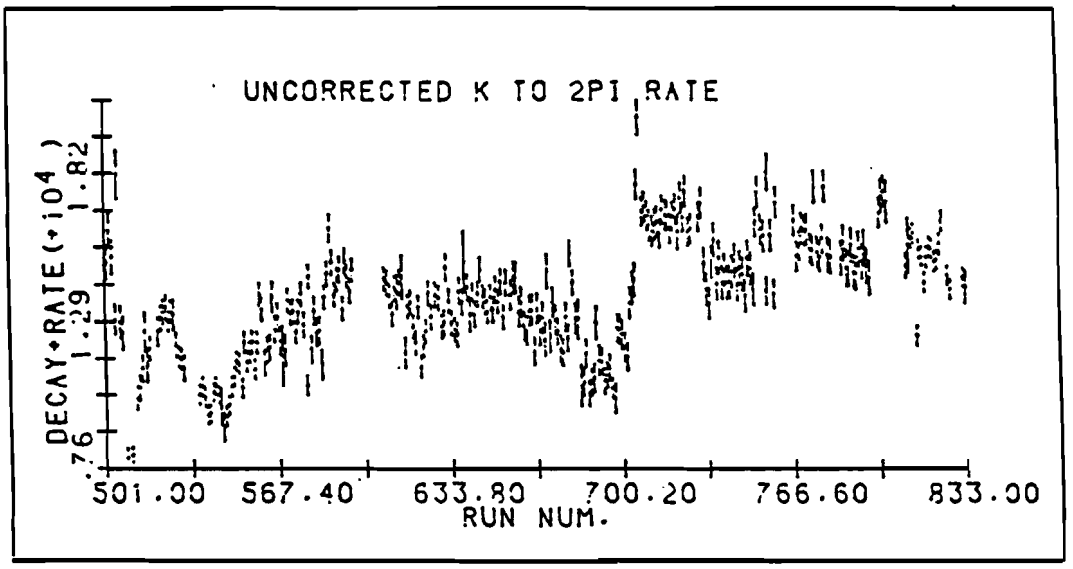
UNCORRECTED K TO 2PI RATE
DECAY*RATE(*10^4)
.76
1.29
1.82
501.00
567.40
633.80
700.20
766.60
833.00
RUN NUM.

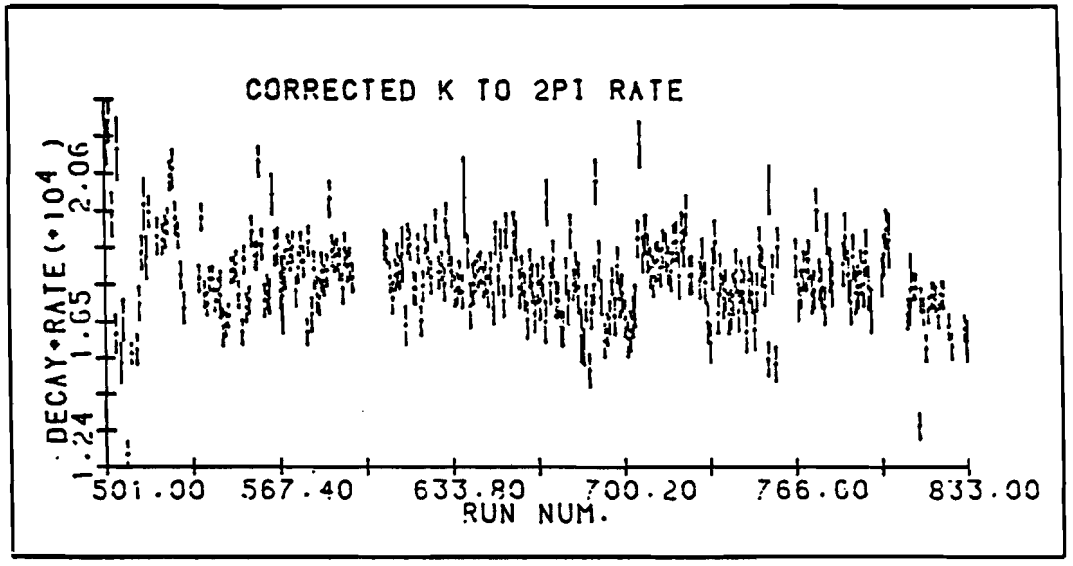
CORRECTED K TO 2PI RATE
DECAY*RATE(*10^4)
1.24
1.65
2.06
501.00
567.40
633.80
700.20
766.00
833.00
RUN NUM.

Figure 33

by events which scattered out of the beamline after the B3 counter. Most of these events had zero hits in the beam proportional chambers, J1 and J2.

The beam veto correction factor was determined by testing the status of the veto counters for each noninteracting beam particle. This beam correction scheme was essential to correct for the dislodged H counter (see Chapter V.). When this counter was repaired the run to run variation in veto corrections was 5%. Figure 33 shows the $K^+ \rightarrow \pi^+ \pi^0$. raw and corrected beam count as a function of run number. These data indicate that the veto correction adequately accounted for the run to run variations.

Along with the veto counters two additional corrections were accumulated on an event by event basis. First, each beam particle was tested for only one beam track. Multiple beam track events could occur when beam particles interacted in the material between B3 and the target. S counter efficiency was also calculated at this time. This efficiency was calculated by testing the S counter ADC and accumulating the fraction of beam particles which registered a signal.

It is important to note that these corrections are not necessarily independent. A beam particle which missed the S counter was also likely to hit one of the other veto counters. Care was taken to insure there was no double counting. In Table 5 the one beam track, random veto, and S counter corrections are listed as one number.

Corrections were applied for misidentification of particles by the Cerenkov counters. From Cerenkov pressure curves it was determined that 0.5% of the pion beam particles were actually kaons and 1.5% of the kaon beam particles were pions. There was also muon contamination. For the kaon beam the source of this contamination was $K^+ \rightarrow \mu^+ \nu$ decays downstream of the kaon Cerenkov counter. A Monte Carlo study showed that this reduced the effective kaon beam flux by 0.4%.

Muon contamination of the pion beam was a different problem. Muons which passed through the pion Cerenkov counter would give a positive signal. Ordinarily this is not a problem. The typical fractions of muons in the M1 beam is ~0.5% [18]. The presence of the beryllium in the beamline enhanced the muon beam fraction relative to the pions. The fraction of the muon beam in the pion beam was measured directly by using a test run with the magnet off. The undeflected beam entered the LAC at a spot about 5 cm to the left of the center hole. The fraction of beam particles which interacted in the LAC was recorded for each particle type. Since the kaon and proton Cerenkov counters were not sensitive to muons a comparison was made of the kaon/proton and pion/proton interaction ratios. This procedure showed the presence of a noninteracting component of 6.0% for the pion beam. This quantity was assumed to be the muon fraction in the pion beam.

[18] S. Ecklund, M-1 User's Guide, Fermilab Report TM-743.2833, May (1977).

Absorption of a beam particle occurred when it interacted with material upstream of the target. This material amounted to 7.55×10^{-3} proton absorption lengths. All of the corrections discussed in this section are listed in Table 5. These corrections were common to all E-272 processes.

B. Target Dependent Corrections

Yields for the different interactions were corrected for absorption of charged particles and photons, and for triggering losses caused by delta rays produced in the target. These corrections were based on the number of charged particles and photons passing through the full length of the target. For K decays the Z vertex position of the decay determined the number and type of particles passing through the target. For interactions occurring in the target, corrections were applied assuming the beam particle traversed 1/2 of the target and were based on the particular final state.

The delta rays produced signals in the V1-V4 counters around the target. It was assumed the target MT veto rate for these counters represented the random veto rate. This was subtracted from the Pb and Cu veto rates to determine the delta ray contribution to the veto rate for those targets. The corrections were determined to be 0.98 ± 0.02

per charged particle for Pb and 0.93±0.02 per charged particle for Cu. One delta ray correction was applied for each charged particle passing through the target.

A correction was applied for the loss of photons in the target caused by conversion to electron-positron pairs. This was calculated using the approximate formula exp(-7t/9), where t is the thickness of the material in radiation lengths [19]. Again for interactions occurring in the target t was taken to be half of the target thickness. The absorption rate of the charged particles was also calculated. To account for the differences in the nuclear absorption cross sections for different types of incident particles, the data of A. S. Carroll et al. were used [20].

[19] Yung-Su Tsai, Rev. of Mod. Phys. 46, 815 (1974).

[20] A. S. Carroll et. al, Phys. Lett. 80B, 319 (1979).

C. Spectrometer Corrections

As with the target corrections, yields were corrected for absorption of charged particles and the conversion of photons in the material of the spectrometer. There were 2.87×10^{-2} proton absorption lengths and 0.087 radiation lengths of material in the spectrometer. Again, the conversion to pion absorption lengths was accomplished using the data of A. S. Carroll et al. [20]. Once a resonance had been produced corrections had to be made for its decay to the proper decay mode. These final state particles could inturn decay. Yields were corrected by using the decay rates listed by the Particle Data Group [21].

The Monte Carlo model was inadequate in the modeling of both the LAC and the track counters. The LAC problem manifested itself as an excess of real data photons when compared to a similar Monte Carlo generated sample. A "photon" here is a photon as defined by the LAC reconstruction program. This definition required correlated energy in the two views of the LAC and the photon must have had a reconstructed position more than 1.25 cm from any charged track (see Chapter IV.). This photon excess primarily stemmed from difficulties in reproducing hadronic shower development. Monte Carlo generated hadronic showers tended to fall within the 1.25 cm overlap region much more frequently than their real data counterparts.

[21] Particle Data Group, see reference 6.

K decays were used to study this process. For one charged particle final states $K^+ \to \pi^+ \pi^0$ events were used. The events chosen for this study were selected using all the cuts from Table 3 except cut e. Cut i, the π^0 mass cut, now referred to the 2-photon combination whose mass was closest to the nominal π^0 mass, 135 MeV and cut g, the total energy, was made up of the charged track energy and the energy of the 2-photon combination chosen as the π^0. A comparison was made between the photon distributions of the Monte Carlo and data kaons. This comparison showed that reconstructed data $K^+ \to \pi^+ \pi^0$ decays had at least three photons 2.2% more often than the Monte Carlo generated decays. In other words, 2.2% more real data events would fail a 2-photon cut as compared to Monte Carlo generated events.

$K^+ \to \pi^+ \pi^+ \pi^-$ decays were used to study this problem for three charged particle final states. Since there were no photons as part of this final state there were no restrictions on the reconstructed LAC information. After reconstruction it was found that 4% of the Monte Carlo $K^+ \to \pi^+ \pi^+ \pi^-$ decays had at least one extra photon while for the real data this number was 15%. For final states with three charged particles and two photons, like the B^+ meson, this implied a correction of 11%. The extra photon corrections are used for the $K^+ \to \pi^+ \pi^0$ and $B^+ \to \pi^+ \omega$ data and are listed in Tables 6 and 10.

The Monte Carlo was developed to model the performance of the track counters and the proportional chambers for well-behaved triggers. Events with ≥ 5 bunch counts in one of the track counters

had been deliberately ignored. This was done because the track counting logic of the data triggers was set up to veto any bunch count which was ≥5 (see Chapter II.). This was not a problem for one charged particle final states but an otherwise acceptable three charged particle event could have been vetoed with just two random noise hits in one of the proportional chambers. Erratic behavior by any of the proportional chambers would have clearly caused a veto.

The level at which this occurred was studied by using the two track counter test tapes. One test tape had the upstream track counters removed from the trigger logic while the other had the downstream track counters removed. Monte Carlo data was also generated in the same way to test its performance.

Because there were only these two tapes the events chosen for study were any reconstructed three track event whose combined energy fell between 192 - 212 GeV. These events were broken into three classes. First, there were events which would have satisfied the complete trigger. Next, there were events which would have violated some aspect of the complete trigger other than the ≥5 limit. The Monte Carlo model correctly predicted the level of these "illegal" triggers. The last class of events were those which had a ≥5 bunch count. This last class of events was not modeled in the Monte Carlo. Care was taken to insure that this noise was random and it was applied as a separate correction rather than incorporate it into the Monte Carlo model. This last class of events comprised a 15% correction and

was applied to all three charged particle final states.

D. Kaon Decays

$K^+ \to \pi^+ \pi^0$ and $K^+ \to \pi^+ \pi^+ \pi^-$ decays were used to check the normalization procedure. This was done by measuring the decay rate of beam kaons. The number of beam kaons which decay within a given region of the spectrometer can be calculated from the lifetime of the kaon. A particle with a lifetime τ, will decay in a region of length ΔZ, with a probability

$$\text{prob.} = \Delta Z/(c\gamma\tau).$$

In this expression, c is the speed of light and γ is the energy/mass of the decaying particle. For 200 GeV kaons the decay probability is 6.66×10^{-6}/cm. This probability must be modified by the decay fraction of the decay mode of interest.

To determine the decay rate from the data the beam count had to corrected and the acceptance of the spectrometer had to be determined. For $K^+ \to \pi^+ \pi^0$ the acceptance was determined in the region downstream of the target from 100 cm to 400 cm (see figure 21). This acceptance was calculated by generating Monte Carlo $K^+ \to \pi^+ \pi^0$ decays uniformly in the region of interest and comparing the number generated to the number of events which passed the cuts listed in Table 3. The spectrometer

acceptance plus all the correction factors for the beam count are listed in Table 6.

The decay rate for the $K^+ \to \pi^+\pi^+\pi^-$ decay mode was determined in the same way. Rather than select the relatively flat region between -50 cm and 10 cm a broad region from -250 cm to 250 cm was chosen (see figure 22). The qualitative differences between the real data and Monte Carlo vertex shapes required a large region to smooth out any local acceptance variations. The corrections for the beam count and the Monte Carlo acceptance are listed in Table 7.

The last row in both the Tables 6 and 7 list the ratios of the measured to calculated decay rates. These numbers differ from unity by 11 - 18 percent. One approach is to assume the discrepancy relates to some non-calculable error such as an overall veto or readout failure which affects all event types. There are also possible systematic errors in the Monte Carlo model. For $K^+ \to \pi^+\pi^0$ events the weak link involves the generation and reconstruction of 2-photon events. This problem has already been mentioned in the previous chapter and could account for the discrepancy. The pions from the $K^+ \to \pi^+\pi^+\pi^-$ events are all tightly bunched in the upstream beam region. This region was difficult to model (see Chapter V.) and it is easy to imagine small changes in the shape and sensitivity of the beam region having large effects on track reconstruction efficiency.

Table 5

Beam Related Corrections

	Beam Type	Pb	Cu	MT
1 Beam Track Random Vetos S Counter	π	0.748±0.016	0.791±0.014	0.770±0.011
	K	0.761±0.024	0.806±0.021	0.780±0.018
μ Contamination	π	0.94±0.015	0.94±0.015	0.94±0.015
	K	0.996	0.996	0.996
Particle Misidentification	π	0.995	0.995	0.995
	K	0.985	0.985	0.985
Absorption Upstream of Target	π	0.994	0.994	0.994
	K	0.995	0.995	0.995
Total Beam Correction	π	0.695±0.019	0.739±0.018	0.716±0.016
	K	0.743±0.024	0.787±0.021	0.761±0.018

Table 6

$K^+ \to \pi^+ \pi^0$ Decay Corrections

		Pb	Cu	MT
Incident Particle Corrections (see Table 5)		0.743±0.024	0.787±0.021	0.761±0.018
Target Related Corrections	δ-ray / Charged Particle	0.975±0.02	0.928±0.02	1.0
	Absorption in Target	0.997	0.984	1.0
Spectrometer Related Corrections	Absorption in Spectrometer	0.981	0.981	0.981
	γ Conversion / γ	0.935	0.935	0.935
	Extra Photon	0.978	0.978	0.978
Decay Corrections	$K^+ \to \pi^+ \pi^0$ Decay	0.2116	0.2116	0.2116
	$\pi^0 \to \gamma\gamma$ Decay	0.989	0.989	0.989
	No π^+ Decay	0.997	0.997	0.997
Total Correction Factor		0.135±0.005	0.134±0.005	0.142±0.004
Monte Carlo Acceptance		0.323±0.003	0.323±0.003	0.323±0.003
Raw Gated Kaon Beam $\times 10^8$		11.55	4.78	2.44
Corrected Beam $\times 10^8$		0.504±0.019	0.207±0.008	0.112±0.003
Observed Decay Prob. $\times 10^{-3}$ (300 cm)		1.75±0.066	1.76±0.068	1.78±0.048
Ratio of Decays Seen to Decays Expected		0.877±0.033	0.885±0.034	0.893±0.024

Table 7

$K^+ \to \pi^+\pi^+\pi^-$ Decay Corrections

		Pb	Cu	MT
Incident Particle Corrections (see Table 5)		0.743±0.024	0.787±0.021	0.761±0.018
Target Related Corrections	δ-ray / Charged Particle	0.975±0.02	0.928±0.02	1.0
	Absorption Targ. / Particle	0.9971	0.983	1.0
Spectrometer Related Corrections	Absorption Spec. / Particle	0.978	0.978	0.978
	>5 Track Count	0.845±0.014	0.845±0.014	0.845±0.014
Decay Corrections	$K^+ \to \pi^+\pi^+\pi^-$ Decay	0.0559	0.0559	0.0559
	No Charged π Decay / Part.	0.997	0.997	0.997
Total Correction Factor $\times 10^{-2}$		3.16±0.13	3.10±0.13	3.33±0.11
Monte Carlo Acceptance		0.217±0.007	0.194±0.007	0.233±0.007
Raw Gated Kaon Beam $\times 10^{8}$		11.55	4.78	2.44
Corrected Beam $\times 10^{7}$		7.92±0.41	2.87±0.16	1.89±0.10
Observed Decay Prob. $\times 10^{-3}$ (500 cm)		2.73±0.14	2.97±0.17	2.77±0.15
Ratio of Decays Seen to Decays Expected		0.823±0.043	0.894±0.05	0.835±0.045

VII. B^+ Data

The only established decay mode for the B^+ meson is $B^+ \to \pi^+\omega$ [22]. This experiment detected this reaction in the coherently produced final state $\pi^+\pi^+\pi^-\pi^0$. This chapter presents data for the reaction

$$\begin{aligned} &\pi^+ + A \to A + B^+ \\ &\qquad\qquad\quad \hookrightarrow \pi^+\omega \\ &\qquad\qquad\qquad\quad \hookrightarrow \pi^+\pi^-\pi^0 \\ &\qquad\qquad\qquad\qquad\quad \hookrightarrow \gamma\gamma \end{aligned} \tag{16}$$

and presents results for the fits of the mass and t distributions. Table 8 lists the cuts used to define an event from the above interaction.

[22] Particle Data Group, see reference 6.

Table 8

Cuts Used to Define $B^+ \to \pi^+ \omega$, $\omega \to \pi^+\pi^-\pi^0$, $\pi^0 \to \gamma\gamma$

a) A1 Trigger
b) Pion Trigger
c) 1 Beam Track
d) 3 Tracks in Final State
e) 2 Photons in Final State
f) Decay Vertex at Target -43 - 33 cm
g) Reconstructed π^0 Mass 0.110 - 0.160 GeV
h) Total Energy 192 - 212 GeV
i) Reconstructed ω Mass
   Either Combination 0.720 - 0.840 GeV
j) Veto Reconstructed η Mass
   Either Combination 0.510 - 0.590 GeV
k) Reconstructed $t<0.003$ Pb; $t<0.005$ Cu

Comparisons of the data with Monte Carlo generated distributions are presented in the rest of this section. This is done to verify the reliability of the Monte Carlo's acceptance prediction. Each of the decays in the sequence was generated in its respective center of mass frame. First, the $B^+ \rightarrow \pi^+ \omega$ decay was generated. This decay is dominantly S wave and was generated isotropically [22]. The momenta of the ω decay pions were assigned using the Dalitz plot of a 1^- particle [23]. The direction of each of these pions was determined by randomly assigning the vectors of the normal to the ω decay plane and the π^0 momentum. Momentum conservation determined the vectors of the remaining two pions. The photons from the π^0 decay, a spin 0^- object, were assigned equal energies and a random direction in the π^0 rest frame. The final state particles were then all boosted into the laboratory frame and the Monte Carlo generated the event as described in Chapter V.

Figure 34 shows the four pion mass distribution from the combined data of the Pb and Cu targets. The events shown in this figure were selected using the cuts a through h from Table 8. There is a clear enhancement at ~1.270 GeV. It should be pointed out that $A2^+ \rightarrow \pi^+ \eta$ is also present in this sample.

Figure 35 shows the three pion mass for these data. For each event there were two possible $\pi^+\pi^-\pi^0$ combinations. Both combinations are present in this figure. There is a clear ω peak at 0.783 GeV and

[23] M. L. Stevenson et al., Phys. Rev. 125, 687 (1962).

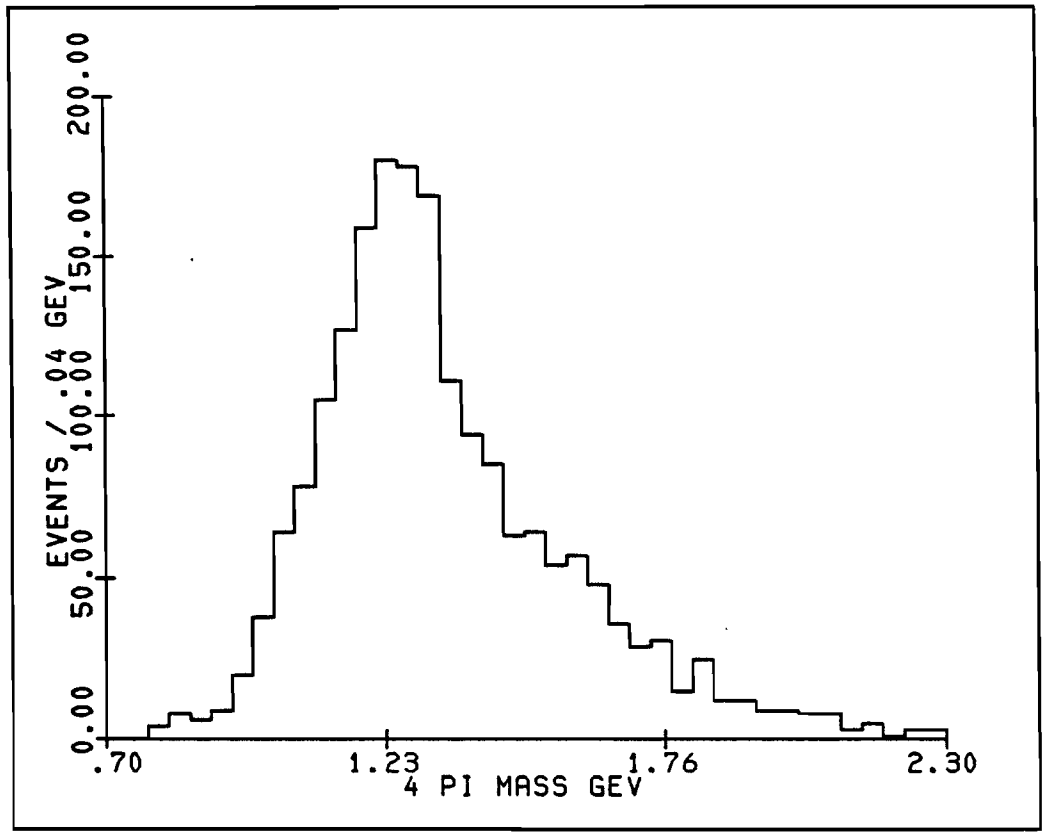
EVENTS / .04 GEV
0.00
50.00
100.00
150.00
200.00
.70
1.23
1.76
2.30
4 PI MASS GEV

Figure 34

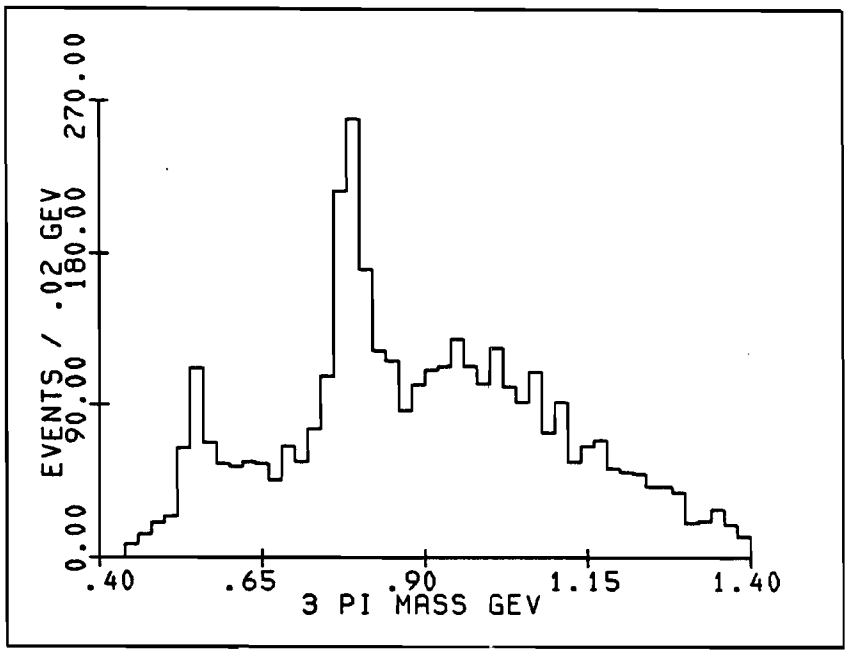

Figure 35

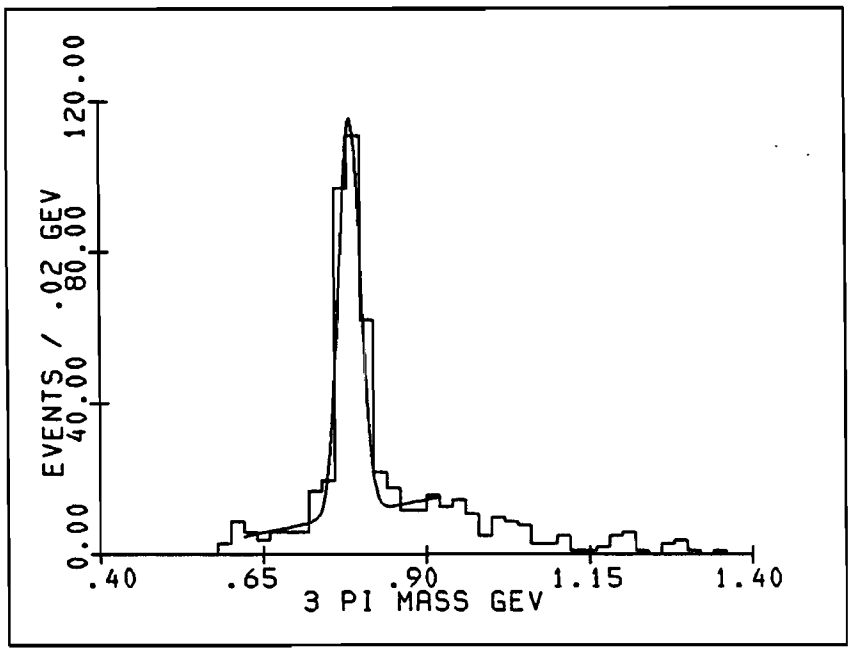

Figure 36

a smaller η peak at 0.549 GeV. These η's are from A2 decays. In all subsequent figures these events have been removed by deleting all events with a sub mass between 0.510 and 0.590 GeV (cut i, Table 8).

Figure 36 shows the three pion mass distribuition with only one combination from each event. For this figure the combination whose effective mass was closer to the accepted mass, 0.783 GeV, was chosen.

The cuts used to select the events in figure 36 were a through i and k (see Table 8) plus an additional restriction. This restriction only accepted events which had a Dalitz radius squared less than 0.5 (see figure 37). This should enhance the ω signal because the 1^- Dalitz plot is bell shaped while any background would be expected to have a different shape. In particular nonresonant three pion events would have a flat Dalitz plot. The background under the ω peak in figure 36 is ~10%. This background was not present in the Monte Carlo generated events. The solid line in figure 36 shows the Monte Carlo prediction for $\pi^+\omega$ events added to a linear background. The distribution has a σ of 16.5 MeV. This figure was used to define the ω region to be from 0.720 GeV to 0.840 GeV.

Figure 37a shows the Dalitz scatter plot for the data events. The variables are defined as $X=(T2-T1)/\sqrt{3}$ and $Y=T3-1$ but the 1^- Dalitz plot has sextant symmetry. In this figure the roughly circular Dalitz plot has been folded six times along it's lines of symmetry. The T's have been divided by Q/3 so that the variables X and Y have a range from -1 to 1. The quantity Q is determined on an event by event

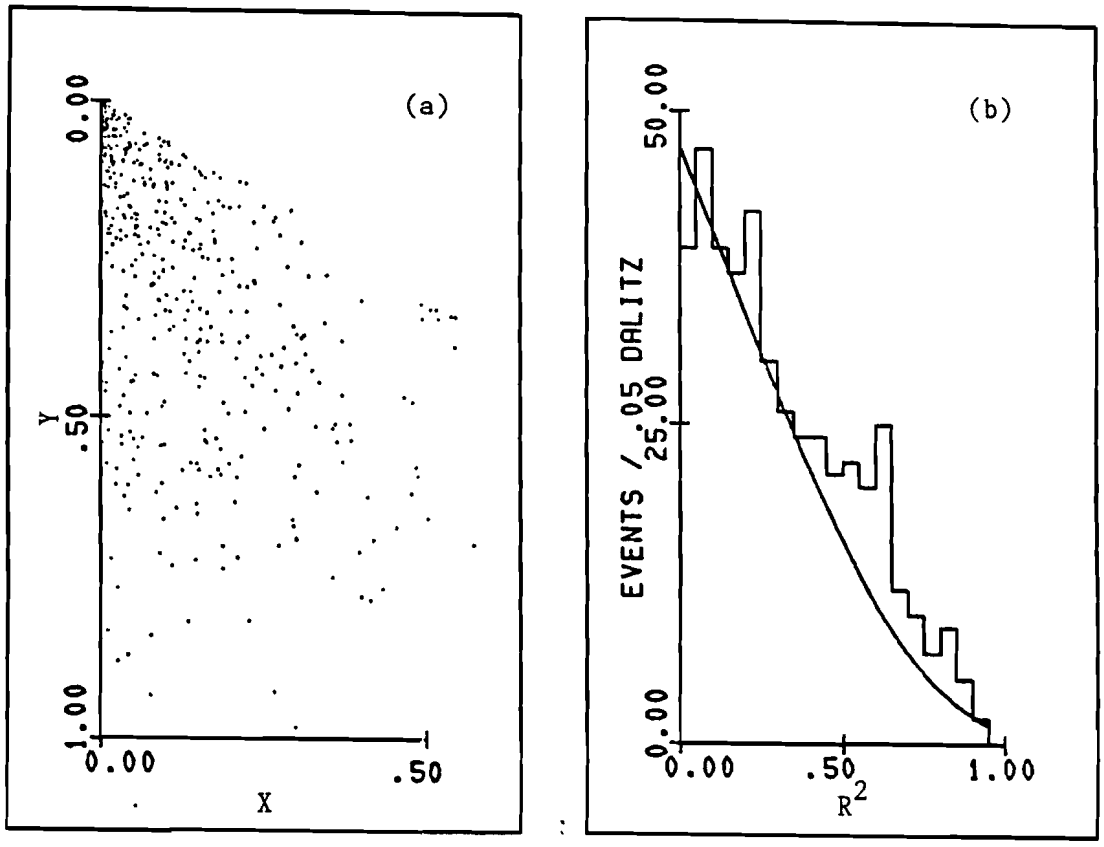
(a)
0.00
.50
1.00
Y
0.00
.50
X
(b)
50.00
25.00
0.00
EVENTS / .05 DALITZ
0.00
.50
1.00
R^2

Figure 37

basis. T3 is the π^0 variable while T1 and T2 are the variables for the π^+ and π^-. The scatter plot shows the characteristic change in the density expected for the decay of a 1^- particle [23].

Figure 37b shows the radial distribution for the events shown in figure 37a. The variable on the abscissa is $R^2=X^2+Y^2$ and the characteristic 1^- shape is evident. The solid line is the Monte Carlo prediction and has a somewhat steeper slope. Some differences are expected because of the background present in the real data sample. In addition discrepancies could be caused by slight differences between the Monte Carlo and data momentum resolution. Possible causes of the discrepancy are π^0 energy resolution and proper resolution smearing in the beam region. These problems have already been discussed in Chapter V.

Figure 38 shows the 2-photon mass distribution for events selected by restrictions a through f and h through k (see Table 8). The discrepency between the Monte Carlo and data π^0 widths, which was discussed in Chapter V., is also apparent in this figure. Here the π^0 mass widths are 8.5 MeV for the data and 5.5 MeV for the Monte Carlo generation. These values are somewhat wider than their counterparts from the $K^+\to\pi^+\pi^0$ analysis. This reflects the increase of energy deposited in the LAC by the presence of two additional charged particles in the final state. This increased the likelihood of electromagnetic showers overlapping in the two views of the LAC. The resulting confusion in separating the showers led to this increase in

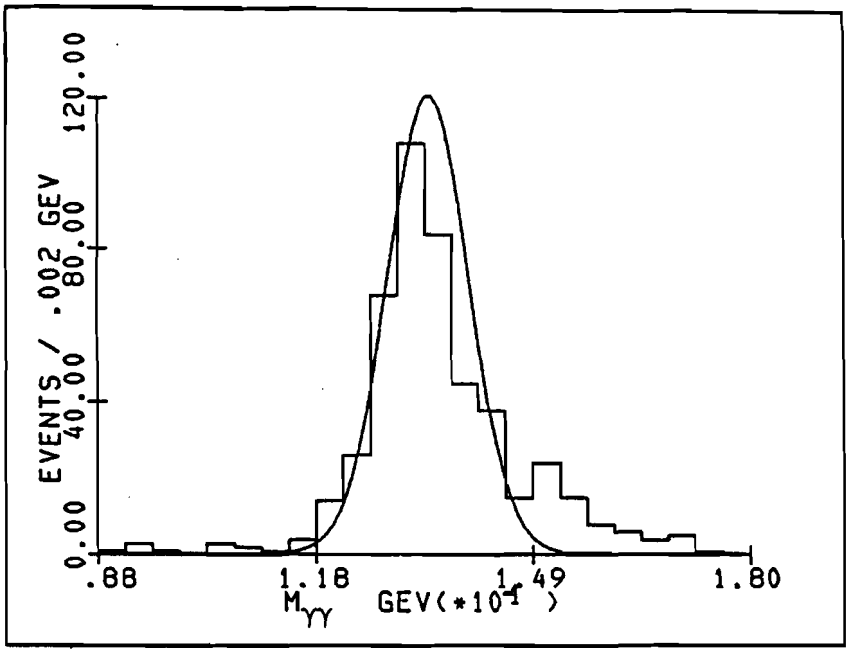

Figure 38

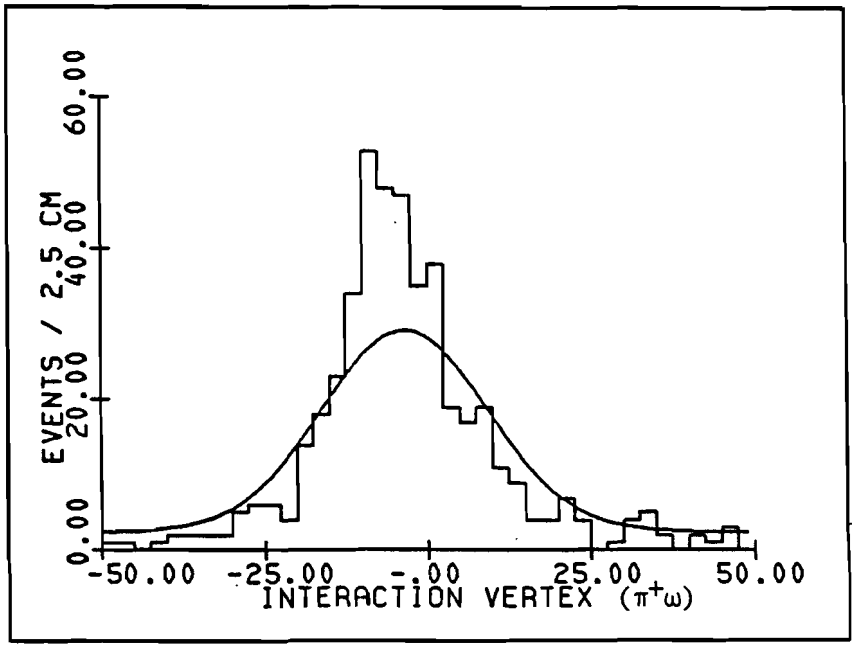

Figure 39

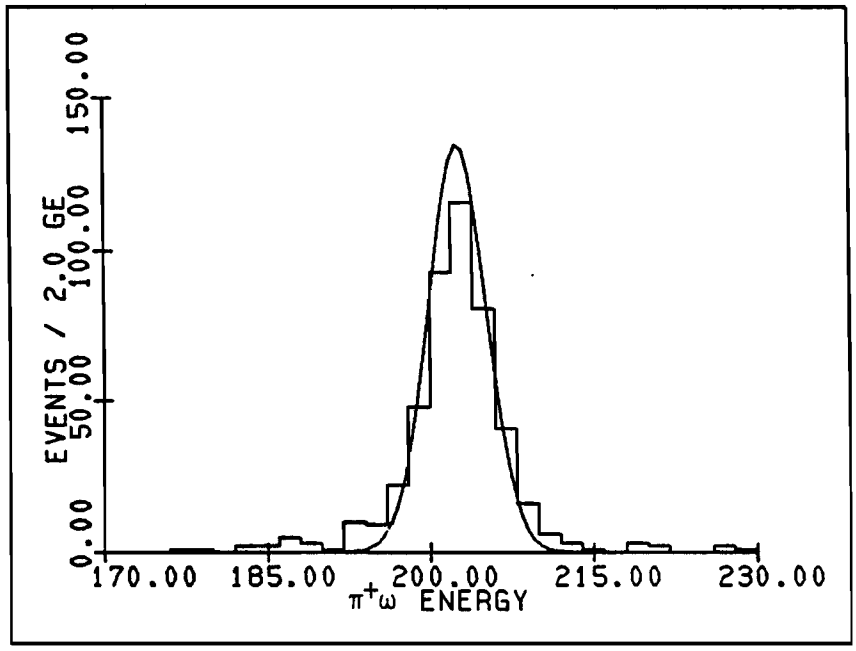
EVENTS / 2.0 GE
0.00
50.00
100.00
150.00
170.00
185.00
200.00
215.00
230.00
π+ω ENERGY

Figure 40

the measured widths of the π^0 mass distribution.

Figure 39 shows the vertex distributions for the events selected by the cuts a through e and g through k (see Table 8). The agreement between the Monte Carlo prediction and the data is not good. The cause of the this discrepency is again resolution. To minimize the effects of this problem a wide vertex cut of -43 cm to 33 cm was used to define the target region.

Figure 40 shows the total energy distribution for these events. The σ of this distribution is 2.7 MeV. Here the Monte Carlo prediction and the data agree quite well. The lack of any low energy events indicates the absence of any inelastic background.

Figure 41 and 42 show the Pb and Cu four pion effective mass plots for the event sample selected by using all the cuts from Table 8. Figure 43 shows these events in a combined plot. Note the peak is still centered around 1.270 GeV.

Figure 44 shows the Monte Carlo predicted mass acceptance for $\pi^+\omega$ events. This curve is not flat over the mass region of interest. It is flat for only a short period after threshold at 0.92 GeV and proceeds to drop sharply at higher masses. This drop is the result of final state particles spreading out and vetoing in the counters around the magnet. The roll off near threshold, resulting in the flat region, is caused by the beam region inefficiency. Any events generated near this mass region would have some of its final state

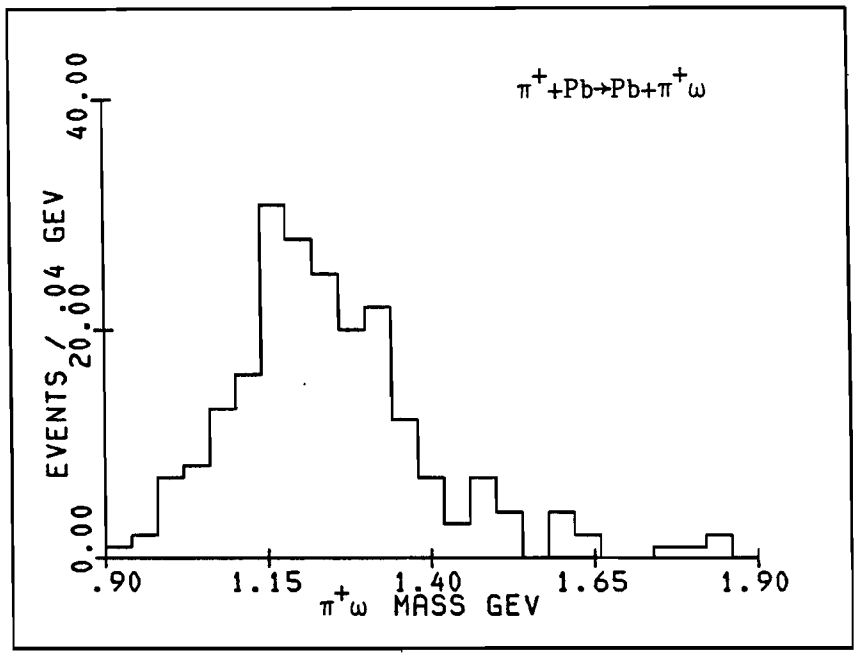

Figure 41

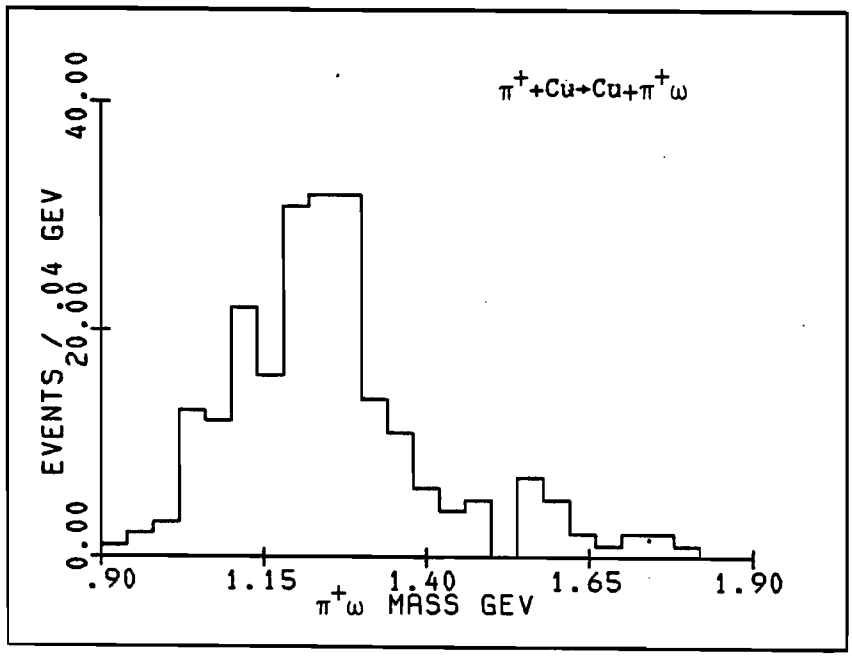

Figure 42

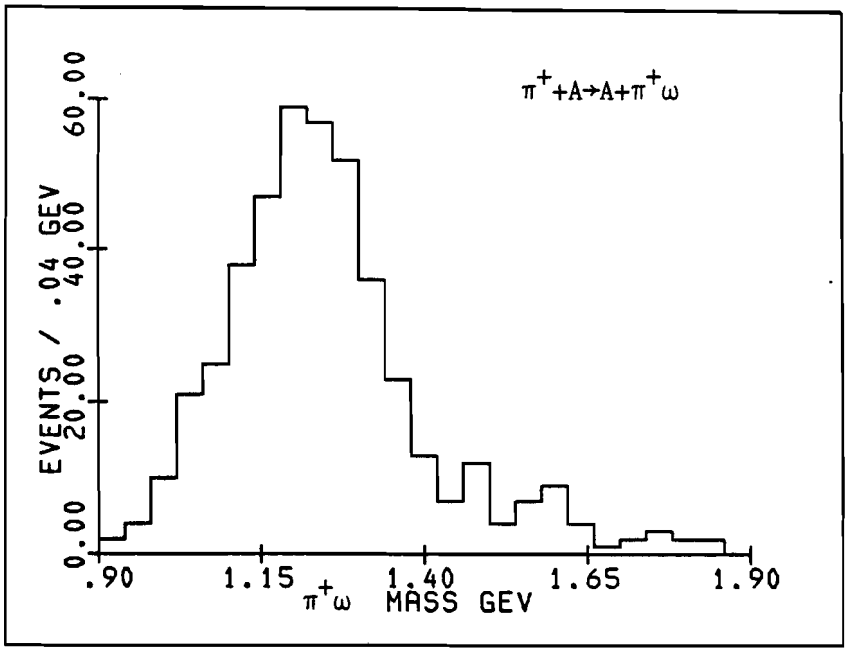

Figure 43

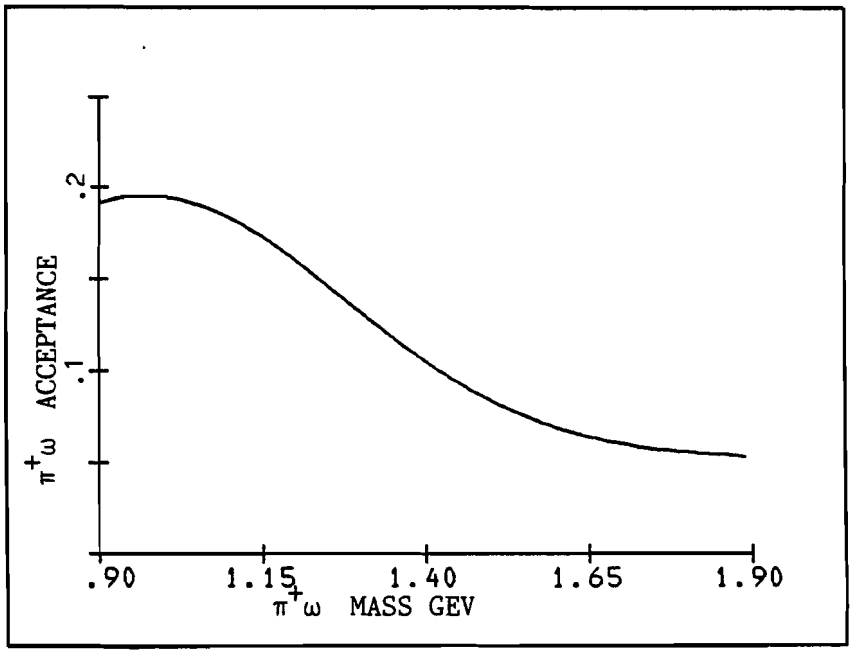

Figure 44

particles moving forward through the beam region of the upstream chambers.

A. Mass Fits

The mass spectrum of Coulomb production can be described using equation (11) from Chapter I. This is done by integrating the expression over the variable t and obtaining the equation

$$\frac{d\sigma}{dm^2} = 12\pi\,\alpha\; Z^2 \frac{m^2}{(m^2-m_\pi^2)^3}\; \Gamma_\gamma\left[\frac{1}{\pi}\frac{\Gamma_{\pi\omega}/2}{(m-m_B)^2 + (\Gamma_{tot}/2)^2}\right] \int_{t_{min}}^{t_{max}} \frac{t-t_{min}}{t^2}\,|F(t)|^2\,dt\,. \tag{17}$$

To make this expression more useful the expression in brackets is replaced by the relativitic form of the Breit-Wigner, Γ_{tot} is set equal to $\Gamma_{\pi\omega}$, and the cross section is converted to one with respect to the invariant mass. This yields

$$\frac{d\sigma}{dm} = 48\pi \propto Z^2 \frac{m^3}{(m^2-m_\pi^2)^3} \Gamma_\gamma \left[\frac{1}{\pi} \frac{m_B^2 \Gamma_{\pi\omega}}{(m-m_B)^2 + (m_B\Gamma_{\pi\omega})^2}\right]$$

$$* \int_{t_{min}}^{t_{max}} \frac{t-t_{min}}{t^2} |F(t)|^2 \, dt \quad . \tag{18}$$

The integral over t can be evaluated by setting $|F(t)|^2 = e^{-bt}$ and allowing t_{max} to go to infinity. In the expression for the form factor $b=(1.12*A^{1/3})^2/3$ [24]. This yields

$$f(m) \equiv \int_{t_{min}}^{\infty} \frac{t-t_{min}}{t^2} e^{-bt} \, dt \simeq -1.577 - \ln (b \, t_{min}) \tag{19}$$

where the mass dependence is contained in t_{min} (see Chapter I.).

The B^+ meson is a broad resonance and so the mass dependence of the two widths $\Gamma_{\pi\gamma}$ and $\Gamma_{\pi\omega}$ must be taken into account. If the decay of a resonance proceeds through a partial wave of orbital angular momentum l the mass dependence of the width can be written as [25]

[24] For a discussion of the electromagnetic form factor see "High Energy Hadron Physics" by Martin Perl, John Wiley and Sons Inc., p. 449.

[25] J. D. Jackson, Nuovo Cimento 34, 1644 (1964).

$$\Gamma(q) = \Gamma_o \left(\frac{q}{q_o}\right)^{2l+1} \tag{20}$$

Here, q is the three momentum of the decay particles in the resonance rest frame and q_0 is the value of the momentum at the resonance mass. It has been established that the B^+ decay is primarily S wave and so an additional factor of q/q_0 appears with each $\Gamma_{\pi\gamma}$ and $\Gamma_{\pi\omega}$.

The equation used for the mass fits is

$$\frac{d\sigma}{dm} = C \left(\frac{m}{(m^2-m_\pi^2)}\right)^3 \left(\frac{k}{k_o}\right) \left[\frac{m_B^2\, \Gamma_{\pi\omega} \left(\frac{p}{p_o}\right)}{(m^2-m_B^2)^2 + (m_B \Gamma_{\pi\omega})^2 \left(\frac{p}{p_o}\right)^2}\right]$$

$$* \quad f(m) \quad . \tag{21}$$

Here, p and k refer to the center of mass momentum of the respective $\pi^+\gamma$ and $\pi^+\omega$ decays, m_B to the resonant mass of the B^+ meson, and C is a normalization constant. The three parameters in the fit were the width $\Gamma_{\pi\omega}$, the resonance mass m_B, and the normalization constant C.

In each of the next three figures (45, 46, and 47), there are two plots showing fits to the $\pi^+\omega$ mass spectra for the Pb, Cu, and combined target data. The data in these plots are from figure 41, 42, and 43 respectively and have been corrected for acceptance by using the Monte Carlo. The errors used are statistical only. The top or

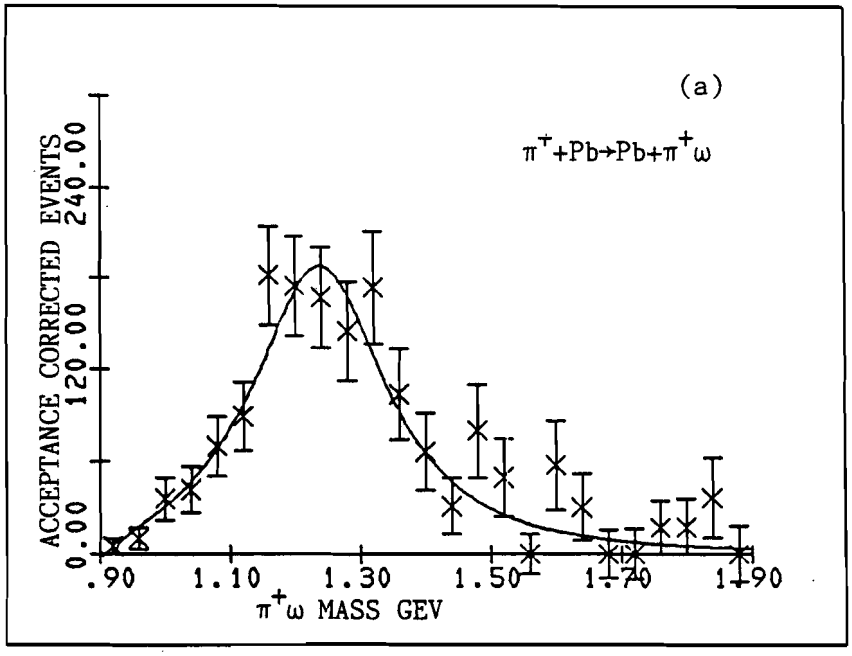
(a)
π⁺+Pb→Pb+π⁺ω
ACCEPTANCE CORRECTED EVENTS
0.00
120.00
240.00
.90
1.10
1.30
1.50
1.70
1.90
π⁺ω MASS GEV

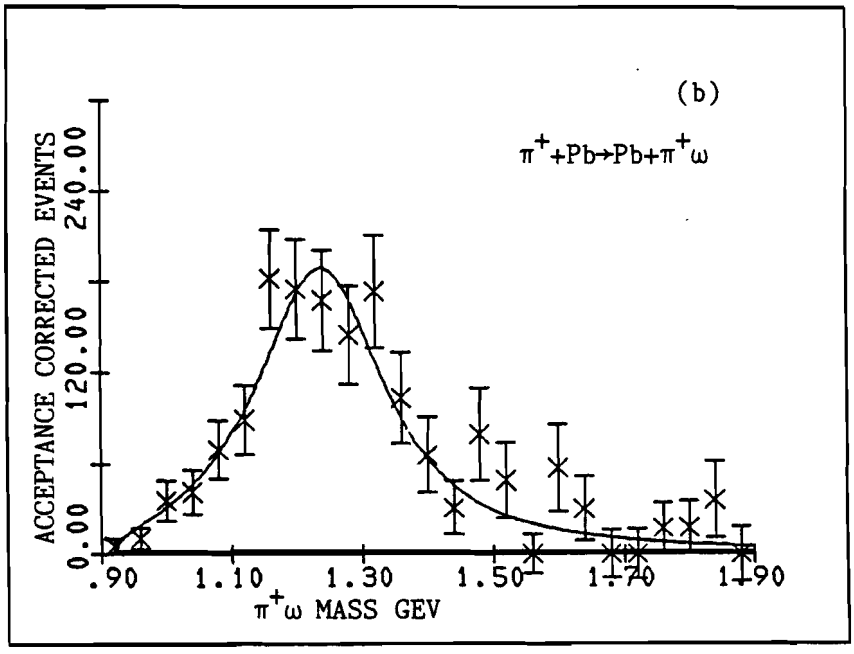
(b)
π⁺+Pb→Pb+π⁺ω
ACCEPTANCE CORRECTED EVENTS
0.00
120.00
240.00
.90
1.10
1.30
1.50
1.70
1.90
π⁺ω MASS GEV

Figure 45

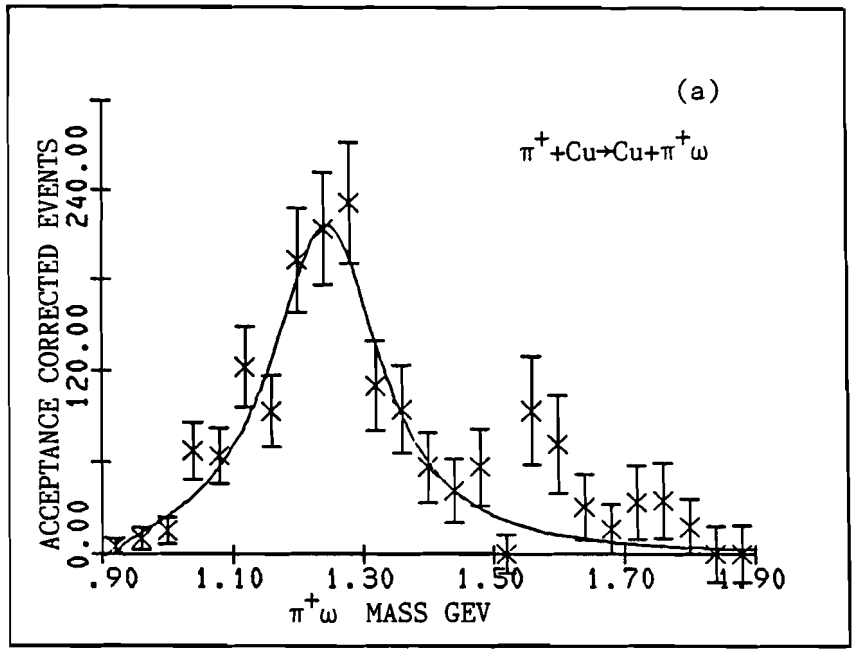
(a)
π+Cu→Cu+π+ω
ACCEPTANCE CORRECTED EVENTS
0.00
120.00
240.00
.90
1.10
1.30
1.50
1.70
1.90
π+ω MASS GEV

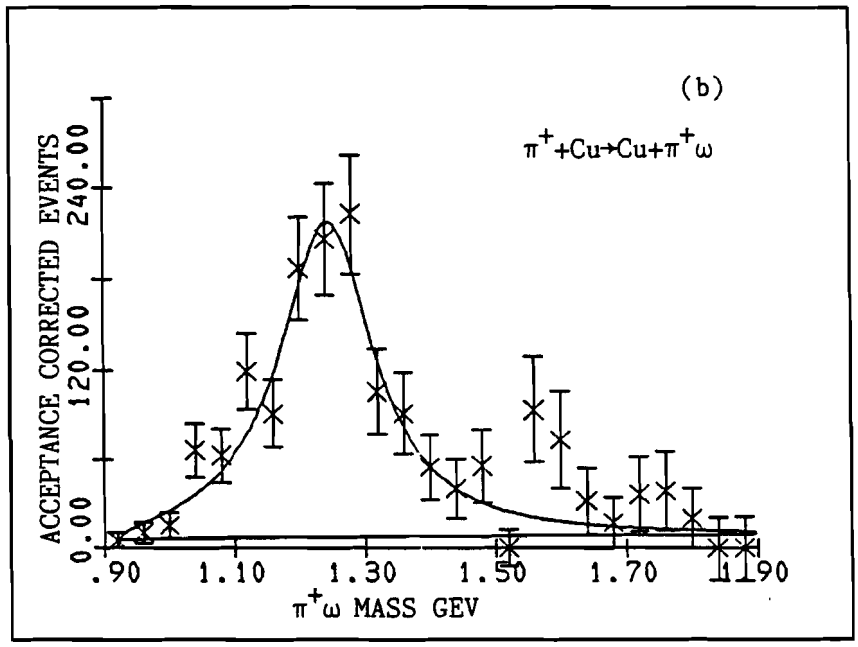
(b)
π+Cu→Cu+π+ω
ACCEPTANCE CORRECTED EVENTS
0.00
120.00
240.00
.90
1.10
1.30
1.50
1.70
1.90
π+ω MASS GEV

Figure 46

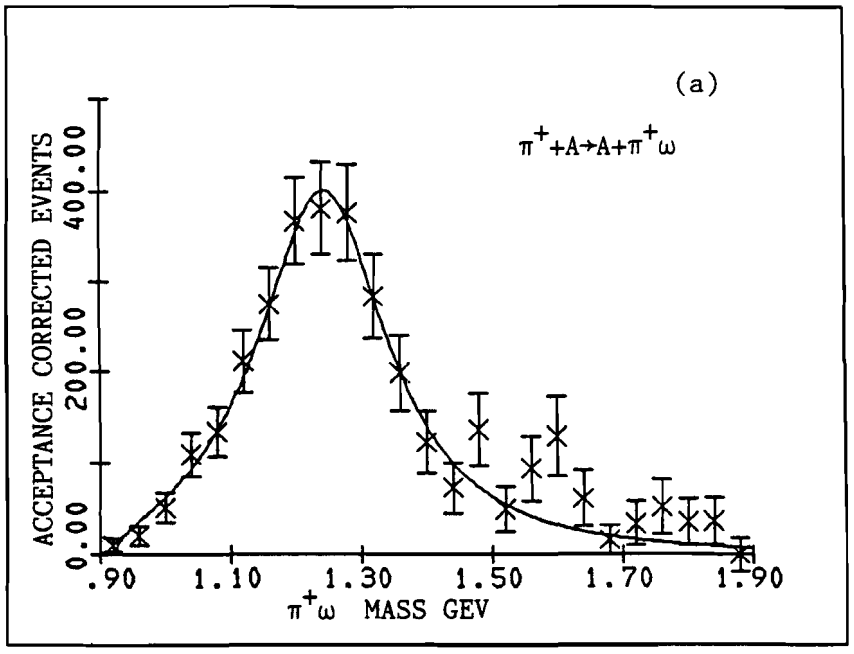
(a)
$\pi^+ + A \to A + \pi^+ \omega$
ACCEPTANCE CORRECTED EVENTS
0.00
200.00
400.00
.90
1.10
1.30
1.50
1.70
1.90
$\pi^+\omega$ MASS GEV

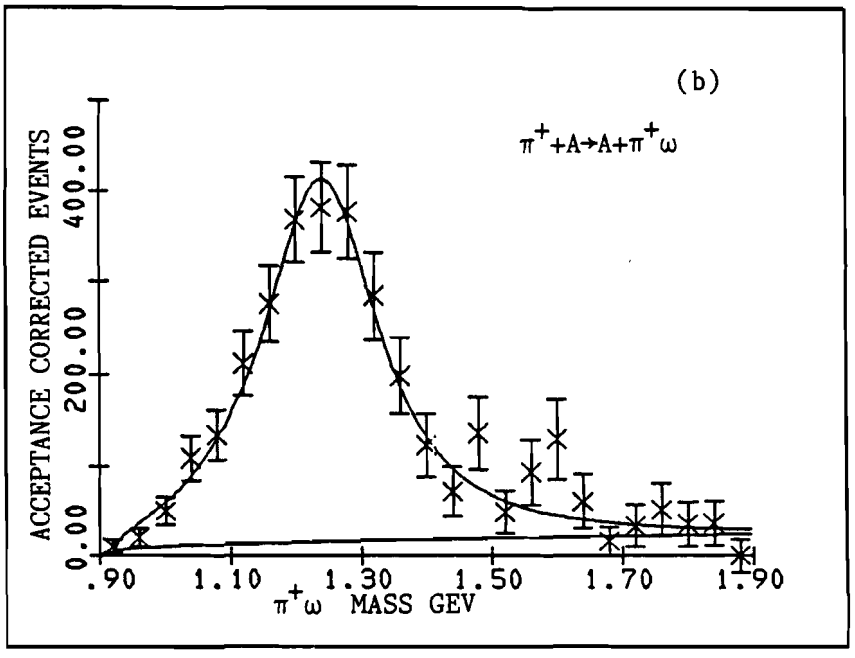
(b)
$\pi^+ + A \to A + \pi^+ \omega$
ACCEPTANCE CORRECTED EVENTS
0.00
200.00
400.00
.90
1.10
1.30
1.50
1.70
1.90
$\pi^+\omega$ MASS GEV

Figure 47

Table 9

Results of Mass Fits

Coulomb Only

Target	Resonance Mass (Gev)	Width (GeV)	χ^2/DOF
Cu	1.272±0.011	0.217±0.032	28.0/22
Pb	1.280±0.017	0.276±0.039	17.6/22
Combined	1.283±0.011	0.268±0.028	21.5/22

Coulomb plus Background

Target	Resonance Mass (GeV)	Width (Gev)	χ^2/DOF
Cu	1.265±0.011	0.188±0.033	25.6/19
Pb	1.277±0.017	0.265±0.041	17.4/19
Combined	1.271±0.011	0.232±0.029	17.1/19

(a) plot on each page shows the fits using the Coulomb cross section from equation (21). The lower or (b) plot shows the same data fit with the addition of a constantly rising background term added to the Coulomb cross section. The form of the background was a second order polynomial.

Table 9 summarizes the results of these fits. Because there was background underneath the ω peak (see figures 35 and 36) it was expected that a background term would improve the fits. In addition, since the background chosen increased with mass it was also expected that the fit values for the resonance's mass and width would shift toward lower values. The trend toward lower values is seen in the fitted results, although in all cases the shifts are within the errors of the values from the Coulomb only fits. For the Pb target data the background made up less that 4% of the total peak and the resulting changes are small. For the Cu and combined fits the background term accounted for 13% of the resonance and the resulting shifts in the fitted values are more significant.

Because of the lower statistics of the separate targets and the presence of the background under the ω peak we believe that the most reliable of the fits was the combined fit listed last on Table 9. Moreover, the errors associated with these fitted values encompassed all the other fits.

Though the results for the mass and width listed in Table 9 are consistent with one another the results of m_B=1.271±0.011 GeV and $\Gamma_{\pi\omega}$=0.232±0.029 GeV differ dramatically from the established values of 1.232 GeV and 0.137 GeV [22]. Systematic effects were examined to test the stability of these results. Different sets of data were selected by varying the t range and the Dalitz variable R^2. The changes of the fitted values were of the order of 5% for the mass and the width, well within the statistical errors.

As further verification of the identity of the resonance an analysis of the sequential decays $B^+\to\pi^+\omega$, $\omega\to\pi^+\pi^-\pi^0$ was performed. Appendix A describes this analysis in more detail. The analysis was limited to an evaluation of the ω helicity amplitudes because at the small t values measured by this experiment the φ dependence was dominated by the resolution of the spectrometer. To avoid the acceptance problems mentioned at the end of the first section the helicity amplitudes were evaluated using the data from the mass region 1.0 - 1.4 GeV. $|F_0|^2$, the helicity-zero decay probability, was determined separately by two different methods and the results were 0.161±0.031 and 0.137±0.034. Using these values we quote a value of $|F_0|^2$=0.15±0.035. This value is somewhat higher but consistent with the values quoted by previous experiments [26]. An average value from these experiments is 0.11±0.06.

[26] V. Chaloupka et al., Phys. Lett. 51B, 407 (1974); U. Karshon et al., Phys. Rev. D 10, 3608 (1974); S.U. Chung et al., Phys. Rev. D 11, 2426 (1975); R. Gassaroli et al., Nucl. Phys. B126, 382 (1977).

The amplitude $F_0{}^2$, as measured by this experiment deviates significantly from zero. The helicity amplitude F_0 is allowed to be different from zero only for the unnatural spin-parity series 1^+, 2^-, 3^+,... [27]. Although this analysis is too limited to further determine the spin-parity assignment of the $\pi^+\omega$ data, it is clearly reasonable to assume that this resonance is a B^+ meson.

B. Cross Section

The cross section per event can be written as

$$\sigma(\text{per event})=(A/N_0\rho t)/(\text{C.F.} * \text{Beam Flux}) * \text{Target MT Correction} * 1/\text{Monte Carlo Acceptance} \quad (22)$$

where A is the atomic number of the target nucleus, N_0 is Avagadro's number, and ρt is the thickness of the target in gm/cm^2. The quantity $A/N_0\rho t$ is listed for the two targets on Table 11.

The incident flux was determined using the Cerenkov counters and the beam definition described in Chapter II. C.F. is the beam correction factor for the reaction in equation (16). After all of the

[27] S.U. Chung, Phys. Rev. 138, B 1541 (1965).

secondary decays the final state of the B^+ meson contains three charged pions and two photons from a π^0 decay. Because this final state contains a mixture of charged particles and photons the C.F. for the B^+ decay contains corrections from both $K^+ \rightarrow \pi^+\pi^0$ and $K^+ \rightarrow \pi^+\pi^+\pi^-$ decays (see Chapter VI.). Table 10 individually lists the elements which make up the B^+ meson's beam correction factor. All of the corrections listed on this table except the last group were discussed in the last chapter.

The last correction group on Table 10 is called the K decay Correction. In the last chapter it was pointed out that the normalization procedure did not give the correct K decay rates. It also briefly discussed problems which could account for the missing decays. These missing decays represent our ability to make an absolute measurement. This raises the question of what fraction of an arbitrary process are unaccounted for by the normalization procedure. If the final state of the process is identical to one of these two prominent K decays, an obvious solution would be to assume an identical fraction of missing events. This is not the case with the B^+ meson which has three charged pions and a π^0 in its final state. Obviously it is inappropriate to directly apply both decays to the B^+ meson normalization. Instead, it was decided to correct the beam count using 1/2 of the missing decays from each decay mode and to use errors which accounted for the remaining 1/2.

Table 10

B^+ Meson Decay Corrections

$B^+ \to \pi^+ \omega$
$\quad \hookrightarrow \pi^+ \pi^- \pi^0$
$\quad\quad \hookrightarrow \gamma\gamma$

		Pb	Cu	MT
Incident Particle Correction (see Table 5)		0.695±0.019	0.739±0.018	0.716±0.016
Target Related Corrections	δ-ray / Charged particle	0.975±0.02	0.928±0.02	1.0
	Absorption Targ. / Particle	0.992	0.983	1.0
	γ Conversion / γ	0.919	0.843	1.0
Spectrometer Related Corrections	Absorption Spec. / Particle	0.978	0.978	0.978
	γ Conversion / γ	0.935	0.935	0.935
	>5 Track Count	0.845±0.014	0.845±0.014	0.845±0.014
	Extra Photon	0.894±0.027	0.894±0.027	0.894±0.027
Decay Corrections	$\omega \to \pi^+\pi^-\pi^0$	0.898	0.898	0.898
	$\pi^0 \to \gamma\gamma$	0.989	0.989	0.989
	No Charged π Decay / Part.	0.997	0.997	0.997
K Decay Corrections	$K^+ \to \pi^+\pi^0$	0.939±0.062	0.943±0.058	0.945±0.054
	$K^+ \to \pi^+\pi^+\pi^-$	0.912±0.088	0.947±0.053	0.917±0.083
Total Correction Factor (C.F.)		0.252±0.037	0.203±0.030	0.358±0.051
Raw Gated Pion Beam $\times 10^9$		3.853	1.492	0.787
Corrected Pion Beam $\times 10^8$		9.71±1.43	3.03±0.45	2.82±0.40

Table 11

Factors for Determining μb / Event

	Pb	Cu
$A / N_0 \rho t$ (barns)	249.7±0.4	18.62±0.02
Corrected Pion Beam $x10^9$	9.71±1.43	3.03±0.45
MT Background	0.910±0.035	0.971±0.011
Monte Carlo Acceptance	0.159±0.004	0.162±0.004
$\sigma(\mu b$ / Event)	1.47±0.23	0.368±0.056

Table 11 lists the numbers used to evaluate equation (22). The first two items have already been discussed. The target MT correction was determined by analyzing the 7.87×10^8 beam pions taken with the targets removed. These data were collected on nine tapes taken at random intervals during the run and were analyzed in identical fashion to the Pb and Cu data. Only seven MT target events passed the cuts defining a B^+ meson. This yield was adjusted for each target to account for the differing amount of incident beam (see Table 10). It was then assumed that the target out background had the same shape as the data taken with the target in and the cross sections were reduced accordingly. The geometric and reconstruction acceptance of the B^+ meson were determined from the Monte Carlo model. The values for the cross section per event are given on the last line of Table 11.

C. Fits to t Distributions

The t distributions for B^+ meson production are shown in figure 48. The data in this plot were selected using all cuts from Table 8 except cut k. These data were converted to cross sections using the cross section per event from the Table 11. The error bars are statistical only. To avoid the acceptance problems mentioned at the end of the first section an additional mass cut of 1.0 - 1.4 GeV was implemented. The fitting formalism used on this data was developed

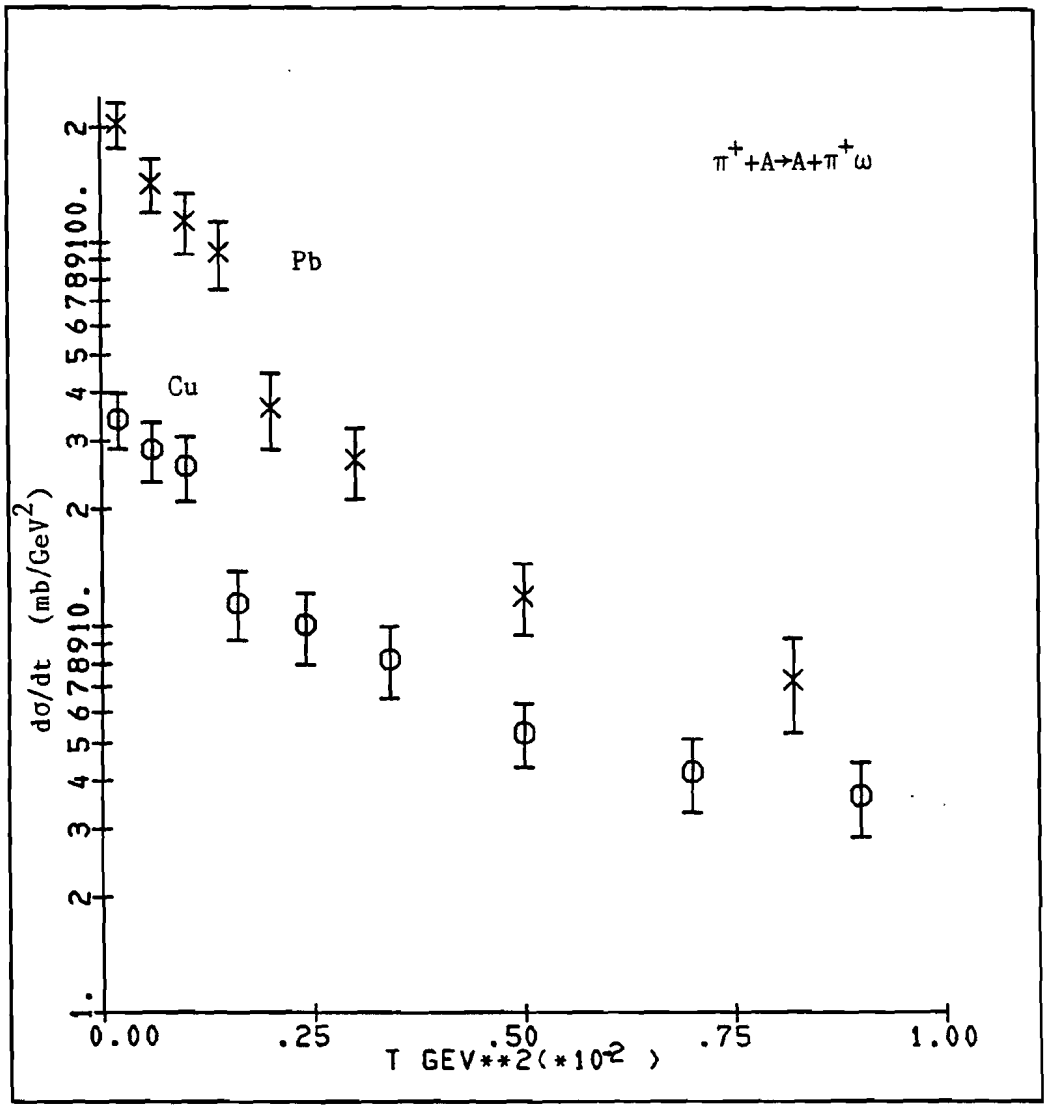
π⁺+A→A+π⁺ω
Pb
Cu
dσ/dt (mb/GeV²)
1.
2
3
4
5
6
7
8
9
10.
100.
0.00
.25
.50
.75
1.00
T GEV**2(*10⁻²)

Figure 48

previously and has been applied to several other experiments [28]. An extensive discussion of the how the fitting process is applied to this particular experiment appears in T. Jensen et al., reference 30. Only a brief outline is given here.

To start we rewrite equation (15) by making the substitutions $T_c=[\Gamma_\gamma(X\to Y\gamma)]^{1/2}f_c(q)$ and $T_s= C_s^{1/2}f_s(q)$. This emphasizes the relevant parameters and yields the expression

$$\frac{d\sigma}{dt} = \Gamma_\gamma|f_c(q)|^2 + C_s|f_s(q)|^2 + 2[\Gamma_\gamma C_s]^{1/2}$$

$$* \ [(\mathrm{Re}(f_c(q))\ \mathrm{Re}(f_s(q)) + \mathrm{Im}(f_c(q))\ \mathrm{Im}(f_s(q)))\cos\phi$$

$$+ \ (\mathrm{Im}(f_c(q))\ \mathrm{Re}(f_s(q)) - \mathrm{Re}(f_c(q))\ \mathrm{Im}(f_s(q)))\sin\phi] \ . \qquad (23)$$

Following the formalizm given in reference 28 the amplitude $f_c(q)$ is

$$f_c(q) = \frac{Z}{q^2}\ [24\pi\alpha\ \frac{m_B^3}{(m_B^2-m_\pi^2)^3}]^{1/2}\ \sqrt{2}\ (\vec{\varepsilon}\times\vec{k})\ \vec{f}_{em}(\vec{q})$$

where $\vec{q}=\vec{k}-\vec{p}$, $\vec{k}$ is the momentum of the incoming meson, $\vec{p}$ is the momentum of the outgoing meson, $\hat{\varepsilon}$ is the polarization of the outgoing meson, and $f_{em}(q)$ is the electromagnetic form factor. The

[28] K. J. Kolbig and B. Margolis, Nucl. Phys. B6, 85 (1968); G. Faldt et al., Nucl. Phys. B41, 125 (1972); G. Faldt, Nucl. Phys. B43, 591 (1972); C. Bemporad et al., Nucl. Phys. B51, 1 (1973).

electromagnetic form factor of the nucleus may be written in terms of the electric field, E(r), of the nucleus as follows:

$$\vec{f}_{em}(\vec{q}) = \frac{iq^2}{4\pi p} \int d^3r \; \Psi^{-*} \; e^{i\vec{q}\cdot\vec{r}} \; \vec{E}(r) \; \Psi^{+}$$

Ψ^- and Ψ^+ are the incoming and outgoing wave functions. These functions are Coulomb-distorted plane waves, modified to account for absorption and scatter inside the nucleus. In the manner employed by Bemporad et al. [28], this Coulomb form factor is calculated for different regions around the nucleus.

Because coulomb production occurs predominately outside the nucleus, the actual form of the charge distribution will not seriously affect the calculation of $f_{em}(q)$. For these calculations a uniform nucleus of radius $R=[c^2+(7/3)(\pi a)^2]^{1/2}$ with $c=1.12*A^{1/3}$ fm and a=0.545 fm [29]. R is the equivalent radius of the Woods-Saxon distribution of nuclear matter. This radius is also used in the form factor calculation for strong production. This is discussed below.

The function $f_s(q)$ from the strong production amplitude, T_s, can be written as [28]

[29] B. Hahn, D.G. Ravenhall and R. Hofstadter, Phys. Rev. 101, 1131 (1956).

$$f_s(q) = A \int d^3r \, e^{i\vec{q}\cdot\vec{r}} \, e^{-\frac{1}{2}\sigma' T(b)} \, e^{i\chi_c(b)} \, \sqrt{2} \, \frac{(\hat{\varepsilon}\times\hat{k})}{q_t} \nabla\rho(r) \; .$$

Here, $\sigma'=(1-ix)\sigma$ where σ is the total π^+ nucleon cross section and x is the ratio of the real to imaginary part of the forward scattering amplitude for π^+ nucleon collisions, T(b) is the nuclear thickness as a function of impact parameter b and is written as

$$T(b) = A \int_{-\infty}^{\infty} dZ \, \rho(b)$$

with ρ being the density distribution of nuclear matter. χ_c is the Coulomb phase created by the distortion of the wave functions of the incoming and outgoing states by the Coulomb field of the nuclear target, and is given by

$$\chi_c(b) = \frac{-Ze^2}{hc} \int_{-\infty}^{\infty} dZ \, \phi((b^2 + Z^2)^{1/2})$$

where

$$\phi = \int d^3r \, \frac{\rho(r')}{(|\vec{r}\cdot\vec{r}'|)}$$

is the coulomb potential of the nucleus.

The function $f_s(q)$ is sensitive to the nuclear shape because of the gradient, $\nabla\rho(r)$. Consequently an explicit Woods-Saxon density distribution is used to characterize the nuclear shape. This distribution has the form $\rho(r)=\rho_0/(1+\exp(r-c/a))$ where a and c have been defined above.

Before comparing these calculated cross section with the data the t resolution of the spectrometer had to be taken into account. The observed cross section was assumed to be a convolution of the true production cross section with a resolution function $R(t,\tilde{t})$,

$$\frac{d\sigma}{dt} = \int dt\, R(t,\tilde{t})\, \frac{d\sigma}{d\tilde{t}} \quad . \tag{24}$$

The resolution function was parameterized as a two-dimensional Gaussian in transverse momentum (see Appendix B):

$$R(t,\tilde{t}) = \frac{1}{2\pi\sigma^2}\, e^{-(|\vec{q}_t-\tilde{\vec{q}}_t|^2)/2\sigma^2} \quad .$$

In this expression, $\tilde{\vec{q}}_t$ and $\vec{q}_t$ are the exact and the resolution-smeared transverse momentum, respectively. σ is the standard deviation of the resolution function and was determined by using the Monte Carlo. This type of fit was tested with K decays and found to work well (see Chapter V.). For the B^+ data σ was 19.2 GeV for the Pb and 20.0 GeV for Cu target.

Folding in the resolution, the t dependent factors $f_c(q)$ and $f_s(q)$ were calculated and averaged over the t intervals corresponding to the binning of the data. The three parameters, Γ_γ, C_s, and ϕ were varied to obtain the best fit of equation (23) to the data. The fit was performed out to $t<0.01$ GeV^2. This was done to emphasize the Coulomb contribution as well as avoid the region of large background and low statistics.

The fits were performed on the data from each target and on the combined data. It was found that there were two minima for each data set. Table 12 summarizes these results. The values for C_s and ϕ are not well determined. Without sufficient statistics in the higher t bins where the strong contribution dominates it is difficult to determine these parameters.

Γ_γ is comparatively stable but there are two minima. As a way out of this dilemma an average number was chosen for each set of minima and the errors were extended to include the outside of each minima. For the Pb and Cu targets this lead to Γ_γ=232±50 keV and to Γ_γ=219±50 keV for the combined data. Table 13 presents the integrated values of $T_s{}^2$, $T_c{}^2$, and the interference term for t less than 0.01 GeV^2 for the Pb and Cu target data.

As with the mass and the full width results listed above these fits were tested for stability. In addition to varying the t range a background term of the form A*exp(-A't) was included in the fits. Here, A and A' were fitted parameters. The fluctuations were always within the statistical errors listed on Table 12. The fits were also performed with different t resolutions. Any excursions away from the resolution value chosen by the Monte Carlo resulted in an increased χ^2 while only modestly changing the width. Typical changes of the width were 4%.

Table 12

Results of Fits to t Distributions

Target	Fit Id.	$\Gamma(B\to\pi\omega)$ (keV)	C_s (mb/GeV)	ϕ (degrees)	χ^2/DOF
Pb	1	258±28	2.09±1.07	-137±27	3.22/5
Pb	2	217±39	4.19±0.74	145±22	3.15/5
Cu	1	259±23	1.87±0.67	-83±32	3.43/6
Cu	2	227±46	2.40±0.82	94±31	3.46/6
Combined	1	236±32	1.87±0.57	-97±24	19.4/14
Combined	2	194±26	2.89±0.60	107±19	16.2/14

Table 13

Integrated Cross Sections for B^+ Production

Target	Fit Id.	$\int dt \ T_c^{\ 2}$ (μb)	$\int dt \ T_s^{\ 2}$ (μb)	$2 \ Re \int dt \ T_c^* T_s \ e^{i\phi}$ (μb)
Pb	1	367± 40	75± 39	-103± 27
Pb	2	309± 22	151± 27	-121± 15
Cu	1	57± 12	29± 10	1.69± 0.35
Cu	2	50± 10	37± 13	0.34± 0.04

D. Conclusions

This experiment identified the B^+ meson in the coherent final state $\pi^+\omega$. The mass and width of the resonance are m_B=1.271±0.011 GeV and $\Gamma_{\pi\omega}$=0.232±0.029 GeV. The mass and width quoted here are larger than the values listed by the Particle Data Group as m_B=1.232 GeV and $\Gamma_{\pi\omega}$=0.137 GeV (see reference 22). It is important to note that previously reported measurements vary from 1.200 - 1.268 GeV for the mass and 0.100 - 0.182 GeV for the width [22]. In addition this experiment has reported radiative widths for the ρ^-, $K^{*\pm}$, $K^{*+}(1420)$, and $A2^+$ mesons [30]. Of particular interest is the $A2^+\to\pi^+\eta$ mass and full width measurements. The η has two decay modes to which this experiment was sensitive. These are $\eta\to\gamma\gamma$ and $\eta\to\pi^+\pi^-\pi^0$. When the η decays to three pions the $A2^+$ and B^+ mesons have the same final state particles. The values of the mass and width for the $A2^+$ are m_{A2}=1.312 0.009 GeV and $\Gamma_{\pi\eta}$=0.098 0.014 GeV for the $\gamma\gamma$ mode and m_{A2}=1.302 0.014 GeV and $\Gamma_{\pi\eta}$=0.140 0.082 MeV for the $\pi^+\pi^-\pi^0$ mode

[30] For the ρ^- see T. Jensen et al., Phys. Rev. D 27, 26 (1983); for the K^{*-} see D. Berg et al., Phys. Lett. 99B, 119 (1981); for the K^{*+} see C. Chandlee et al., Phys. Rev. Lett. 51, 168 (1983); for the $K^{*+}(1420)$ see S. Cihangir et al., Phys. Lett. 117B, 123 (1982); for the $A2^+$ see S. Cihangir et al., Phys. Lett. 117B, 119 (1982).

[31]. These numbers agree well with the accepted values of m_{A2}=1.310 GeV and $\Gamma_{\pi\eta}$=0.102 GeV. This agreement with standard values of the A2 parameters argues against any systematic error in this experiment in measuring the four pion final state. It should also be noted that this experiment's measurement of the B^+'s mass and width has been performed via an electromagnetic reaction, which is better understood and less susceptible to background than previous strong interaction production experiments.

The B^+ meson has a spin-parity assignment of $J^P=1^-$. The determinination of the ω helicity amplitudes showed a strong dominance of the helicity $\lambda=\pm1$ states, the probability for helicity zero being $|F_0|^2=0.15\pm0.035$. The value of $|F_0|^2$ is consistent with previous measurements [26] and indicates that the resonance has unnatural spin-parity, ie 1^+, 2^-, 3^+,... [27]. This observation is in agreement with the spin and parity of the established B^+ meson

For the radiative width we quote a value of 232±61 keV. This value is the width as determined by the targets separately. The error of 61 keV now includes the 15% uncertainty in the overall normalization (see Table 11). The values for C_s and ϕ are not well determined. For this reason, the fitting of the combined data appeared artificially constrained and the combined target value for the width (219±53 MeV) is not as reliable even though both values are

[31] "Measurement of the Radiative Decay Widths of the $A2^+$ and $K^{*+}(1420)$ Mesons", thesis by Selcuk Cihangir, University of Rochester (1981).

consistent. If the values for the mass, full width, and F_0 measured by this experiment are used to predict the radiative width of the B^+, as was done in Chapter I., the predicted value is 274±48 keV.

Appendix A

An analysis of the sequential decays $B^+ \to \pi^+ \omega$, $\omega \to \pi^+ \pi^- \pi^0$ was performed using the formalism suggested by Berman and Jacob [32]. In this formalism the matrix element M for the decay of the B^+ with spin and Z projection (J,m) is given by

$$M \propto \sum_{\lambda=0,\pm1} F_\lambda \, D^{*J}_{m\lambda} (\Phi,\Theta,0) \, D^{*0}_{\lambda 1} (\Phi,\Theta,0) \; . \tag{A.1}$$

In this equation F_λ is the helicity amplitude of the ω and $\sum F_\lambda = 1$. Θ and Φ are the polar and azimuthal angles of the ω in the B^+ rest frame, and θ and ϕ are the corresponding angles of the normal to the ω decay plane (see figure 49). The angles θ and ϕ are measured in the ω rest frame with Z' defined as the momentum direction of the ω and $\hat{Y}' = \hat{Z} \times \hat{Z}'$. The Z axis is defined as the momentum direction of the B^+ (helicity frame) and the Y axis is the normal to the production plane,

[32] S. M. Berman and M. Jacob, Phys. Rev. 139, B 1023 (1965).

$\hat{Y}=\hat{p}_{\pi}x\hat{p}_{B}$.

It should be noted that at the t values relevant to this experiment $\vec{p}_{\pi}$ and $\vec{p}_{B}$ are nearly parallel, and the spectrometers resolution was insufficient to accurately determine the production plane. Consequently the analysis of these decays was limited to determination of the helicity amplitudes of the ω.

To determine the helicity decay probability equation (A.1) is squared and then the expression is reduced. This is done by shifting the ϕ dependence to the first of the two D-functions and then reducing the product of two $D(\alpha,\beta,\gamma)$ functions to one using the Clebsh-Gordon series. This results in the equation

$$\frac{d\sigma}{d\cos\Theta\, d\Phi\, d\cos\theta\, d\phi} = \frac{3(2J+1)}{16\pi^2} \sum_{L} \sum_{\substack{mm' \\ \lambda\lambda'}} (-1)^m \rho_{mm'}$$

$$* F_{\lambda}F_{\lambda'} C(JJL;-mm') C(JJL;-\lambda\lambda')$$

$$* D_{m'-m,\lambda'-\lambda}(\Phi,\Theta,\phi) d^{1}_{-\lambda 0}(\theta) \; d^{1}_{\lambda' 0}(\theta) \; . \qquad (A.2)$$

The $\rho_{mm'}$ elements are the density matrix elements of the B^+ meson.

Parity conservation yields $F_{\lambda}=-P(-1)^{J}*F_{\lambda}$ where P is the parity of the B^+ meson [33]. With this condition the helicity amplitude F_{λ} can be different from zero only for the unnatural parity series 1^+, 2^-,

[33] S. U. Chung, Phys. Rev. 138, B 1541 (1965).

3^+, ... For $J^P=0^-$ only the F_0 amplitude is allowed [33].

Integrating equation (A.2) yields

$$\frac{d\sigma}{d\cos\theta} = \frac{3}{2} (|F_0|^2 \cos^2\theta + |F_1|^2 \sin^2\theta) \ . \qquad (A.3)$$

Using the nomalization condition this equation can be written as

$$\frac{d\sigma}{d\cos\theta} = \frac{1}{2} (1 + (3|F_0|^2 - 1) \ p_2(\cos\theta)) \ . \qquad (A.4)$$

The value of $|F_0|^2$ can now be evaluated by the method of moments or fitting equation (A.4) to the $\cos\theta$ distribution. Figure 50a shows the $\cos\theta$ distribution. The data used here was selected using the cuts from Table 8 and using only those events in the mass region 1.0 - 1.4 GeV. The figure clearly shows a dominate $\sin^2\theta$ constribution. The line in the figure represents equation (A.4) with $|F_0|^2=0.137\pm0.034$.

The helicity zero decay probability was also evaluated using the mean value of $P_2(\cos\theta)$. From equation (A.4) we get

$$|F_0|^2 = \frac{1}{3} (5 \ \langle p_2(\cos\theta)\rangle + 1) \ . \qquad (A.5)$$

This gives $|F_0|^2=0.161\pm0.031$. Figure 50b shows the dependence of $|F_0|^2$ on the $\pi^+\omega$ mass (140 MeV bins).

The average value from the two methods is $|F_0|^2=0.149\pm0.033$. This value is consistent with previous measurements [34]. The

[34] For the most recent results see reference 26. For a review of previous spin-parity analysis of the B meson see paper by S.U. Chung in "Experimental Meson Spectroscopy - 1974", edited by D.A. Garelick, A.I.P. New York, 1974.

presence of a small but significant $|F_0|^2$ term indicates that the resonance is consistent with the unnatural parity series.

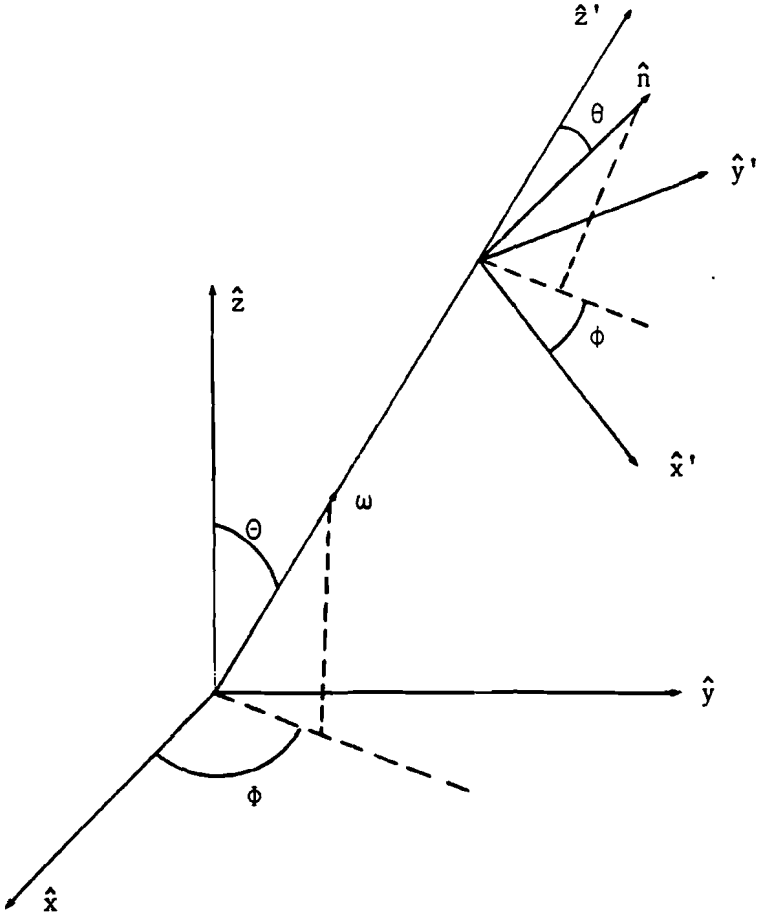

Figure 49

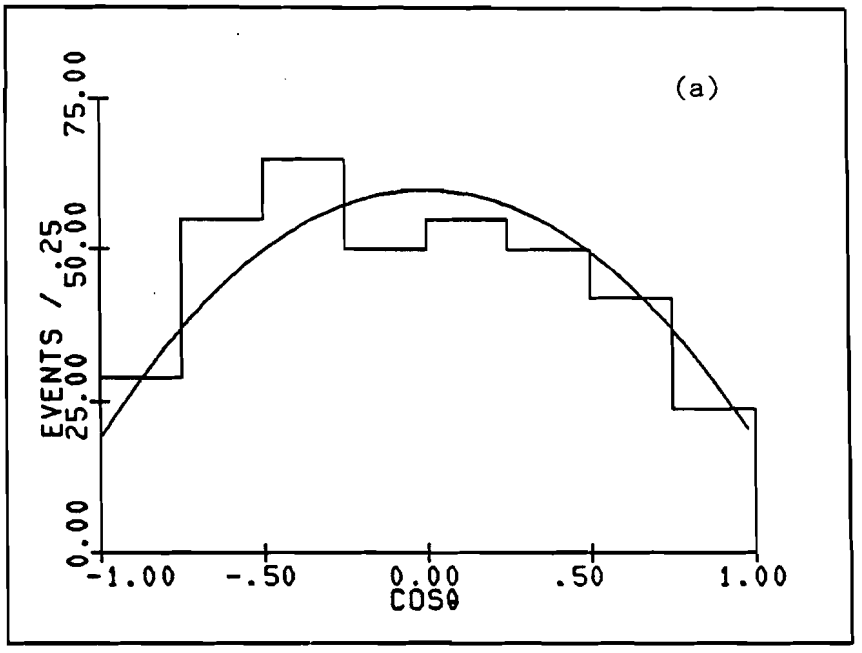
(a)
EVENTS / .25
0.00
25.00
50.00
75.00
-1.00
-.50
0.00
.50
1.00
COSθ

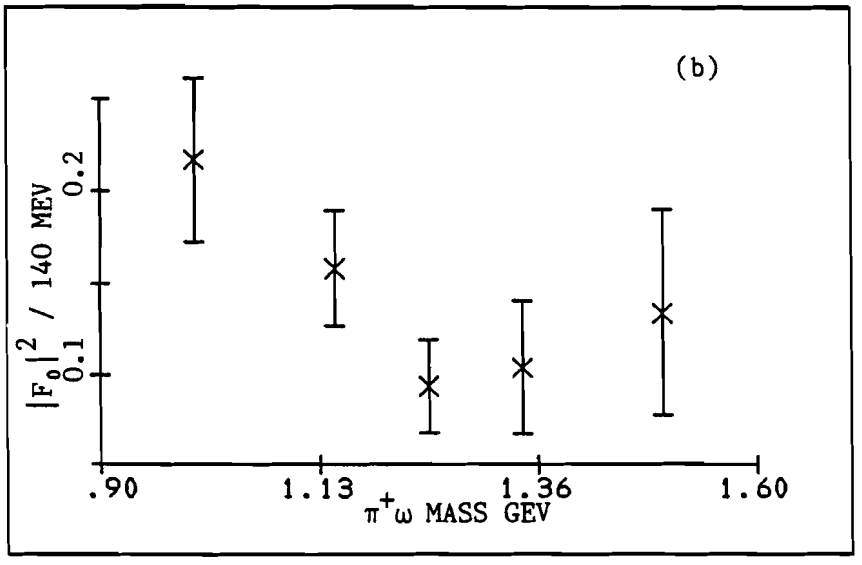
(b)
$|F_0|^2$ / 140 MEV
0.1
0.2
.90
1.13
1.36
1.60
$\pi^+\omega$ MASS GEV

Figure 50

Appendix B

The t resolution of the spectrometer was determined by the K^+ decays. Since this process is a decay the events occur with t=0 and any resulting distribution is due to the resolution of the spectrometer. This section derives the expected t distribution for these decays.

First it was assumed that the measured transverse momentum $\vec{p}_t$ was a Gaussian distribution centered at the true transverse momentum $\tilde{\vec{p}}_t$. It was further assumed that the momentum resolution was equal in both the horizontal and vertical directions, $\sigma_x = \sigma_y$, and that σ_x and σ_y were uncorrelated. With these assumptions the resolution function of the transverse momentum can be written as

$$R(\vec{p}_t, \tilde{\vec{p}}_t) = \frac{1}{2\pi\sigma^2} e^{-((\vec{p}_t - \tilde{\vec{p}}_t)/2\sigma^2)}$$

The expected distribution for events in p_t^2 is

$$\frac{d\sigma}{dt}(p_t^{\,2}) = \int d^2\,\tilde{\vec{p}}_t\; R(\vec{p}_t,\tilde{\vec{p}}_t)\,\frac{d\sigma}{d\tilde{t}}(\tilde{\vec{p}}_t^{\,2})\ . \tag{B.2}$$

This equation is then transformed from $p_t^{\,2}$ to t and becomes

$$\frac{d\sigma}{dt}(t) = \frac{\cos\theta}{2\sigma^2}\int d\tilde{t}\; e^{-((p_t-\tilde{p}_t)^2/2\sigma^2)}\; e^{-(2p_t\tilde{p}_t/2\sigma^2)}$$

$$* \; I_o\left(\frac{2p_t\tilde{p}_t}{2\sigma^2}\right)\cos\tilde{\theta}\,\frac{d\sigma}{d\tilde{t}}(\tilde{t})\ . \tag{B.3}$$

Now the process is a decay so the values are $t=0$, $p_t=0$ and $\cos\theta=1$. This leads to

$$\frac{d\sigma}{dt}(t) = \frac{1}{2\sigma^2}\,\frac{d\sigma}{dt}(0)\; e^{-t/2\sigma^2}\ . \tag{B.4}$$

The observed t distributions can thus be parameterized as

$$N(t) = N_o\; e^{-t/2\sigma^2} \tag{B.5}$$

This function was used to fit the K^+ decay t distributions to obtain the resolution σ.

Equation (B.5) was used to fit both data and Monte Carlo generated K^+ decays. The resolutions, σ, were in good agreement (see Table 4) and so the Monte Carlo was used to determine the spectrometer's resolution for an arbitrary process. This was done by generating the Monte Carlo events for this process at $t=0$ and fitting

the reconstructed t distribution to equation (B.5). The resulting resolution was an important input parameter in the determination of the radiative width (see Chapter VII.).